



**Michigan  
Technological  
University**

Michigan Technological University  
**Digital Commons @ Michigan Tech**

---

Dissertations, Master's Theses and Master's Reports

---

2016

# WIRELESS IMPLANTABLE MAGNETOELASTIC SENSORS AND ACTUATORS FOR BIOMEDICAL APPLICATIONS

Andrew DeRouin

*Michigan Technological University, [ajderoui@mtu.edu](mailto:ajderoui@mtu.edu)*

Copyright 2016 Andrew DeRouin

---

## Recommended Citation

DeRouin, Andrew, "WIRELESS IMPLANTABLE MAGNETOELASTIC SENSORS AND ACTUATORS FOR BIOMEDICAL APPLICATIONS", Open Access Dissertation, Michigan Technological University, 2016.  
<http://digitalcommons.mtu.edu/etdr/233>

Follow this and additional works at: <http://digitalcommons.mtu.edu/etdr>



Part of the [Biomedical Engineering and Bioengineering Commons](#)

WIRELESS IMPLANTABLE MAGNETOELASTIC SENSORS AND ACTUATORS  
FOR BIOMEDICAL APPLICATIONS

By

Andrew J. DeRouin

A DISSERTATION

Submitted in partial fulfillment of the requirements for the degree of

DOCTOR OF PHILOSOPHY

In Biomedical Engineering

MICHIGAN TECHNOLOGICAL UNIVERSITY

2016

© 2016 Andrew J. DeRouin

This dissertation has been approved in partial fulfillment of the requirements for the Degree of DOCTOR OF PHILOSOPHY in Biomedical Engineering.

Department of Biomedical Engineering

Dissertation Advisor: *Keat Ghee Ong*

Committee Member: *Rupak Rajachar*

Committee Member: *Jeremy Goldman*

Committee Member: *Yongmei Jin*

Department Chair: *Sean Kirkpatrick*

*This dissertation is dedicated to Tim and Wendy DeRouin.*

## Table of Contents

PREFACE .....	8
ACKNOWLEDGMENTS .....	10
ABSTRACT .....	11
<b>1. BACKGROUND AND RESEARCH OBJECTIVES .....</b>	<b>13</b>
1.1. EVIDENCE-BASED CARE .....	13
1.2. SENSOR POWER SCHEMES .....	14
<i>1.2.1. Active Sensors.....</i>	<i>15</i>
<i>1.2.2. Semi-Passive Sensors.....</i>	<i>16</i>
<i>1.2.3. Passive Sensors.....</i>	<i>16</i>
<i>1.2.3.1. Inductive-Capacitive Sensors .....</i>	<i>16</i>
<i>1.2.3.2. Magnetoelastic Sensors .....</i>	<i>17</i>
1.3. RESEARCH OBJECTIVE .....	18
REFERENCES .....	19
<b>2. MAGNETOELASTIC DETECTION THEORY AND DEVICE DEVELOPMENT .....</b>	<b>23</b>
2.1. MAGNETIC MATERIALS THEORY .....	23
2.2. MAGNETOELASTIC RESONANCE DETECTION.....	25
<i>2.2.1. Impedance Measurement.....</i>	<i>26</i>
<i>2.2.2. Frequency Domain Measurement.....</i>	<i>27</i>
<i>2.2.3. Time-Domain Measurement .....</i>	<i>28</i>
2.3. THRESHOLD-CROSSING DETECTION DEVICE.....	29
<i>2.3.1. Threshold-Crossing Circuit.....</i>	<i>29</i>
2.4. MAGNETO-HARMONIC DETECTION.....	32
2.5. HARMONIC DETECTION DEVICE.....	33
<i>2.5.1. Harmonic Excitation Circuit .....</i>	<i>33</i>
<i>2.5.2. Harmonic Detection Circuit .....</i>	<i>34</i>
REFERENCES .....	38

<b>3. GEOMETRICAL MODIFICATION OF MAGNETOELASTIC SENSORS TO ENHANCE SENSITIVITY .....</b>	<b>39</b>
ABSTRACT .....	39
3.1. INTRODUCTION.....	40
3.2. EXPERIMENTS .....	42
3.2.1. <i>Triangular Sensors versus Rectangular Sensors</i> .....	42
3.2.2. <i>Sensor Fabrication and Calibration</i> .....	45
3.2.3. <i>Sensor Array Fabrication and Demonstration</i> .....	47
3.3. RESULTS AND DISCUSSIONS .....	50
3.4. CONCLUSIONS .....	56
REFERENCES .....	57
<b>4. MULTI-PARAMETER SENSING WITH A SINGLE MAGNETOELASTIC SENSOR BY APPLYING LOADS ON THE NULL LOCATIONS OF MULTIPLE RESONANT MODES .....</b>	<b>59</b>
ABSTRACT .....	59
4.1. INTRODUCTION.....	60
4.2. EXPERIMENTS .....	64
4.2.1. <i>Confirming Null Locations</i> .....	66
4.2.2. <i>Changing width of the sensing region</i> .....	68
4.2.3. <i>Changing Length of the Sensing Region</i> .....	70
4.2.4. <i>Loading Multiple Null Locations Simultaneously</i> .....	70
4.3. RESULTS AND DISCUSSIONS .....	71
4.3.1. <i>Confirming Null Locations</i> .....	71
4.3.2. <i>Changing the Sensing Region Width</i> .....	72
4.3.3. <i>Changing the Sensing Region Length</i> .....	75
4.3.4. <i>Loading Multiple Regions Sequentially</i> .....	77
4.4. CONCLUSIONS .....	78
REFERENCES .....	79

<b>5. A WIRELESS SENSOR FOR REAL-TIME MONITORING OF TENSILE FORCE ON SUTURED WOUND SITES .....</b>	<b>81</b>
ABSTRACT .....	81
5.1. INTRODUCTION.....	82
5.2. EXPERIMENTS .....	84
5.2.1. <i>Sensor Design and Fabrication</i> .....	84
5.2.2. <i>Detection System and Coils</i> .....	86
5.2.3. <i>Setup for Force Monitoring at Simulated Skin Repair</i> .....	89
5.2.4. <i>Setup for Force Monitoring at a Simulated Tendon Repair</i> .....	92
5.3. RESULTS AND DISCUSSION.....	93
5.3.1. <i>Characterization of Sensor Performance</i> .....	93
5.3.2. <i>Force Monitoring at a Simulated Skin and Tendon Repairs</i> .....	100
5.4. CONCLUSIONS .....	103
REFERENCES .....	104
<b>6. FORCE SENSING SUTURE ANCHOR FOR REAL TIME MONITORING OF TENSILE LOADS.....</b>	<b>107</b>
ABSTRACT .....	107
6.1. INTRODUCTION.....	108
6.2. EXPERIMENTS .....	111
6.2.1. <i>Design and Fabrication of Force Sensing Suture Anchor</i> .....	111
6.2.2. <i>Experimental Setup and Procedures</i> .....	112
6.2.3. <i>Custom Detection Device</i> .....	114
6.2.3.1. <i>Excitation Circuit</i> .....	114
6.2.3.2. <i>Detection Circuit</i> .....	116
6.3. RESULTS AND DISCUSSIONS .....	118
6.4. CONCLUSIONS .....	122
REFERENCES .....	122
<b>7. MAGNETOELASTIC GALFENOL AS A STENT MATERIAL FOR WIRELESSLY CONTROLLED DEGRADATION RATES .....</b>	<b>125</b>

ABSTRACT .....	125
7.1. INTRODUCTION.....	126
7.2. EXPERIMENTS .....	129
7.2.1. <i>Degradation Experiment</i> .....	129
7.2.2. <i>Surface Characterization</i> .....	130
7.2.3. <i>Indirect Cytotoxicity Test</i> .....	131
7.3. RESULTS AND DISCUSSION.....	132
7.3.1. <i>Degradation Experiment</i> .....	132
7.3.2. <i>Surface and Cross-Sectional Characterization</i> .....	134
7.3.3. <i>Indirect Cytotoxicity Test</i> .....	141
7.4. CONCLUSION.....	146
REFERENCES .....	147
<b>8. OVERALL CONCLUSIONS .....</b>	<b>151</b>
APPENDIX .....	155

## Preface

All work presented in this document was conducted in the Biosensors Laboratory at the Michigan Technological University campus. Unless otherwise noted, the copyright for material in this document has been retained by the authors.

A version of the work presented in Chapter 3 was previously published [Nina Pacella, Andrew DeRouin, Brandon Pereles and Keat Ghee Ong, “Geometrical modification of magnetoelastic sensors to enhance sensitivity,” *Smart Materials and Structures*, 24, 025018, 2015.]. Nina Pacella was primarily responsible for conducting the experiments using individual sensors and 3D printing the coil apparatus, while I was responsible for overseeing the project, designing the detection device, and running experiments using the multi-sensor detection coil. Brandon Pereles was responsible for training Nina Pacella to use a variety of equipment which included the 3D printer, where he also contributed to the CAD design. Keat Ghee Ong oversaw the project as the adviser and directed the other authors.

A version of the work presented in Chapter 4 was previously published in [Andrew DeRouin, Keat Ghee Ong, “Multi-parameter sensing with a single magnetoelastic sensor by applying loads on the null locations of multiple resonant mode,” *Smart Materials and Structures*, vol. 25(3), 030544, 2016.]. I was responsible for conducting all experiments, designing and fabricating the detection device, writing the manuscript, as well as analyzing and preparing the resulting data. Keat Ghee Ong oversaw the project, contributed to the design conception, data processing, and manuscript composition.

The work presented in Chapter 5 was previously published in [Andrew DeRouin, Nina Pacella, Chunfeng Zhao, Kai-Nan An, Keat Ghee Ong, “A wireless sensor for real-time monitoring of tensile force on sutured wound sites,” *IEEE Trans. Biomedical Engineering*, vol. 63(8), pp. 1665-1171, 2016.]. Keat Ghee Ong advised the project, contributed to the experimental design conception, conducted a portion of experiments, as well as manuscript preparation. Nina Pacella contributed to the initial sensor characterization and experimental setup design. I was responsible for preparing the

manuscript, running the *ex vivo* experiments, and mentoring Nina during the initial characterization and fabrication of the sensors. Chunfeng Zhao and Kai-Nan An helped to direct the project and aided in conceptualizing the proposed design.

The work presented in Chapter 6 (which overlap with some elements of Chapter 2) will be submitted for publication to *IEEE Sensors Journal*. Keat Ghee Ong advised the project and contributed to the design conception as well as collecting information from surgeons and physical therapists regarding the clinical need and feasibility of the proposed technology. I was responsible for fabricating and testing the instrumented suture anchors as well as running experiments regarding the sensor's characteristic curve and cyclic drift. Additionally, I designed and fabricated the experimental setup for measuring the effect of displacement and created the calibration algorithm to correct for it. Alexa Thompson conducted the angular load experiments, as well as designed and fabricated the angular load test apparatus. She also conducted the offset-adjustment experiments.

Chapter 7 contains work that will be submitted to *IEEE Transactions on Biomedical Engineering*. As an American Heart Association fellow, I was primarily responsible for the execution of this project. I conducted the degradation experiments in addition to the cell culture protocols. I was also a significant part of the groundwork going into this project, performed all image analysis, and composed the manuscript. Weilue He obtained the primary aortic smooth muscle cells and helped with the tissue culture and fluorescent imaging thereof. He also helped with the statistical analysis conducted in this work. Roger Guillory conducted the SEM imaging and provided insights into the SEM image analysis. Dr. Goldman advised on the proper methods for the degradation experiments and Dr. Rajachar and Dr. Frost advised on the proper methods for and the cell work. Dr. Ong advised on the degradation experiments and magnetoelastic sensor fabrication and experimental setup and additionally contributed to manuscript preparation.

## **Acknowledgments**

There are far too many people to acknowledge in regards to this work and the training that enabled me to do it, but I will try. First, I would like to thank my family members who were incredibly supportive during the course of my studies. I would also like to thank the faculty and staff in the Electrical and Biomedical Engineering Departments at MTU who have helped become the research scientist and critical thinker that I am today.

My committee members deserve special thanks for their encouragement, training, and efforts towards developing my skill set and a mindset for research. Above all, I would like to thank my adviser, Dr. Ong, for the opportunity that he provided me in allowing me to work in his lab. He has excelled as a mentor and has acted as an example of the type of scientist I want to be.

I would also like to thank my fellow undergraduate and graduate students. A number of them contributed significantly to training me and contributing to the work within this document. I sincerely appreciate everything that the people I've interacted with at MTU have done for – and with – me.

Finally, I would like to give my appreciation to the American Heart Association for awarding me with a predoctoral fellowship. Working at this university on these projects has been a great opportunity that has helped me to develop and expand my skill set and my curiosity beyond anything I would have expected.

## Abstract

Magnetoelastic sensors represent a low-cost wireless and battery-less method for monitoring parameters in embedded or implanted applications; however, some limitations still exist preventing their commercial implementation. Presented in this work are a variety of studies that are aimed at improving the feasibility of magnetoelastic materials for sensing and actuating applications. Magnetoelastic resonant sensors of non-standard geometries were investigated to determine if geometry could play a role on the sensitivity of the sensor response to mass loading. It was shown that a significant increase in sensitivity could be achieved by using triangular sensors rather than standard rectangular strips. A method for monitoring multiple parameters on a single magnetoelastic resonant strip was also pursued. It was demonstrated that multiple parameters will have different effects depending on the location of the applied load due to the effect of sensor areas with zero vibration at different harmonics of the fundamental resonant frequency.

Magneto-harmonic sensors and actuators were also explored in this work. Specifically, it was demonstrated that magnetoelastic sensors could be implemented as a means of detecting stresses on deep tissue wounds, which are critical for proper healing of certain wound sites after surgery. Both a suture and a suture anchor design were investigated for their efficacy at monitoring forces applied to tendon repair sites.

Two detection devices were fabricated and built for this work which represent low-cost alternatives (both less than \$200 each) to commercially available alternatives that minimally cost tens of thousands of dollars. This advancement reinforces the claim that magnetoelastic materials are a low-cost and portable sensing solution.

The biodegradability and cytotoxicity of a promising magnetoelastic material for biomedical applications, specifically Galfenol (iron-gallium), was also investigated. Cytotoxicity tests demonstrated that concentrations much higher than would be likely to be encountered *in vivo* are necessary to cause significant cellular toxicity. Additionally, surface characterization of the degraded materials suggests that the degradation rate of Galfenol can be wirelessly controlled through application of externally applied magnetic

fields to more readily expose the bulk material to biological solvents. Further studies involving the *in vivo* response of this material for stenting and other biomedical applications are warranted.

## **1. Background and Research Objectives**

The evolution of physiological monitoring has been critical for diagnosing and preventing pathologies as well as tracking the efficacy of human interventions. Most quantitative diagnostic and monitoring tools today still rely on external, wired connections to obtain useful biofeedback; however, a number of wireless and implantable solutions have emerged in the past several decades which have the potential to revolutionize healthcare. While most of these systems have not reached the stage of clinical trials, their impact on human health and quality of life will likely be of great significance.

The goal of implantable medical sensors and actuators is the reduction of healthcare costs, improved healing times, and improved patient outcomes. Many implantable sensors are integrated into current implantable devices. For example, implantable glucose pumps contain glucose sensors which help in determining when and how much insulin should be delivered to the patient [1.1]. Similarly, heart activity is monitored in order to determine the correct timing and intensity required to provide vital information for implantable cardioverter defibrillators to jump-start failing hearts [1.2]. Cochlear implants also contain sensing elements; microphone sensors are used to pick up external vibrations which are then processed and applied to electrodes that directly stimulate the auditory nerve [1.3].

### **1.1. Evidence-Based Care**

Recently, there has been a push in the medical community to transition towards evidence-based care. Scholarly articles present a vast amount of data that can be used to improve the quality of care given by physicians; however, there has traditionally been very little integration of scientific findings into clinical practice. Grimshaw and Eccles found that 30-40% of treatments were not in accordance with current scientific evidence while 20-25% of the care provided was found to be harmful or unnecessary [1.4,1.5].

There are a number of significant hurdles contributing to this problem. While some physicians do not actively attempt to disseminate research findings for integration into their practices, others do not agree with results obtained in the studies. The inability to replicate the same results as the publishing authors is also an issue which may arise due to lack of instrumentation, patient compliance, variability among patients, or time available for physicians to train [1.4]. While physician experience is critical in the proper diagnoses and treatment of physiological ailments, tools that have emerged for use in understanding, visualizing, and predicting the course of pathologies have improved the field of medicine tremendously and have helped to usher in evidence-based care by providing a basis for comparison. To that end, and with the miniaturization of electronic components, a number of wireless systems have recently been put forward to quantify physiological parameters. Such instruments are capable of bridging the gap between data collected in research studies and the conditions of the individual patient which can vary based on physical activity level, diet, anatomical variability, and a number of other factors. As a result, wireless sensing technologies are arising which open the door to patient-centered and evidence-based care, rather than “top-down” textbook protocols. These technologies, in the hands of physicians, represent a method for providing biofeedback regarding individual patients as well as a platform for collecting data on a large scale for further understanding of pathologies and improved treatment protocols.

## **1.2. Sensor Power Schemes**

Existing wireless sensing systems fall into several categories. Active systems tend to be all-in-one solutions that include on-board power sources such as batteries and/or capacitive storage [1.6]. Passive systems, on the other hand, act independently and either produce a signal as a direct result of stimulus or through the use of externally coupled power sources (mutual inductance coupling). These systems operate by using sophisticated electronics and detection algorithms externally rather than directly incorporated with the sensor. Passive systems typically have the advantage of integrating

more seamlessly into the desired application, are smaller due to the lack of complexity of the physical implant, and do not need to be removed/replaced due to the absence of an on-board power source. Active sensing systems, on the other hand, can generally obtain more information (more sensing elements, higher resolution, or higher sensitivity, etc.) and can be used in the form of wireless sensor networks to relay large quantities of information. Active systems can also provide a constant flow of information, whereas passive sensors only relay information when interrogated externally. Some systems can be considered semi-passive, such as those with onboard power sources which can be wirelessly charged or harvest energy from their environment. These sensor systems have the same advantages and disadvantages as active systems except that the power supply does not need to be replaced over time and space requirements are often increased to achieve the added functionality.

### **1.2.1. Active Sensors**

Active sensors have a number of advantages, especially when the monitoring area is accessible on a periodic or constant basis. This allows their power supplies to be recharged or replaced manually. Their high degree of power storage makes active sensors ideal for providing a continuous flow of data from the embedded device to a remote transceiver. However, it also comes with the necessity to change the power source upon depletion. As a result, active sensors are not ideal for situations where access to the device is restricted or impossible.

With active sensors, it is typically possible to include more complexity and functionality in the sensing system. This can include multiple sensing channels, multiple sensing parameters, and improved performance (resolution, sampling rate, transmission distance, etc.) when compared to other types of systems. The tradeoff for these characteristics is in size of the physical device, the necessity for invasive power supply replacement, careful power supply management, and a less durable composition.

### **1.2.2. Semi-Passive Sensors**

Semi-passive (or semi-active) sensors are similar to active sensors, but include a mechanism for wireless powering. These systems can still incorporate active circuit components. The primary advantage of semi-passive systems is that they are able to preserve some of the measurement characteristics of active systems while allowing the embedded system to remain embedded and functional for an extended duration without accessing the embedded location. Implantable force measurement devices for the knee [1.7] and spine [1.8] are examples of semi-passive medical sensors. In addition to extended lifetime, these devices are often implemented to reduce the number of failure-prone or environmentally sensitive components.

### **1.2.3. Passive Sensors**

The third category of sensor systems is considered “passive,” meaning that they do not contain active components or an onboard power source. Surface acoustic wave (SAW), inductive-capacitive (LC), and magnetic-based platforms are some of the most common passive systems. The functionality of these systems relies on short-range electromagnetic, magnetic, or acoustic coupling between the sensor and an external detection unit [1.6].

#### **1.2.3.1. Inductive-Capacitive Sensors**

LC sensors are comprised of an inductive and a capacitive component (and sometimes a resistive component). The inductive component couples to an external detection coil through mutual inductance coupling, and the resonant frequency of the circuit is determined. The most common configuration for LC sensors implements an inductive component for coupling electromagnetic energy and a capacitive element that varies based on the parameter of interest. As the capacitance of the LC circuit changes, the resonant frequency changes. In some cases, the inductive element is used as both the

sensing and the energy coupling component. A third case exists wherein a resistive element is added to the circuit and used as the sensing element. Although the resistive element does not change the resonant frequency, the damping that it applies to the system does have a significant effect on the quality factor of the resonance. The advantage of using resonant frequency detection is that the error due to displacement of the sensor relative to the detector coil is very low. Additionally, decreasing the quality factor by increasing the resistance of the resistive element decreases the signal strength, thus decreasing the maximum detection range.

LC sensors have the advantage of high durability and small physical footprint since they can be created from any conductive material. Often, LC sensors are printed on fiberglass PCB with a single jumper to complete the circuit [1.9]. More recently, LC sensors have been created which implement only a single layer conductive spiral which acts as both the sensing and inductive coupling element. This is achieved by using the parasitic capacitance between parallel traces as a sensing element [1.10].

### **1.2.3.2. Magnetoelastic Sensors**

Another example of a passive sensor is the magnetoelastic sensor. Magnetoelastic materials can convert mechanical (elastic) energy to magnetic energy as well as magnetic to mechanical. Because magnetic field is not significantly attenuated by human tissue when compared to electric field, magnetoelastic sensors are more desirable for use in biomedical applications than inductive-capacitive sensors, especially when the parameter of interest requires implantation in the deep tissue. Magnetoelastic sensors resonate when they experience an AC magnetic field at their mechanical resonant frequencies. Depending on material selection, small magnetoelastic sensors in the range of a few millimeters to a few centimeters experience mechanical resonance in the range of tens of kHz to several MHz. Like any mechanical structure, the resonance is dependent on the elasticity and mass of the structure as well as any damping acting on it. Taking this into consideration, applied force [1.11], stress [1.12], pressure [1.13], or strain [1.14] can be

determined using this type of sensor. By applying surface coatings which react with and/or absorb specific compounds, the mass of the sensor can be changed, thus allowing remote monitoring of chemicals. Examples of parameters that have been monitored are humidity [1.15], carbon dioxide [1.16], ammonia [1.17], pH [1.18], biological parameters such as glucose concentration [1.19], bacteria growth/presence [1.20,1.21], and coagulation [1.22,1.23].

Magnetoelastic sensors can also be interrogated by monitoring the change in their permeability with applied stress [1.24]. By monitoring the signal at harmonics of the excitation frequency, the non-linear magnetization of the magnetoelastic sensor can be isolated from the excitation field. Resonant mode detection of physical parameters using magnetoelastic sensors has high sensitivity but low range due to the effects of damping. Harmonic detection, on the other hand, has a much higher load range [1.25], especially when dealing with positive magnetostriction materials whose permeability increases with applied stress. However, Pereles and coworkers recently showed that loading at the null locations of magnetoelastic resonant sensors (points of zero vibration) can significantly increase the dynamic range of this sensing method [1.25].

### **1.3. Research Objective**

Due to their small size, long lifetime, and high resilience to environmental factors, passive sensors are ideal for medical implant applications. For example Green and coworkers proposed a biliary stent sensor for use in monitoring “sludge accumulations” in biliary stents [1.26]. Puckett and coworkers also investigated coagulation detection for blood coagulation monitoring applications [1.22]. Although these systems have been investigated in the laboratory, they are not readily available on the market due to several drawbacks for their use. These shortcomings include the inability to monitor multiple parameters simultaneously, error due to displacement from the detection coil/system, and relatively high costs of detection devices compared to competing technologies.

Recent work has addressed some of these drawbacks for inductive-capacitive sensors. Specifically, LC sensors capable of multi-parameter monitoring were developed in addition to LC sensors consisting of only a single layer of conductor (decreasing unit price). These improvements to LC sensor technology improve their feasibility for acceptance in commercial applications. The goal of this work is similar; to improve the feasibility of magnetoelastic sensors for a variety of biomedical-focused applications. Several methods and applications are discussed here. Thus, Chapter 2 details the theory of operation for the magnetoelastic resonance and harmonic detection modes as well as the development of low-cost detection systems for each mode. A method for improving magnetoelastic sensor activity is discussed in Chapter 3, and monitoring multiple parameters simultaneously is discussed in Chapter 4. Chapter 5 and Chapter 6 explore two applications of the magneto-harmonic sensing method as well as a method for decreasing error due to changing distance of the sensor with the detection coil. Chapter 7 additionally addresses the biocompatibility of a potential magnetoelastic biomaterial comprised of iron and gallium ( $\text{Fe}_{80}\text{Ga}_{20}$ ). The studies conducted here provide insights into the feasibility of implementing magnetoelastic sensors and actuators in biomedical applications.

## References

- 1.1. E. Renard, "Implantable closed-loop glucose-sensing and insulin delivery: the future for insulin pump therapy," *Curr. Opin. Pharmacol*, Vol. 2, No. 6, pp. 708-716, 2002.
- 1.2. A.G. Rapsang, P. Bhattacharyya, "Pacemakers and implantable cardioverter defibrillators – general and anesthetic considerations," *Rev. Bras. Anesthesiol*. Vol. 64, No. 3 pp. 205-214, 2014.
- 1.3. P. Hasler, P.D. Smith, R. Ellis, D. Graham, D. Anderson, "Biologically inspired auditory sensing system interfaces on a chip," *Sensors*, 2002. *Proc. IEEE*, Vol. 1, pp. 669-674, 2002.

- 1.4. J.M. Grimshaw, M.P. Eccles, "Is evidence-based implementation of evidence-based care possible?" *Med. J. Aust.* Vol. 180, No. 6, pp. S50-S51, 2004.
- 1.5. M.T.E. Heafield, "Practitioners of evidence based care," *BMJ*, Vol. 320, pp. 954-955, 2000.
- 1.6. C. Hausleitner, R. Steindl, A. Pohl, H. Hauser, A.M.J. Goiser, F. Siefert "Cordless batteryless wheel mouse application utilizing radio requestable SAW devices in combination with the giant magneto-impedance effect." *Microw. Theroy Techn.*, Vol. 48, No. 4, pp. 817-822, 2001.
- 1.7. I. Kutzner, B. Heinlein, F. Graichen, A. Bender, A. Rohlmann, A. Halder, A. Beier, G. Bergmann, "Loading of the knee joint during activities of daily living measured in vivo in five subjects," *J. Biomech.*, Vol 43, pp. 2164-2173, 2010.
- 1.8. A. Rohlmann, M. Dreischarf, T. Zander, F. Graichen, P. Strube, H. Schmidt, G. Bergmann, "Monitoring the load on a telemeterised vertebral body replacement for a period of up to 65 months," *Eur. Spine J.*, Vol 22, No 11, pp 2575-2581, 2013.
- 1.9. S.F. Pichorim, P.J. Abatti, "A novel method to read remotely resonant passive sensors in biotelemetric systems," *IEEE Sens. J.*, Vol 8, No 1, 2008, pp 6-11. 2008
- 1.10. A.J. DeRouin, S.J. Treirweiler, B.D. Pereles, B. Lippi, K.G. Ong, "A low cost, wireless embedded sensor for moisture monitoring in hard-to-access places," *Sens. Lett.*, Vol. 11, No. 9, pp 1573-1579, 2013.
- 1.11. B.D. Pereles, A.J. DeRouin, K.G. Ong, "A wireless, passive magnetoelastic force-mapping system for biomedical applications." *J. of Biomech. Eng.*, Vol. 136, No. 1, pp. 011010-011010, 2013.
- 1.12. D. Kouzoudis, C. Grimes, "The frequency response of magnetoelastic sensors to stress and atmospheric pressure," *Smart Mat. Struct.*, Vol. 9, No. 6, pp 885-889, 2000.

- 1.13. E.L. Tan, B.D. Pereles, K.G. Ong, "A wireless embedded sensor based on magnetic higher-order harmonic fields: application to liquid pressure monitoring," *IEEE Sens J.*, Vol. 10, No. 6, pp. 1085-1090, 2010.
- 1.14. N.P. Oess, B. Weisse, B.J. Nelson "Magnetoelastic strain sensor for optimized assessment of bone fracture fixation," *IEEE Sens J.*, Vol. 9, No. 8, pp. 961-968, 2009.
- 1.15. M.K. Jain, S. Schmidt, K.G. Ong, C. Mungle, C.A. Grimes, "Magnetoacoustic remote query temperature and humidity sensors." *Smart Mater. Struct.*, Vol. 9, pp. 502-510, 2000.
- 1.16. Q.Y. Cai, A. Cammers-Goodwin, C.A. Grimes, "A wireless, remote query magnetoelastic CO<sub>2</sub> sensor," *J. Environ. Monit.*, Vol. 2, pp. 556-560, 2000.
- 1.17. Q.Y. Cai, M.K. Jain, C.A. Grimes, "A wireless, remote query ammonia sensor." *Sens. Actuat. B. Chem.*, Vol. 77, pp. 614-619, 2001.
- 1.18. Q.Y. Cai, C.A. Grimes, "A remote query magnetoelastic pH sensor," *Sens. Actuat. B Chem*, Vol. 71, pp. 112-117, 2000.
- 1.19. Q.Y. Cai, K.F. Zeng, C.M. Ruan, T.A. Desai, C.A. Grimes, "A wireless, remote query glucose biosensor based on a pH-sensitive polymer." *Anal. Chem.*, Vol. 76, pp. 4038-4043, 2004.
- 1.20. C.M. Ruan, K.F. Zeng, O.K. Varghese, C.A. Grimes, "Magnetoelastic immunosensors: amplified mass immunosorbent assay for detection of *Escherichia coli*" *Anal. Chem.*, Vol. 75, pp. 6494-6498, 2003.
- 1.21. C.M. Ruan, K.F. Zeng, O.K. Varghese, C.A. Grimes, "A staphylococcal enterotoxin B magnetoelastic immunosensor." *Biosens. Bioelect.*, Vol. 2, pp. 138-144, 2004.
- 1.22. L.G. Puckett, G. Barrett, D. Kouzoudis, C.A. Grimes, L.G. Bachas, "Monitoring blood coagulation with magnetoelastic sensors." *Biosens. Bioelect.*, Vol. 16, pp. 675-681, 2003.

- 1.23. Libby G. Puckett, Gary Barrett, Dimitriz Kouzoudis, Craig Grimes, Leonidas G. Bachas, “Monitoring blood coagulation with magnetoelastic sensors”, *Biosens Bioelect.*, Vol. 18, pp. 675-681, 2003.
- 1.24. Ee Lim Tan, Brandon D. Pereles, Ranyuan Shao, Justin Ong, and Keat Ghee Ong, “A wireless, passive strain sensor based on the harmonic response of magnetically soft materials,” *Smart Materials and Structures*, Vol. 17, No. 2, pp. 025015, 2010.
- 1.25. B. Pereles, A. DeRouin, J. Jiang, K.G. Ong, “Partially loaded magnetoelastic sensors with customizable sensitivities for large force measurements,” *IEEE Sens. J.*, Vol. 15, No.1, pp. 591-597, 2015.
- 1.26. S.R. Green, Y.B. Gianchandani, “Tailored magnetoelastic sensor geometry for advanced functionality in wireless biliary stent monitoring systems,” *J. Micromech. Microeng.*, Vol. 20, 2010.

## 2. Magnetoelastic Detection Theory and Device Development

As stated in Chapter 1, magnetoelastic sensors have been proposed as medical sensors in a variety of applications; however, one of the fundamental barriers to widespread acceptance and implementation of this technology (even beyond medical applications) is the absence of a cost-effective detection device targeted at monitoring these sensors in their intended detection mode.

### 2.1. Magnetic Materials Theory

In order to understand the operation of magnetoelastic materials for sensing applications, it is necessary to build an understanding of the behavior of magnetic materials. For a magnetic material to operate as a repeatable sensor, it has to have a consistent output for any given input; its current output does not depend on previous loading conditions. Therefore, the most desirable starting point for a magnetic sensor is to utilize what is referred to as a “soft” magnetic material. A perfectly soft magnetic material is a material that magnetizes when exposed to a magnetic field and demagnetizes completely when the field is removed (no previous “magnetic memory”). This concept can be visualized in the  $BH$  loop shown in **Figure 2.1a**, which shows the magnetic flux density  $B$  (incident magnetic field  $H$  plus magnetization  $M$ ) as a function of applied magnetic field  $H$ . In contrast, a “hard” magnetic material (**Figure 2.1b**) will magnetize up to a certain threshold (saturation magnetization  $H_s$ ) when exposed to an applied field, but will have some remaining field after the field is removed known as the remanence,  $H_r$ . An additional magnetic field of opposite polarity would then be required to demagnetize the material, which is known as the coercive force,  $H_c$ . The ideal magnetic material for use in most sensing applications would exhibit a minimum hysteresis, and thus, zero remanence and coercive force.

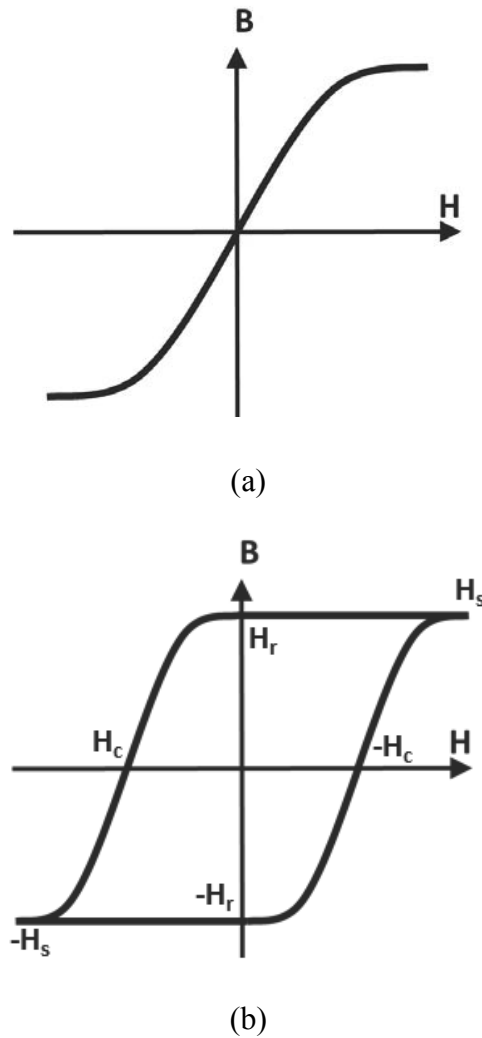


**Figure 2.1.** (a) BH-Loop of a soft magnetic material (b) BH-Loop of a hard magnetic material.

While there are a variety of different magnetic parameters that can be used in sensing applications, the focus of this work is on materials exhibiting magnetoelastic properties. Magnetoelasticity refers to the coupling of magnetic and elastic/mechanical energies within the material. In other words, magnetoelastic materials exhibit a mechanical change with an applied magnetic field and a magnetic change when exposed to a mechanical stimulus. Specifically, a stress applied to the material will change its magnetic permeability  $\mu$ , which is the slope of the linear portion of the  $BH$  characteristic.

Conversely, an applied magnetic field will result in a change in the material's dimensions as given by [2.1]:

$$\varepsilon = \frac{\sigma}{E} + \frac{3}{\lambda_s} \left( \frac{H^2}{H_k} - \frac{1}{3} \right) \quad \text{where } H < H_k \quad (2.1)$$

Where  $\varepsilon$  is the induced strain,  $\sigma$  is the longitudinal stress,  $E$  is the Young's modulus,  $\lambda_s$  is the saturation magnetostriction,  $H$  is the applied magnetic field, and  $H_k$  is the anisotropy field. The strain resulting from an applied magnetic field is known as the material's magnetostriction, while the change in the material's Young's modulus is known as the  $\Delta E$  Effect. The magnetostrictive and  $\Delta E$  effects occur due to rotation of magnetic domains within the material on an atomic level. The rotation of the magnetic domains to align with the applied field direction causes a stretching along the direction of the field and also induces an internal strain on the material that causes the change in the material's elasticity.

In magnetoelastic materials, the reverse situation is also true; an applied stress changes their anisotropy,  $H_k$ , and their susceptibility,  $\chi$ , according to [2.2]:

$$H_k = \frac{2K_u - 3\lambda_s\sigma}{M_s} \quad (2.2)$$

$$\chi = \frac{M_s^2}{2K_u - 3\lambda_s\sigma} \quad (2.3)$$

which is known as the Villari Effect. The susceptibility of the material is directly related to its magnetic permeability by [2.2]:

$$\mu = \mu_0(1 + \chi) \quad (2.4)$$

For materials with positive magnetostriction, as will be discussed in future chapters, an increase in applied stress causes an increase in magnetic permeability.

## 2.2. Magnetoelastic Resonance Detection

The most common method for magnetoelastic sensor detection reported in literature today is by monitoring the sensor resonance as a function of the parameter of interest. Like any mechanical structure, a magnetoelastic sensor exhibits a mechanical

resonance behavior depending on its mass, elasticity, and any damping forces applied. The typical rectangular resonant sensor will have resonant frequencies as given by [2.3]:

$$f_n = \frac{n}{2L} \sqrt{\frac{E}{\rho(1-\nu^2)}} \quad n = 1, 2, 3 \dots \quad (2.5)$$

where  $E$  is the Young's modulus,  $\rho$  is the density of the material,  $L$  is the length of the rectangular sample,  $\nu$  is the Poisson's ratio and  $n$  indicates that resonance occurs at integer multiples of the fundamental resonant frequency ( $n=1$ ) as shown in **Figure 2.2**. For Metglas 2826MB, a commonly used magnetoelastic thick film, the resonant frequencies for sensors from 1 mm to 100 mm resonate in the range of about 22 kHz (at 100 mm) to 2.2 MHz (at 1 mm).

Application of an external magnetic field causes the magnetic domains in the material to rotate along the direction of the field through the Villari Effect. This, in turn, causes the material to exhibit an elongation in the direction of the applied field. Upon excitation with a sinusoidal magnetic field, the material will exhibit a longitudinal vibration. At the mechanical resonant frequency, constructive acoustic wave energy will cause a maximum in vibration amplitude, thus causing the permeability of the material to rise. Since the acoustic wave propagation corresponds to the magnetic domain orientation, the sensor produces a secondary magnetic flux which exhibits a local maximum at mechanical resonance. This can be detected in a number of ways; most of which center around detecting the current generated on a detection coil through Faraday's Law.

### 2.2.1. Impedance Measurement

One method for measuring the resonant frequency of a magnetoelastic sensor is through the measurement of a detection solenoid with the magnetoelastic material acting as the solenoid core. As the sensor approaches resonance, the magnitude of the permeability changes, thus increasing the inductance of the coil given by:

$$L = \frac{\mu N^2}{l} \quad (2.6)$$

where  $\mu$  is the permeability of the core,  $N$  is the number of turns of wire, and  $l$  is the length of the solenoid. Various methods can be used to ascertain the coil inductance as a function of frequency, including commercial impedance analyzers or network analyzers. However, these pieces of equipment can be costly (\$10000+) especially when concerned with higher frequency ranges and high detection amplitude/frequency resolution. These devices typically determine the impedance of the coil by applying a known signal and measuring its reflectance/transmission.

### 2.2.2. Frequency Domain Measurement

Frequency domain detection is also possible for monitoring the resonant frequency of magnetoelastic sensors. One form of frequency detection used to monitor the sensors is to apply a known excitation sinusoid and monitor the detection response at each frequency. Fourier transformations applied to the response are used to determine the detection amplitude as the applied sinusoidal field is stepped through a range of frequencies. The resulting frequency spectrums corresponding to each excitation frequency can be compared, where the highest amplitude will correspond to the resonant frequency.

Another method can be employed which implements a technique known as “lock-in amplification.” Lock-in amplification relies on multiplication of the detected signal with a phase-locked reference signal. The result of multiplying sine waves is as follows:

$$A_1 \sin(\omega_1 t_1 + \theta_1) * A_2 \sin \omega_2 t_2 + \theta_2 = \tag{2.7}$$

$$\frac{1}{2} A_1 A_2 \cos((\omega_1 - \omega_2) t + \theta_1 - \theta_2) - \frac{1}{2} A_1 A_2 \cos((\omega_1 + \omega_2) t + \theta_1 + \theta_2)$$

Therefore, multiplying sinusoidal components of two signals at the same frequency will produce a signal component at twice the frequency and a signal component at 0 Hz (DC) as given by:

$$A_1 \sin(\omega t_1 + \theta_1) * A_2 \sin(\omega t_2 + \theta_2) = \frac{1}{2} A_1 A_2 - \frac{1}{2} A_1 A_2 \cos(2\omega t + \theta_1 + \theta_2) \tag{2.8}$$

By implementing a high roll-off low-pass filter, only the DC component of the signal will remain corresponding to the component of the detection signal at the reference frequency as:

$$\frac{1}{2}A_1A_2 \quad (2.9)$$

Utilizing this concept, lock-in detection multiplies a known reference sinusoid with the detected signal to achieve a very narrow-band filter with amplification. By setting the excitation signal as the reference signal and scanning through a number of frequencies, the resonant frequency of a magnetoelastic sensor (maximum magnitude) can be discerned.

Lock-in amplifiers have the advantage of extremely narrow-band detection. However, they sacrifice detection speed due to long time constants on their low-pass filters and phase-locking circuits. Regardless, they are still fast enough for use in biomedical applications where detection speed is not a primary concern. However, like previously described detectors, lock-in amplifiers are relatively expensive. Additionally, very few lock-in amplifiers exist for frequencies above about 125 kHz, which correspond to sensors about 20 mm in length (anything smaller would not be detectable). Currently, the only device fitting this description on the market is a Sanford Research Systems SRS844 high frequency lock-in amplifier, which is priced at \$8450.

### 2.2.3. Time-Domain Measurement

Another method for measuring the resonant frequency of the magnetoelastic sensor is by analyzing its damping characteristics over time. In this type of system, a pulse of known excitation frequency and magnitude is applied for a set duration and is then removed. The vibrating sensor continues to vibrate in a “ring-down” pattern after the excitation is removed as shown in **Figure 2.2**. As the excitation frequency approaches the sensor resonant frequency, the acoustic energy storage in the material will increase. Thus, the starting vibration amplitude and resulting magnetization signal of the sensor will

increase. Therefore, by monitoring the time it takes for the ring-down response to decay over a range of frequencies, the resonant frequency can be determined.

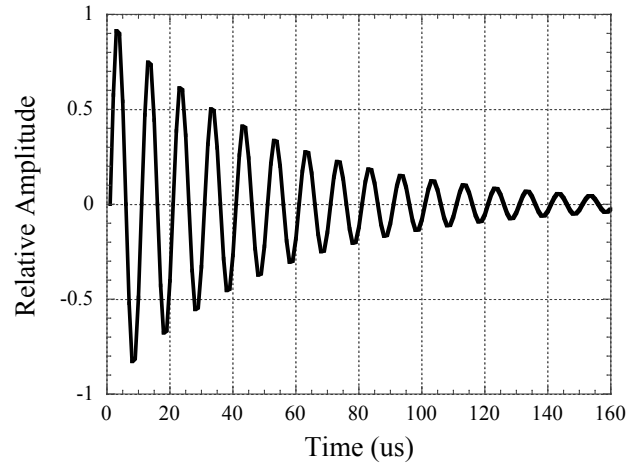


**Figure 2.2.** Typical shape of a ring-down response of a magnetoelastic after the excitation field is removed.

## 2.3. Threshold-Crossing Detection Device

In applications proposed in later chapters, a wearable patient-centered detection device would be needed in order to effectively monitor the parameter of interest. While currently devices have been proposed for interrogating these sensors, none have been proven as a low-cost option, causing magnetoelastic sensing platforms to be ignored in commercial applications. Therefore, a low-cost detection device was designed and fabricated for detection of magnetoelastic sensors in resonant mode. The device functioned based on the ring-down detection as described in **Section 2.1.3**. The excitation and detection circuitry is described in the following sections.

### 2.3.1. Threshold-Crossing Circuit

A Texas Instruments MSP430f2618 microcontroller controlled all functions of the circuit and was used to communicate through 128kBaud RS232 communication to a

MATLAB graphical user interface on a PC. An AD5932 direct digital synthesis (DDS) function generator chip was chosen for signal generation due to its 1 Hz frequency resolution, programmable frequency sweep, and high frequency range (20 MHz) and communicated to the microcontroller using 4-wire SPI communication. The digital-to-analog (DAC) output of the AD5932 chip was filtered and amplified to smooth and condition the signal for power amplification. A variable-gain stage was included to allow for flexibility when using a variety of different detection coils. A class-AB output stage in the feedback loop of an LF353 operational amplifier provided the excitation signal to the excitation/detection coil using TIP41C and TIP42C bipolar junction transistors for power amplification. The 12-bit DAC output of the MSP430f2618 microcontroller was added to the AC signal prior to power amplification using a summing circuit to allow for software-programmable DC bias control.

An ADG452 digital switch was used to connect the excitation circuit to the coil. The detection circuit was also connected through the digital switch in order to allow software-controlled switching between excitation and detection circuitry. This was necessary for quickly and repeatedly detecting the ring-down response before it was dissipated.

The detection circuitry consisted of an AD624 instrument amplifier input stage set to a gain of 500 followed by a bandpass filtering stage with corner frequencies (-3dB) at 10 kHz and 1.5 MHz. The filtered output was then amplified with a variable-gain stage to allow modification for different detection coil types. An AD8564 high-speed comparator was implemented with two thresholds set by digital potentiometers. The thresholds were implemented to allow software-controlled sensitivity thresholds.

The comparator outputs of the AD8564 were connected to two MSP430 input/output pins configured as inputs with bi-directional interrupts (high-to-low and low-to-high). A graphical user interface is shown in **Figure 2.3**. As illustrated, the user was able to set parameters for the frequency sweep in addition to the duration of each test. After the sweep, the GUI displayed the combined number of times that the ring-down

signal crossed the threshold level for each threshold. The option to apply a 3-point moving average filter was also included. The GUI calculated the resonant frequency by determining the maximum point in the filtered data in order to eliminate error due to noise peaks around the actual maximum.

The logical flow of the device function is as follows. The PC GUI sends the device parameters to the microcontroller and waits for the collected data to be sent back. The microcontroller then tells the function generator to start generating the excitation signal. After 250  $\mu\text{s}$ , the output of the excitation circuit is connected to the coil, and after 250  $\mu\text{s}$  of applying the excitation signal to the coil it is then disconnected and unpowered. At the same time, the detection circuit is connected. 20  $\mu\text{s}$  is allowed before data is collected to wait for the detection circuit to stabilize. The data is collected for 10 ms (or more depending on user input) and the data is transmitted over serial communication to the GUI, where it is saved, processed, and displayed.

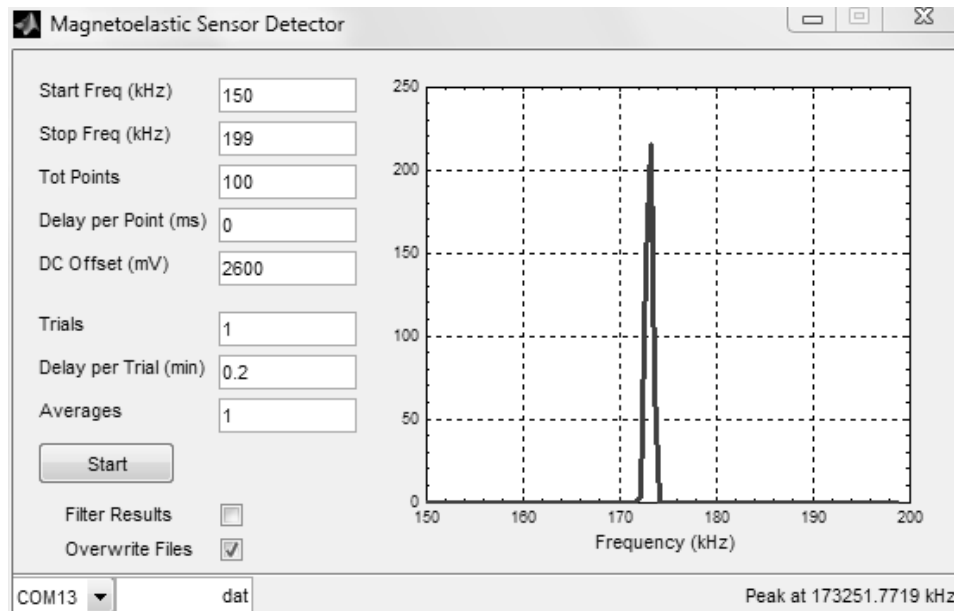


**Figure 2.3.** Image of the magnetoelastic resonance sensor detector

The device presented here is a practical, low-cost solution for sensing magnetoelastic sensors in resonant mode. Although previous work has described devices for monitoring sensors in this mode in the past [2.4, 2.5], they were designed for use in a research lab rather than a commercial application where cost-effectiveness is critical. **Table A1** in the **Appendix** shows the bill of materials for this device. The cost of building an individual device is currently \$196.76. But fabrication in bulk (1000+) is as low as \$91.84 per device. With this type of system, hospitals could reasonably lend these devices out to patients on a basis similar to what is currently implemented with heart-monitoring systems.

## 2.4. Magneto-Harmonic Detection

Because the permeability of magnetoelastic materials changes with applied stress, the amplitude of the magnetization of the sensor will increase with stress given a constant excitation magnetic field. The magnetization field will consist of multiple frequency components due to the material's nonlinear magnetization curve; specifically a sinusoidal excitation field will result in a magnetoelastic sensor magnetization field composed of components at the excitation frequency in addition to frequency components at multiples, or harmonics, of the excitation frequency. The resulting signal in terms of its frequency components can be written as [2.6]:

$$B(h) = C_0 + \sum_{n=1}^{\infty} 2|b_n| \cos\left(\frac{nh}{h_{AC}} + \phi\right) \quad (2.10)$$

where  $B$  is the magnetic flux,  $C_0$  is a DC offset,  $b_n$  is the coefficient of the  $n^{\text{th}}$  order,  $h$  is the applied AC field, and  $\phi$  is the phase angle.

Work by Ong and colleagues showed that the harmonic amplitude of the  $n^{\text{th}}$  order harmonic can be determined by [2.7]:

$$A_n = \frac{iB_s\omega}{\pi^2} |e^{jn\pi H_{dc}} \cos(\pi n) - \kappa \sin \frac{1}{\kappa}| \quad (2.11)$$

$$\kappa = \frac{h_{ac}B_s}{n\pi(B_S H_k - 3\lambda_s \sigma)} \quad (2.12)$$

where  $A_n$  is the amplitude of the  $n$ th order harmonic,  $H_{dc}$  is the applied DC biasing field,  $\iota$  is the coupling between the sensor and the coil,  $B$  is the magnetic flux density,  $\omega$  is the radian frequency,  $H_k$  is the anisotropy field,  $\lambda_s$  is the saturation magnetostriction, and  $\sigma$  is the stress applied to the sensor. Typically, spectral analysis involving envelope detection or Fourier Transform methods are implemented to analyze the harmonic response. It is also possible to use the lock-in detection method described in **Section 2.12** to monitor a single frequency component of the response at a time.

## 2.5. Harmonic Detection Device

A low-cost detection device was designed and fabricated for monitoring the harmonic response of magnetoelastic sensors. The harmonic detection device operated by implementing time-domain signal acquisition followed by a Fourier Transform of the data to obtain the frequency spectrum of the sensor response. The desired detection range was 200 Hz corresponding to a frequency range sufficiently above 60 Hz wall noise to filter yet low enough to minimize frequency-dependent hysteresis loss. Excitation and detection circuitry are detailed in the following sections.

### 2.5.1. Harmonic Excitation Circuit

A block diagram overview of the detection device is shown in **Figure 2.4**. A MATLAB graphical user interface (GUI) was generated to communicate with the MSP430f2618 microcontroller onboard the detection circuit PCB which also controlled the excitation circuit. A Wein Bridge Oscillator circuit was created to produce a 200 Hz sinusoidal signal. The Wein Bridge Oscillator output was amplified and filtered in order to smooth the signal and provide adequate voltage to the following power amplification circuit. Due to the nature of harmonic detection, it was critical that harmonics in the excitation signal were minimized in order to prevent detection of false sensor harmonics at the detection circuit input. An OPA548 was chosen for power amplification due to its 5

A current output per channel, wide supply range, thermal shutdown safety feature, and stability when driving inductive loads. A variable gain stage was also implemented to accommodate for different coil configurations, where higher coil impedance generally requires a higher excitation circuit output.

A DC excitation circuit and coil were also included in the device design. The DC excitation field, which was connected to an independent DC excitation coil wound concentrically over the AC excitation coil, was generated by amplifying the MSP430 microcontroller's digital-to-analog converter output using LF353 general purpose op amps as well as a second OPA548 amplifier. The DC biasing field generated by this circuit added the capability for software-controlled DC biasing sweeps to locate the maximum amplitude response corresponding to each harmonic frequency component.

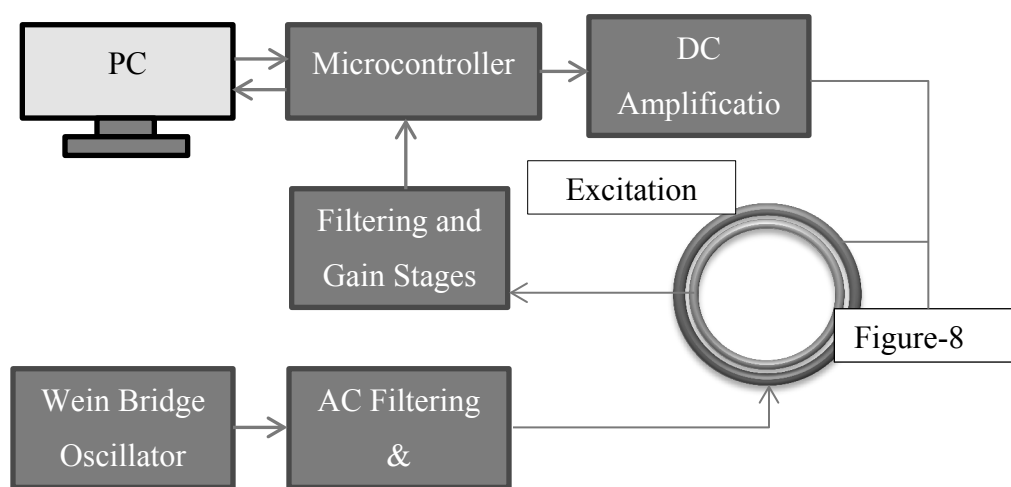


**Figure 2.4.** Flowchart depicting the functionality of the magneto-harmonic detection device.

### 2.5.2. Harmonic Detection Circuit

Since the goal of the harmonic detection circuit was to monitor the response at the harmonics of the 200 Hz excitation signal, A 10<sup>th</sup> order filtering stage was used to amplify and filter the detection signal using LF353 general purpose amplifiers. The filter

was comprised of 4 bandpass Sallen-Key filtering stages as well as 2 Sallen-Key low-pass filtering stages. The primary concerns for the filtering stages was the removal of 60 Hz wall noise, 200 Hz excitation signal, and undesired high-frequency noise commonly encountered in areas with wireless communication devices. A 60 Hz notch filter was also included to further attenuate power line noise. The 10<sup>th</sup> order circuit was simulated in OrCAD Capture SPICE software and the frequency response is shown in **Figure 2.5**.

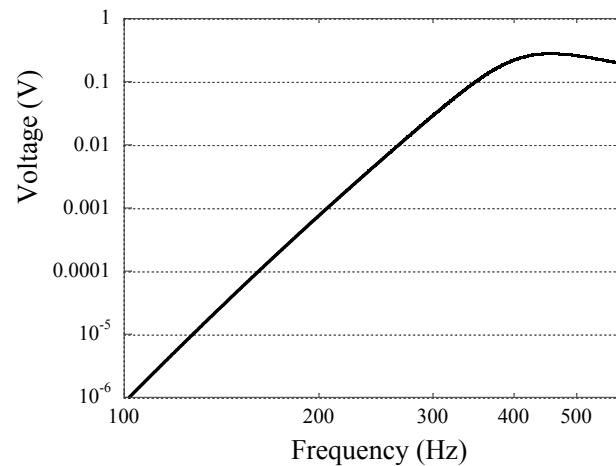


**Figure 2.5.** Theoretical frequency response of the 10<sup>th</sup> order harmonic detection filter.

The MATLAB graphical user interface, as shown in **Figure 2.6**, allows control of the circuit via communication to the MSP430 microcontroller. Specifically, the user interface allows control of a variety of parameters including: number of 200 Hz periods to collect data over, number of points per period, the DC current, and the internal MSP430 reference to use (1.5 V for signals less than 1.5 V to improve resolution and 2.5 V for larger signals). The GUI also displays a graph of the time-domain response collected as well as the Fast Fourier Transform output. A second GUI was also created for DC biasing field sweeps as shown in **Figure 2.7**. For reference, the response of the same 6mm long Metglas 2826MB sensor was measured by an Agilent 4396B spectrum/network analyzer using an excitation field generated by a Fluke 271 function

generator amplified by a Tapco J1400 audio amplifier. The resulting response is shown in **Figure 2.8** as the “unloaded” signal.

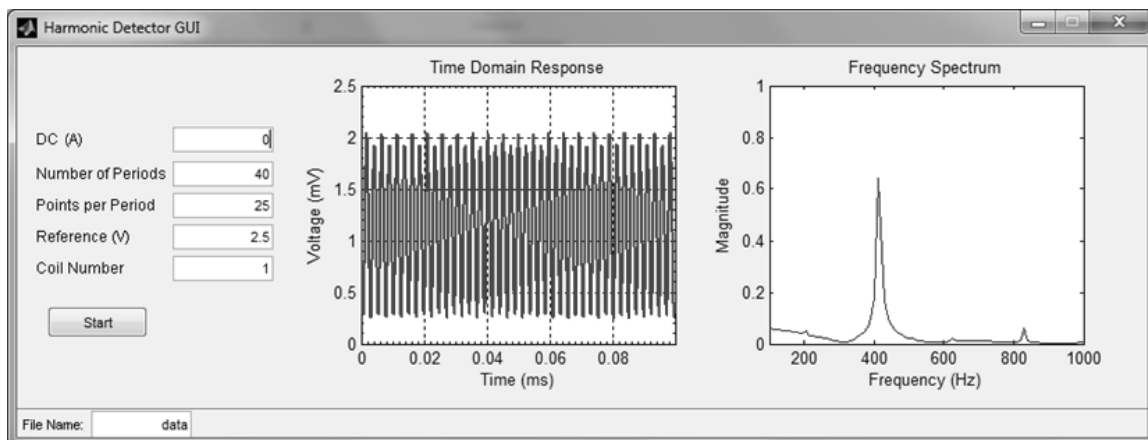


**Figure 2.6.** Visual depiction of the magneto-harmonic detector graphical user interface monitoring a 6 mm long Metglas 2826MB sensor.

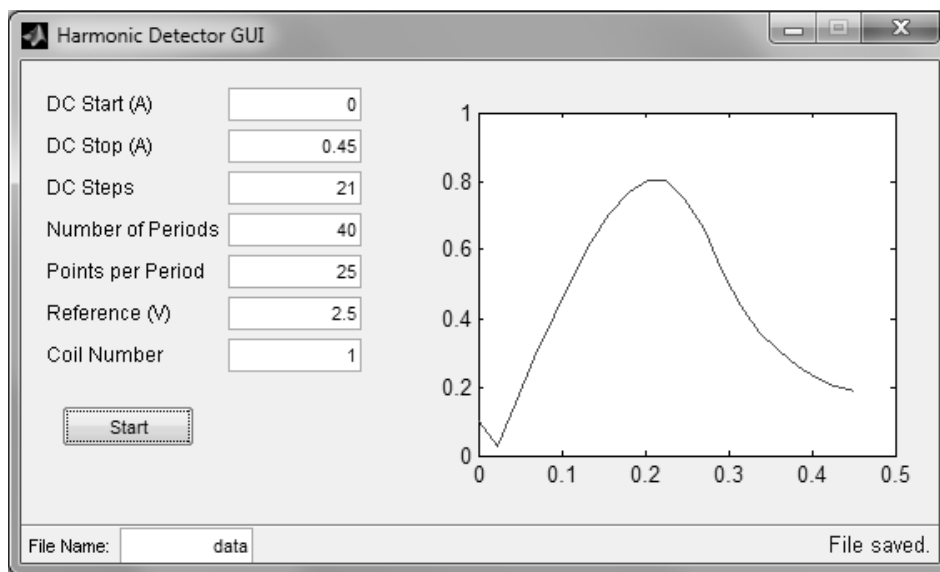


**Figure 2.7.** The DC Biasing sweep graphical user interface measuring a 6 mm long Metglas 2826MB strip.

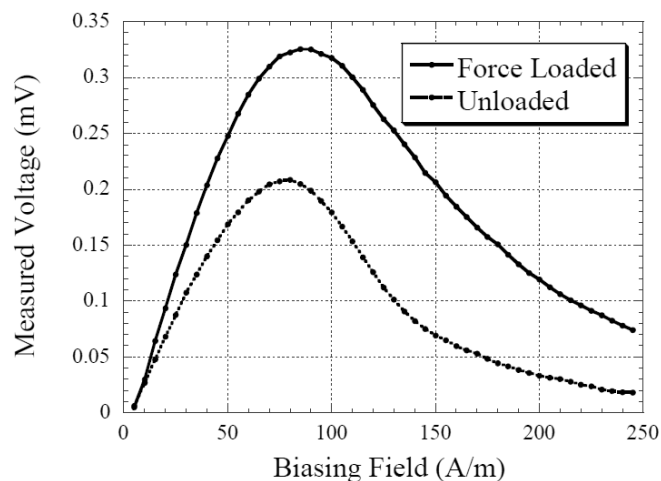


**Figure 2.8.** The 6 mm long Metglas sensor response as detected by commercial equipment.

The particular implementation described here does not necessarily represent a device with novel detection range or functionality. However, by designing the device to function in the narrow detection range of the sensor in addition to removing extra functionality of commercial equipment, this device does serve as evidence that a low-cost detection device can be fabricated for use in portable applications (such as wearable or home-monitoring applications). The result is that magneto-harmonic detection, which has previously been claimed as a low-cost detection method due to low sensor costs (less than \$1 per sensor using Metglas 2826 MB), more feasible with a low-cost detection system also in place. A bill of materials (BOM) is provided in **Table A2** of the **Appendix**. Given in the table are the components used in the device as well as their cost when purchased in bulk (1, 100, or 1000 parts). The overall cost for one device is \$153.41 when produced as a stand-alone unit, but if produced in bulk (1000+) would be under \$70 each including PCB fabrication and packaging costs.

## References

- 2.1. K.G. Ong, C.A. Grimes. Magnetostrictive Nanomaterials for Sensors. *ChemInform*, Vol. 35 No. 37, 2004.
- 2.2. K.E. Elkins, Fabrication of Iron-platinum Ferromagnetic Nanoparticles. 2008: ProQues. 153.
- 2.3. C.A. Grimes, C.S. Mungle, K. Zeng, M.K. Jain, W.R. Dreschel, M. Paulose, K.G. Ong, “Wireless magnetoelastic resonance sensors: a critical review,” *Sensors.*, Vol. 2, pp. 294-313, 2002.
- 2.4. K. Zeng, C.A. Grimes, “Threshold-crossing counting technique for damping factor determination of resonator sensors,” *Review Sci. Inst.*, Vol. 75, No. 12 pp. 5257-5261, 2004.
- 2.5. H. Xie, Y. Chai, S. Horikawa, S. Li, B.A. Chin, H. C. Wickle III, “A pulsed wave excitation system to characterize micron-scale magnetoelastic biosensors,” *Sensors and Actuators A: Physical*, Vol. 205, pp. 143-149, 2014.
- 2.6. K.G. Ong, and C.A. Grimes, “Tracking the harmonic response of magnetically-soft sensors for wireless temperature, stress, and corrosive monitoring.” *Sens Actuators A Phys*, Vol. 101 No.1, pp. 49-61, 2002.
- 2.7. Cullity, B.D. and Graham, C.D., Introduction to Magnetic Materials. 2009: Wiley

### **3. Geometrical Modification of Magnetoelastic Sensors to Enhance Sensitivity**

Nina Pacella, Andrew DeRouin, Brandon Pereles, Keat Ghee Ong\*  
Department of Biomedical Engineering, 1400 Townsend Drive, Houghton MI 49931,  
USA.

#### **Abstract**

The magnetoelastic sensor is a wireless, passive sensor platform typically comprised of a strip of magnetoelastic material that exhibits a mechanical vibration when under the excitation of a magnetic AC field. At the resonant frequency, the vibration of the sensor is most prominent, generating a significant secondary magnetic field that can be detected with a remotely located coil. Biological and chemical sensing can be realized by functionalizing a mass- or elasticity-changing coating on the magnetoelastic sensor, causing a shift in the resonant frequency when exposed to the target analyte. To date, most magnetoelastic sensors are rectangular and are designed to sense a uniform coating over the entire sensor surface. This paper presents a new magnetoelastic sensor design with higher sensitivity, achieved by applying non-uniform coatings and altering the sensor to a triangular shape. In addition, the new design allows the magnetoelastic sensor to form a sensor array that requires only a fraction of sample volume for multi-parameter sensing compared to the current sensor design.

This material was previously published in *Smart Materials and Structures*

### 3.1. Introduction

Magnetoelastic sensors are a class of wireless, passive sensors based on resonating structures of magnetoelastic/magnetostrictive materials. When exposed to an excitation magnetic field, the magnetoelastic sensor vibrates, generating a secondary magnetic field that can be independently monitored. Since the vibration of the sensor is sensitive to mechanical loading, physical parameters such as stress, force, and liquid flow have been monitored by tracking the changes in the resonant frequency of the sensor [3.1-3.3]. Additionally, chemical and biological sensing can be achieved by applying a coating on the sensor surface that responds to the target of interest by changing its mass or elasticity, thus converting non-physical information into quantities that the sensor can detect. Using different functionalization schemes, magnetoelastic sensors have also been deployed for detecting biological and chemical quantities such as glucose, *E. coli*, anthrax, salmonella, pH, ammonia, etc. [3.4-3.9]. Due to their numerous attractive qualities, magnetoelastic sensors are ideal for many applications [3.10]. For example, since they are powered remotely with magnetic fields, magnetoelastic sensors can be interrogated without direct physical or optical links. As a result, they are ideal as embedded sensors where directly accessing them would be difficult, if not impossible. This sensor technology is also inexpensive, making it suitable for single use or applications requiring a large array of sensing elements.

Sensitivity and selectivity are important qualities for sensors. A sensor with good selectivity allows differentiation of a specific target from other interferences, which eliminates many pre-measurement processes (to remove interference analytes) and allowing the sensor to be used in a complex medium such as inside a human body, agricultural products, etc. A sensor with high sensitivity allows it to detect a small quantity of target, leading to improvements in accuracy and resolution. Many investigations have been conducted to improve the performance of the magnetoelastic sensor for use in novel applications [3.11,3.12]. However, most of these investigations rely on the same sensor structure, which is a rectangular, free standing magnetoelastic

strip, and focus on uniform loading over the sensor surface. For magnetoelastic sensors of rectangular design can be approximately described as [3.7]:

$$\frac{\Delta f}{f_0} = -\frac{\Delta m}{2M} \quad (3.1)$$

where  $\Delta f$  is the change in resonant frequency,  $f_0$  is the resonant frequency prior to the mass loading,  $\Delta m$  is the change in mass and  $M$  is the mass of the sensor. The negative sign indicates the decrease in resonant frequency with applied mass due to damping. As evident in Eq. (3.1), the sensitivity of the sensor towards mass loading is proportional to the mass of the sensor. This indicates that small sensors will be more sensitive to a smaller mass change. However, since the resonant frequency is higher for a smaller sensor, it needs to operate at higher frequencies to detect small mass change. This creates additional challenges in the detector design and fabrication process (making a high frequency detector is more complicated, requiring more expensive components, and is more susceptible to noise). In addition, smaller sensors produce smaller magnetic fields, thus requiring a more sensitive detector.

This work focuses on combining the unique properties of magnetoelastic materials and novel designs for realizing a sensor system with higher sensitive and selectivity without reducing the sensor size. A new improvement of the sensor described here is an enhanced sensitivity achieved by changing shape from rectangular to triangular. Furthermore, for most magnetoelastic sensors, the chemical/biological recognition layer is usually coated over the entire surface of the sensor. However, as will be shown in this paper, not all areas of the sensor are equally sensitive and placing the test sample at a specific area of the sensor (rather than uniformly coated all over the sensor) could lead to an increase in sensitivity.

## 3.2. Experiments

### 3.2.1. Triangular Sensors versus Rectangular Sensors

The new magnetoelastic sensor is a long triangle, where the test sample and sensing coating is placed at the tip of the narrow end of the triangle (see **Figure 3.1a** and **3.1d**). The magnetic field is applied in parallel to the length of the triangle, resulting in a sensor that vibrates in the same direction. A simple model is shown in **Figure 3.1a – 3.1c** to demonstrate the increase in sensitivity of a triangular magnetoelastic sensor compared to a rectangular sensor when a localized loading is applied at one end. As shown in **Figure 3.1a**, the mass loading is applied at the tip of the triangular sensor with a surface area of  $A_l$  (see **Figure 3.1a**). To compare between triangular and rectangular sensors, two loading configurations are considered. Specifically, a thin strip of coating is applied to the rectangular sensor along the length (**Figure 3.1b**) and along the width (**Figure 3.1c**). The coating on rectangular sensor covers a surface area of  $A_0$  (see **Figure 3.1b** and **3.1c**). By assuming the same coating mass is applied on the triangular sensor and the rectangular sensor (surface area and thickness held constant) with a strip of coating along the length:

$$A_l = A_0 \quad (3.2)$$

The effect of the geometrical changes on the sensor is illustrated in **Figure 3.1**. A rectangular sensor can be modeled as number of length-wise, thin regions physically connected in parallel as shown in **Figure 3.1a-3.1c**. For a rectangular sensor, if a mass load is applied at the end of the sensor but does not fully cover the width of the sensor (e.g. the region  $A_0$  depicted in the **Figure 3.1b**), only the region bordering the coating, which in this case, rectangular region with a width of  $a$ , is affected by the loading. Conversely, for a triangular sensor with a mass covering the whole width of its tip, the loading affects the whole width of the sensor,  $w$ . Therefore, the ratio of triangular to rectangular sensor sensitivity can be approximated by comparing the widths of their affected regions for both sensors as:

$$\frac{S_1}{S_0} = \frac{w}{a} \quad (3.3)$$

where  $S_1$  and  $S_0$  are the mass sensitivities for the triangular and rectangular sensors, respectively. Since the sensor is a right-angled triangle,  $d/c = w/L$ . The coating area at the triangular sensor (**Figure 3.1a**) can then be determined as:

$$A_1 = \frac{cd}{2} = \frac{wc^2}{2L} \quad (3.4)$$

Similarly, the coating area at the rectangular sensor (**Figure 3.1b**) is:

$$A_0 = ca \quad (3.5)$$

Rearranging Eq. (3.4) and Eq. (3.5), and substituting into Eq. (3.3) along with Eq. (3.2) yields:

$$\frac{S_1}{S_0} = \frac{w}{a} = \frac{2A_1L/c^2}{A_0/c} = \frac{2L}{c} \quad (3.6)$$

Eq. (6) indicates that compared to the traditional rectangular sensor, the sensitivity of a triangular sensor can be theoretically increased by a dimensional factor  $L/c$ . The model used to derive Eq. (4) assumes no vibration energy loss from the asymmetry of the triangular sensor and no coupling among the vibrations across the width of the rectangular sensor. In reality, both assumptions are not ideal and hence the actual signal increase is less than that predicted from Eq. (4). However, Eq. (4) is still useful for sensor design. Specifically, Eq. (4) points to that a long triangular sensor with a small coating footprint would have a higher sensitivity. Therefore, for a fixed sensor length ( $L$ ), the sensitivity of a triangular sensor can be further increased by reducing the length of the coated region, while there is no such sensitivity improvement for a rectangular sensor. Using a similar analysis for the widthwise coated rectangular sensor (**Figure 3.1c** and **3.1f**) and assuming the coated surface area is the same for the triangular sensor and widthwise coated rectangular sensor, the ratio of their sensitivities can be derived as:

$$S_1/S_0 = w/d \quad (3.7)$$

Eq. (7) indicates that a smaller coating area for the triangular sensor can lead to higher sensitivity compared to the widthwise coated rectangular sensor.

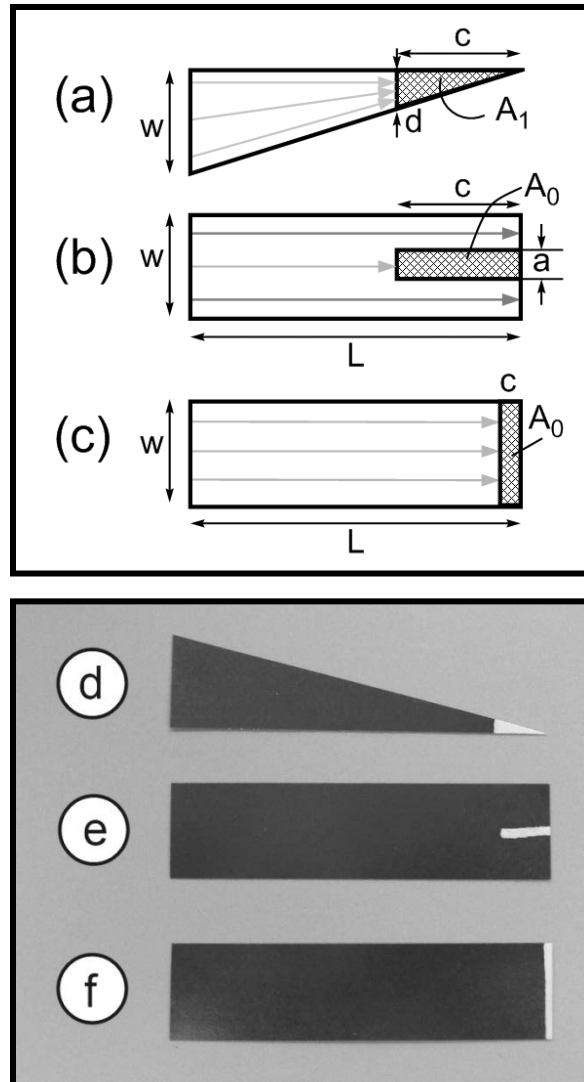


**Figure 3.1.** (a) For a triangular sensor, a coating at the tip affects the vibrations of the whole sensor (indicated by green arrows). (b) A rectangular sensor with the same volume/mass of coating along the length only leads to a narrow strip with width of  $a$ , thus only the region with coating affects the sensor vibrations (indicated by the green arrow). This led to a lower sensitivity compared to the triangular sensor. (c) A rectangular sensor with the same volume/mass of coating across the width at one end of sensor has lower sensitivity compared to a triangular

sensor because the vibrating energy of the triangular sensor focuses at a narrower width of  $d$  but the vibrating energy of the rectangular sensor has to focus at the full width of the sensor  $w$ . The photographs of the (d) triangular sensor, (e) lengthwise coated sensor, and (f) widthwise coated sensor are also shown.

### 3.2.2. Sensor Fabrication and Calibration

Metglas 2826MB ( $\text{Fe}_{40}\text{Ni}_{38}\text{Mo}_4\text{B}_{18}$ ) was purchased from Metglas Inc as a continuous ribbon of 12.7 mm in width and 30  $\mu\text{m}$  in thickness. Metglas 2826MB is a commonly used magnetoelastic material with a saturation magnetostriction (maximum change in dimension under magnetic field) of 12 ppm. This material is magnetically soft and has a magnetic permeability of 50,000 for an as-cast sample. Magnetoelastic sensors used in this experiment were mechanically sheared from the ribbon into the desired shape. To examine the sensor response with increasing loading, a layer of acrylic enamel (Plaid Enterprise) was painted at the tip of the triangular sensor (**Figure 3.1d**), and at one of the ends of the rectangular sensor (**Figure 3.1e** and **3.1f**). The mass of the coating was determined by taking the difference of the sensor weights before and after the coating.

The experimental setup, similar to the setup in other previous work [3.13], is illustrated in **Figure 3.2**. A Fluke 271 function generator was used to generate a sine wave of varying frequencies, and the signal was amplified by a Tapco Juice 1400 amplifier. The captured signal from the sensor, at each frequency point, was fed to a lock-in amplifier (Stanford Research System SR810) to measure its magnitude and phase. The excitation coil was made of two serial-connected coils forming a Helmholtz configuration. Each coil was 28 cm in diameter, 50 in turns and was made of 18 gauge laminated copper wires. The excitation field strength was 100 A/m for all tests. The detection coil consisted of two 17.6 cm  $\times$  12.0 cm opposite-wound coils, each with 100 turns of 36 gauge copper wire. A custom Visual Basic 6.0 program was used to control the frequency sweep operation. The magnitude of the signal measured by the lock-in

amplifier was plotted against frequency, and the resonant frequency was determined as the frequency that corresponded to the largest signal magnitude.

Triangular and rectangular sensors were fabricated to examine their respective sensitivities towards mass loading. For the triangular sensor,  $L = 46$  mm,  $w = 12.7$  mm and  $c = 5$  mm. For the rectangular sensors,  $L = 56$  mm,  $w = 12.7$  mm,  $c = 5$  mm, and  $a = 1$  mm. Note that the coating area of the triangular sensor was smaller than that of the rectangular sensor. To compensate for the difference in coating areas (and therefore mass), the sensitivity of the sensor was defined as the change in coating mass,  $\Delta m$ , over the mass of the sensor  $M$ . Therefore, the sensor was more sensitive if the ratio  $\Delta m/M$  was higher, regardless of the sensor size. In other words, all measurements were normalized to the mass change to compensate for the difference in coating area.

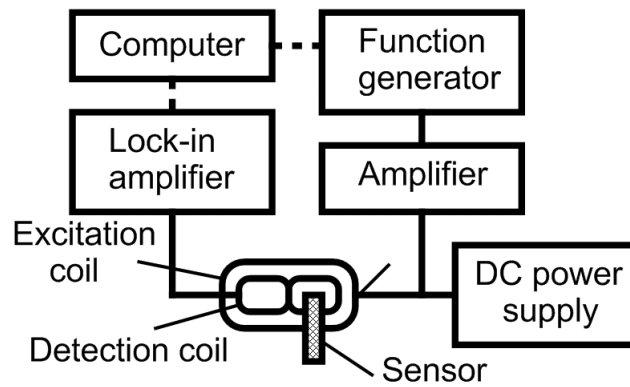


**Figure 3.2.** Experimental setup for characterizing the mass sensitivities of the triangular and rectangular sensors.

### 3.2.3. Sensor Array Fabrication and Demonstration

With triangular design, a polar array of sensors can be formed so that only a small amount of test sample is needed for all sensors at their tips. **Figure 3.3** is a photograph of the sensor holder designed for a maximum of eight sensors. The holder was printed with a V-flash 3D modeler (3D Systems, Rock Hill, SC), and painted with acrylic enamel (Walmart's fast dry gloss spray paint) to prevent test liquid from seeping into the holder. The diameter of the holder was 56 mm. The sensors were arrayed with their tips pointed towards the center. The lengths and widths of the sensors, from the largest to the smallest, were 23.41 mm and 3.23 mm, 21.25 mm and 3.15 mm, 19.31 mm and 3.35 mm, 17.75 mm and 3.45 mm, 16.05 mm and 2.75 mm, 15.05 mm and 3.73 mm, 14.35 mm and 3.73 mm, 14.35 mm and 3.44 mm and 12.85 mm and 3.19 mm, respectively. To simultaneously interrogate all sensors, a spiral coil was placed at the bottom of the sample holder as shown in **Figure 3.3**. The spiral coil was made of 26 gauge tightly wound laminated copper wire, had 50 turns, and had an inner diameter of 12 mm and outer diameter of 55 mm.

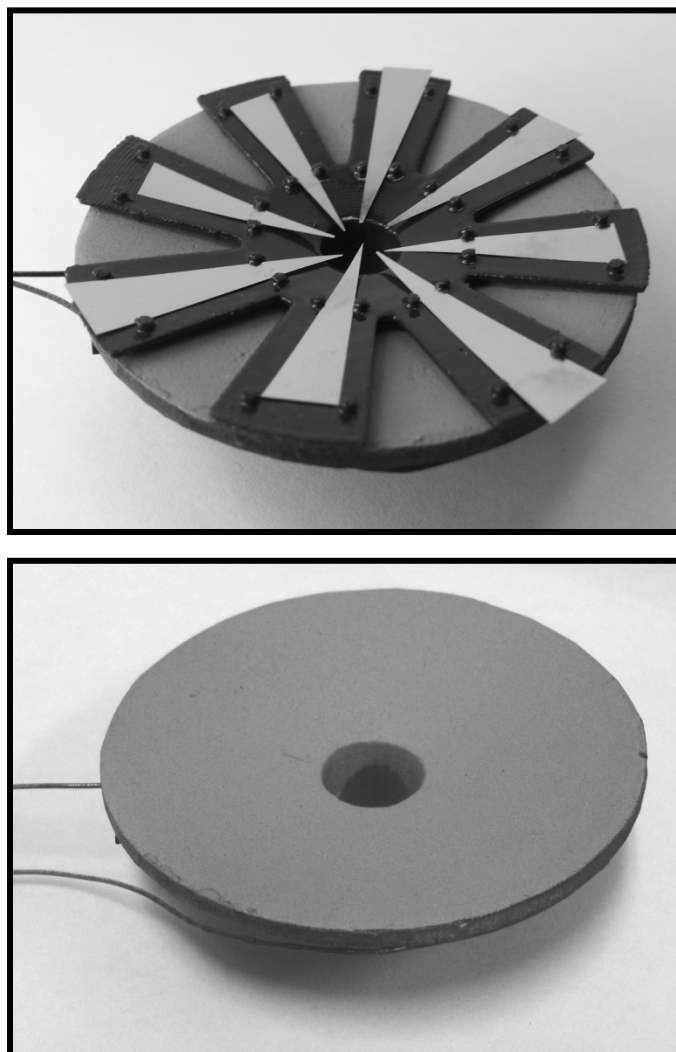


**Figure 3.3.** A photograph of the triangular sensor array (a) with the sensor holder and (b) with only the spiral detection coil. The triangular sensors form a polar array in to a “flower” pattern. The center of the array is the testing area that exposed the sample to all sensors.

Customized electronic circuits were fabricated to monitor the sensor array. **Figure 3.4** illustrates the block diagram of the circuits. A microcontroller (Texas Instruments MSP 430) controlled a function generator to produce a sinusoidal signal for 8 ms to vibrate the sensor. The excitation signal was then turned off, allowing the sensor to experience an exponentially decaying vibration. The sensor signal (sinusoidal pulses with

a decaying exponential profile) at 100  $\mu\text{s}$  after turning off the excitation signal was passed through two comparators at 50 mV and 100 mV. The numbers of pulses detected from both comparators were summed to determine the signal amplitude at each frequency. The function generator continued to increase the frequency and capture the sensor's signal amplitudes at all frequencies to construct the resonance plot; the resonant frequency was determined as the frequency with the largest signal amplitude.

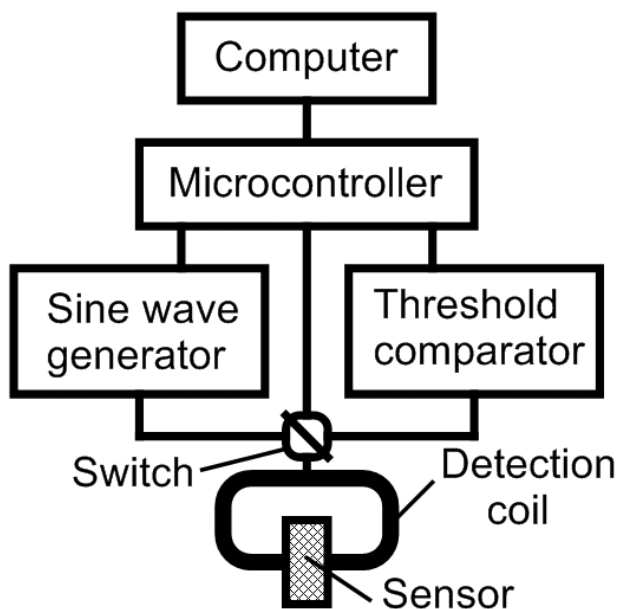


**Figure 3.4.** Block diagram of the custom detector that measured the resonant frequencies of the sensor array.

An experiment was conducted to demonstrate the functionality of the sensor array. Four triangular sensors, with length and width of 28.5 mm and 7.0 mm (Sensor A), 25.2 mm and 6.2 mm (Sensor B), 23.3 mm and 5.3 mm (Sensor C), and 21.3 mm and 5.5 mm (Sensor D), respectively, were placed in the same holder shown in **Figure 3.3** with an empty slot between two adjacent sensors. The tip of Sensor A was coated with watercolor paint (Daler Rowney) that was water soluble, and Sensor C was coated with oil paint (Daler Rowney) that was not water soluble. Sensor B and Sensor D were uncoated. Distilled water was placed at the testing chamber of the sensor holder,

submerging all four sensor tips. The resonant frequencies of the four sensors were then measured as a function of time.

### 3.3. Results and Discussions

**Figure 3.5** plots the mass loading sensitivity of rectangular sensors with various coating conditions (complete coating, partial coating along the length, and partial coating along the width), as well as sensitivity of the triangular sensor. As expected, the rectangular sensor with complete coating on its surface has the lowest sensitivity (slope =  $20 \text{ kHz}\cdot\text{M} / \Delta\text{m}$ ) compared to the partially coated sensors. The rectangular sensor with coating along its width has a slightly larger sensitive (slope =  $48 \text{ kHz}\cdot\text{M} / \Delta\text{m}$ ) than the one with coating along its length (slope =  $38 \text{ kHz}\cdot\text{M} / \Delta\text{m}$ ). Nevertheless, all partially coated rectangular sensors have at least two times the mass sensitivity than the sensor with complete coating. Compared to the rectangular sensors, the sensitivity of the triangular sensor (slope =  $165 \text{ kHz}\cdot\text{M} / \Delta\text{m}$ ) was 3 to 4 times larger than the rectangular sensors. This observation confirms the trend described in Eq. (4) and (5). However, the sensitivity increase was smaller than predicted in the equations due to the effects in the triangular sensor that were not included in the derivation of the equations. For example, since the coated region of the rectangular sensors was physically connected to the rest of the strip, it experienced some damping effect from the mass. Nevertheless, **Figure 3.5** is a clear indication that the triangular sensor had a larger sensitivity when the coating was applied to the tip of the narrow end of the sensor.

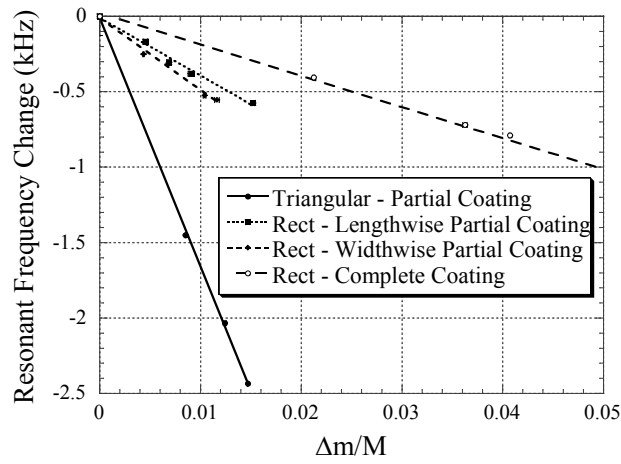


**Figure 3.5.** Mass sensitivity of a triangular sensor, a rectangular sensor with a strip coated along its length, a rectangular sensor with a strip coated along its width, and a fully coated rectangular sensor. The triangular sensor showed the highest sensitivity compared to the rectangular sensors, while the fully coated rectangular sensor has the lowest mass sensitivity. The error bars represent standard deviation of 3 measurements.

**Figure 3.6** demonstrates the effect of coating area on mass sensitivity of the triangular sensor. By increasing the length of the coating ( $c$  in **Figure 3.1**) while keeping the sensor's length  $L$  constant, the sensitivity of the sensor decreased. This is consistent with Eq. (3.4), which indicated the sensitivity of a triangular sensor should increase with smaller value of  $c$  compared to  $L$ .

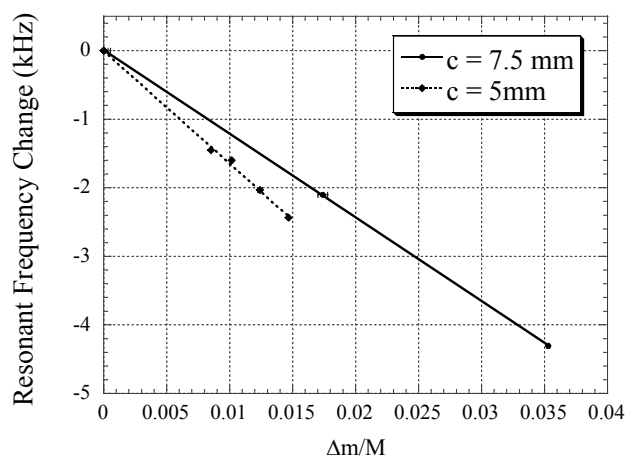
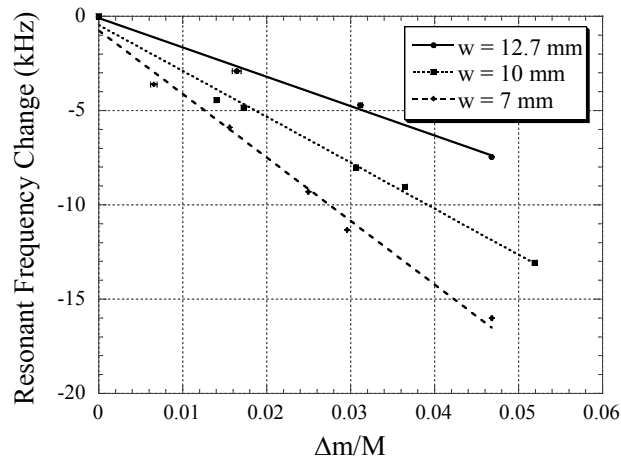
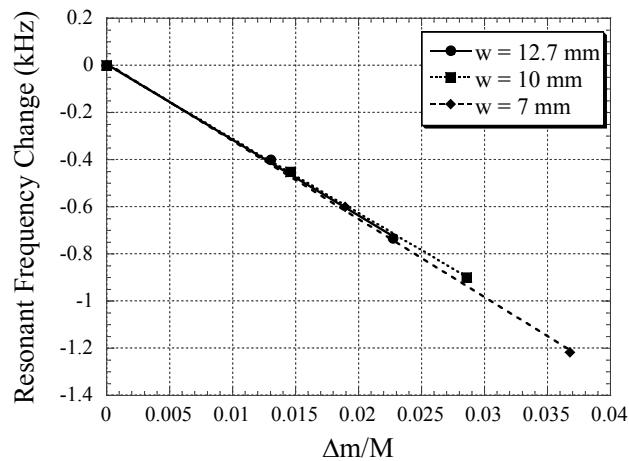


**Figure 3.6.** Mass sensitivity of a triangular sensor when the length of the coating area,  $c$ , was 5 mm and 7.5 mm. Increasing  $c$ , corresponding to larger coating area, resulted in a reduction of sensitivity. The error bars represent standard deviation of 3 measurements.

**Figure 3.7** depicts the effects of varying the width on the sensitivity of the triangular and rectangular sensors with a lengthwise partial coating. **Figure 3.7a** shows that a sensor with smaller width has a higher mass sensitivity. In contrast, for the rectangular sensor, the sensor's width has little to no impact on the sensor's sensitivity, see **Figure 3.7b**. This allows the sensitivity of the triangular sensor to be further increased by reducing the width of the triangle.



(a)



(b)

**Figure 3.7.** Sensitivity of the (a) triangular sensor and (b) rectangular sensor with different widths. For the triangular sensor, decreasing the width further increased the sensitivity; while for the rectangular sensor, the width has no effect on the sensor's sensitivity. The error bars represent standard deviation of 3 measurements.

**Figure 3.8** illustrates the frequency spectrum of eight triangular sensors in the sample holder shown in **Figure 3.3**. The eight resonant peaks in the figure were from eight sensors of different lengths, with the lowest frequency corresponding to the longest

sensor. Note that the amplitudes of the lower resonant frequencies were higher. This was because the sensors with lower frequencies have larger volumes of magnetoelastic material to generate more vibrations under the same excitation field, thus leading to more magnetic field generation. In addition, since longer sensors overlapped more turns of the detection coil, they captured more excitation field and their responses were picked up by more turns of the coil. This directly increased their signal amplitudes.

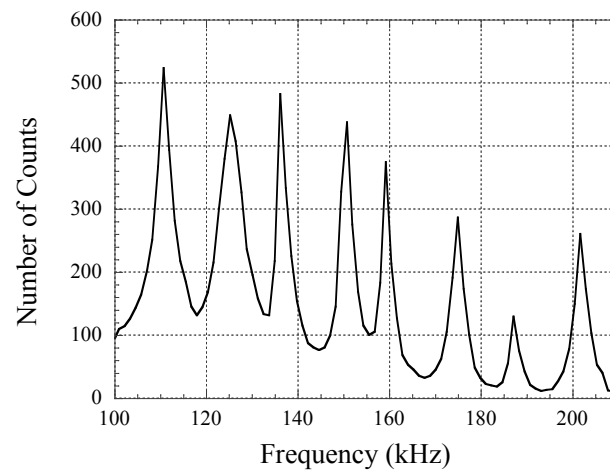


**Figure 3.8.** The frequency spectrum of a sensor array consisting of 8 sensors of different lengths. The resonance peaks of the larger sensors were higher than the smaller sensors.

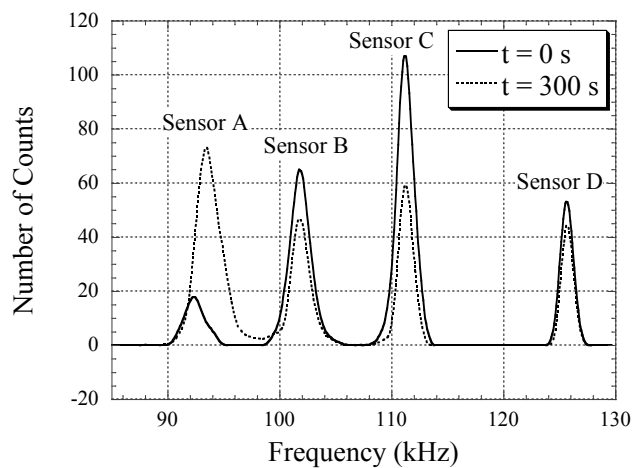


**Figure 3.9.** The frequency spectrum of a four-sensor array immediately after adding water and at the end of experiment (300 s). The tip of Sensor A was coated with a water soluble layer and the tip of Sensor C was coated with a non water-soluble layer.

**Figure 3.9** plots the frequency spectrum of four sensors, two coated with paint (one oil-based, one water-based) and two uncoated, at the beginning and 300 s after exposure to water. At 300 s, the resonant frequency of Sensor A increased significantly due to the degradation of the water-soluble coating. In contrast, Sensor C, which was coated with a non-soluble coating, did not demonstrate a noticeable resonant frequency shift, which indicated the coating was intact (confirmed visually). The resonant frequencies of the control sensors, Sensor B and D, remained unchanged throughout the experiment. The amplitude of the resonance for Sensor A increased after the coating dissolved. This was due to the reduction of damping from the coating as it dissolved. In contrast, the amplitudes of the rest of sensors decreased after the coating from Sensor A dissolved. This was due to the release of the coating into the medium, which slightly increased the viscosity of the solution. The viscosity change was not enough to cause the resonant frequency change but did affect the resonant amplitudes of other sensors. Although the viscosity increase in the medium also reduced the resonant amplitude of Sensor A, the effect of coating dissolving, which increased the resonant amplitude, was much larger

than the viscosity change. Therefore, the net change on Sensor A was an increase in resonant amplitude. **Figure 3.10** graphs the resonant frequencies of the sensors over time. The graph indicates that only Sensor A showed an increased in resonant frequency due to the degradation of the water-based paint, while the resonant frequencies from the other three sensors remained constant.

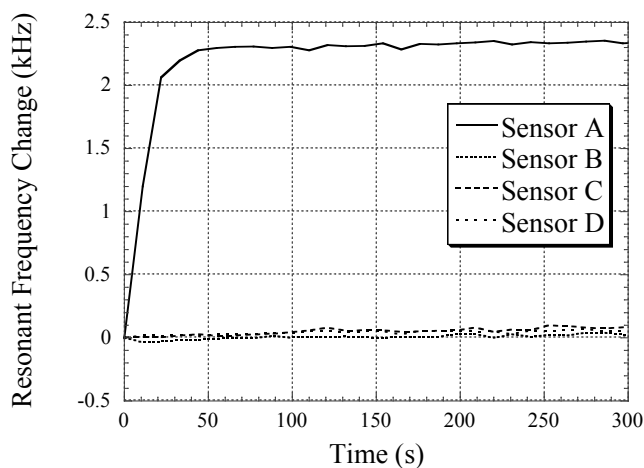


**Figure 3.10.** The change in resonant frequencies of the four sensors as a function of time. The resonant frequency for Sensor A increased due to the degradation of the water soluble coating.

### 3.4. Conclusions

A new technique for improving the sensitivity and arraying capability of the magnetoelastic sensor has been presented. Experimental results have shown that by depositing on a certain area of the sensor instead of the whole surface, the sensitivity towards mass loading was increased. In addition, by changing the shape of the sensor to triangular instead of rectangular, the mass sensitivity of a sensor with aspect ratio of about 4 has increased by at least 3 times. Furthermore, the sensitivity of the triangular magnetoelastic sensor can be increased if the aspect ratio is increased. For example, with the aspect ratio of the sensors increased to about 7, the sensitivity of the triangular sensor was found to be more than 11 times better than their rectangular counterparts. These results are evidence that changing the loading area and shape of the sensor are promising

techniques for significantly improving the mass sensitivity of the magnetoelastic sensor. The new design will lead to fabrication of biological or chemical sensors for detection of glucose, pH, *Bacillus anthracis*, and others following the techniques described in [3.4-3.9]. The new design would retained the selectivity as those described in [3.4-3.9], but with higher sensitivities without changing the coating or sensor size.

In addition to increased sensitivity, triangular magnetoelastic sensors can also be formed into a polar array with their tips concentrated in a small region. As a result, only a small quantity of test samples is needed for all sensors. A detection apparatus, including a new sensor holder, a spiral coil, and a custom electronics, have been fabricated and tested to demonstrate the feasibility of this sensitive magnetoelastic sensor array with a minimized sample size.

## References

- 3.1 D. Kouzoudis, C.A. Grimes, "Remote query fluid-flow velocity measurement using magnetoelastic thick-film sensors," *J. Appl. Phys.* Vol. 87, pp. 6301, 2000
- 3.2 D. Kouzoudis, C.A. Grimes , "The frequency response of magnetoelastic sensors to stress and atmospheric pressure," *Smart Materials and Structures*, Vol. 9 No. 6, pp. 885, 2000.
- 3.3 C.A. Grimes, P.G. Stoyanov, D. Kouzoudis, K.G. Ong, "Remote query pressure measurement using magnetoelastic sensors," *Review of Scientific Instruments* Vol. 70 No. 12, pp. 4711-4714, 2000.
- 3.4 Q.Y. Cai, M.K. Jain, C.A. Grimes, "A wireless, remote query ammonia sensor," *Sens. Actuators B*, Vol. 77, No. 3, pp. 614-619, 2001.
- 3.5 Q.Y. Cai, C.A. Grimes, "A salt-independent pH sensor," *Sens. Actuators B*, Vol. 79, No. 2, pp. 144-149, 2001.
- 3.6 X. Gao, W. Yang, P. Pang, S Liao, Q. Cai, K. Zeng, C.A. Grimes, "A wireless magnetoelastic biosensor for rapid detection of glucose concentrations in urine samples," *Sens. Actuators B*, Vol. 128 No. 1, pp. 161-167, 2007.

- 3.7 J. Wan, M.L. Johnson, R. Guntupalli, V.A. Petrenko, B.A. Chin, "Detection of *Bacillus anthracis* spores in liquid using phage-based magnetoelastic micro-sensors," *Sens. Actuators B*, Vol. 127, No. 2, pp. 559-566, 2007.
- 3.8 R. S. Lakshmanan, R. Guntupalli, J. Hu, V.A. Petrenko, J. M. Barbaree, B.A. Chin, "Detection of *Salmonella typhimurium* in fat free milk using a phage immobilized magnetoelastic sensor," *Sens. Actuators B*, Vol. 126, No. 2, pp. 544-550, 2007.
- 3.9 C. Ruan, K. Zeng, O.K. Varghese, C.A. Grimes, "Magnetoelastic immunosensors: amplified mass immunosorbent assay for detection of *Escherichia coli*," O157:H7 *Anal Chem*. Vol. 75, No. 23, pp. 6494-6498, 2003.
- 3.10 C.A. Grimes, C.S. Mungle, K. Zeng, M.K. Jain, W.R. Dreschel, M. Paulose, K.G. Ong, "Wireless magnetoelastic resonance sensors: a critical review," *Sensors*, Vol. 2 pp. 294-313, 2002.
- 3.11 K.G. Ong, C.S. Mungle, C.A. Grimes, "Control of a magnetoelastic sensor temperature response by magnetic field tuning," *IEEE Trans. Magnetics*, Vol. 39 No. 5, pp. 3414-3416, 2003.
- 3.12 S. Schmidt, C.A. Grimes, "Characterization of nano-dimensional thin-film elastic moduli using magnetoelastic sensors," *Sens. Actuators A*, Vol. 94 No. 3 pp. 7, 2001.
- 3.13 B. Pereles, A. DeRouin, J. Jiang, K.G. Ong, "Partially loaded magnetoelastic sensors with customizable sensitivities for large force measurements," *IEEE Sens. J.*, Vol. 15, No.1, pp. 591-597, 2015.

## **4. Multi-parameter Sensing with a Single Magnetoelastic Sensor by Applying Loads on the Null Locations of Multiple Resonant Modes**

Andrew DeRouin and Keat Ghee Ong\*

Biomedical Engineering, Michigan Technological University, Houghton MI 49931, USA.

### **Abstract**

Magnetoelastic sensors are mass sensitive sensors commonly used for stress and pressure measurement, as well as chemical and biological monitoring when combined with a functionalized coating. Magnetoelastic sensors are typically made of free-standing, rectangular strips of magnetoelastic materials that exhibit longitudinal, extensional vibrations due to the excitation of magnetic fields. A single magnetoelastic sensor is generally used to monitor one parameter since only the fundamental resonant frequency is measured. Multiple-parameter sensing in close proximity has previously been achieved by using multiple magnetoelastic sensors of different dimensions and tracking their resonant frequencies independently. However, this requires a large surface area and inconvenient layout of dissimilarly shaped sensors. This paper presents a technique for monitoring multiple parameters with a single magnetoelastic sensor by applying separate mass loads at the null points (points of zero vibration) of multiple resonant modes. Applying a load at a null location does not affect the corresponding resonant mode but alters the resonant frequencies of other modes. Therefore, by isolating the variables of interest to multiple null points and simultaneously measuring the resonant frequency shifts of related resonant modes, the masses at each null location can be calculated. Results showed that changing the coverage at a null location along

This material was previously published in *Smart Materials and Structures*

the width of the sensor can be used to minimize the loading effect on the corresponding resonant mode. In contrast, changing the lengthwise coverage can maximize the loading effect on other resonant modes, thus increasing the mass sensitivity of the sensor. Furthermore, simultaneously applying loads to null points of multiple resonant modes had a nearly additive effect, allowing detection of multiple parameters with a single magnetoelastic sensor.

#### **4.1. Introduction**

Magnetoelastic materials are characterized by their ability to change physical dimension in response to magnetic fields, as well as change their magnetic properties due to exposure to physical forces. Therefore, by magnetically activating these materials and monitoring their magnetic responses, magnetoelastic materials have been used as physical sensors, and with proper functionalization, chemical and biological sensors. Various types of sensors are based on the magnetoelastic materials, which can be designed to exhibit different vibration modes leading to different sensor characteristics. A common design, known as the magnetoelastic cantilever, is to use the magnetoelastic material as a part of a bi-layer cantilever [4.1-4.2]. In this case, one end of the cantilever is fixed to a support while the other is left free-hanging. A magnetic field is applied along the length of the cantilever, causing the magnetoelastic piece to apply a longitudinal force to the whole piece. Since the secondary layer attached to the magnetoelastic material does not respond to the magnetic field, the net effect is to cause a flexural strain. The largest flexural strain will be produced at the free end of the cantilever; hence, the sensing component is usually placed there [4.1-4.2].

Another popular configuration is a rectangular, free-standing magnetoelastic strip where the magnetic field is applied along its length [4.3-4.12]. This is the most commonly reported type of magnetoelastic sensor. As a whole, their low cost, small footprint, and low sensitivity to changes in position/orientation make magnetoelastic sensors ideal for a variety of embedded applications including detection of

stress/pressure [4.3], humidity [4.4], temperature, [4.5], chemical concentrations [4.6], pH [4.7,4.8], and biological growth [4.9-4.12]. In terms of commercial applications, magnetoelastic sensor technology has been implemented on a large scale in products such as the Methode Electronics Inc. torque sensing solutions that are sold around the world.

Magnetoelastic sensors are typically placed inside a solenoid or a Helmholtz coil to experience uniform, longitudinal AC magnetic fields resulting primarily longitudinal, in-plane extensional vibrations. The ideal resonant frequencies of the sensor under such excitation conditions are:

$$f_n = \frac{n}{2L} \sqrt{\frac{E}{\rho(1-\sigma^2)}} \quad (4.1)$$

where  $n$  is the mode number,  $L$  is the length,  $E$  is the Young's Modulus,  $\rho$  is the density, and  $\sigma$  is the Poisson's ratio of the sensor material. Note that Eq. (1) assumes the sensor is only exhibiting a longitudinal vibration, and other modes of vibrations are insignificant. The equation also indicates that the sensor exhibits multiple resonant frequencies. The lowest resonant frequency of a sensor occurs at the fundamental mode ( $n = 1$ ), while the higher mode resonant frequencies ( $n > 1$ ) occur at integer multiples of the fundamental resonant frequency. To capture the resonance response of the sensor, a detection coil can be implemented to pick up the secondary magnetic field produced by the sensor, which is also at a maximum at the resonant frequencies. Since a mass load applied to the sensor acts as a damper and shifts the resonant frequencies, this phenomenon can be utilized for direct sensing of physical quantities.

The vast majority of literature regarding magnetoelastic sensing assumes a uniform load across the sensor surface at a mass much smaller than the mass of the sensor. However, several recent studies have explored alternate possibilities. For example, Pereles et al [4.13] showed that modification of the load interface can allow

measurement of masses several orders of magnitude higher than the mass of the sensor. Additionally, Pereles's work showed that alteration of the load applicator surface and geometry had a significant impact on the sensor response.

Prior work by Li and Cheng [4.14] found that monitoring odd and even order resonant modes (multiples of the excitation frequency) simultaneously can eliminate blind spots (locations of zero sensor displacement) that occur at various points across the sensor length. In the ideal case, a mass applied at one of the null locations of the magnetoelastic sensor will not cause a shift in the resonant frequency of the associated resonant modes, but by monitoring both odd and even modes simultaneously, any mass changes at these points can still be detected.

The study by Li and Cheng [4.14] confirmed that the magnitude of displacement of the sensor follows the absolute value of a cosine function across its length for any given mode. Each resonant mode exhibits maximum displacement at the sensor's edge and  $n$  locations of zero displacement, where  $n$  is the resonant mode under consideration. **Figure 4.1** illustrates this concept and shows the locations of null points for the three lowest resonant modes along the sensor length. Since masses applied at the null points have a near-zero effect on the resonant frequency of the mode corresponding to those locations but not for other modes, loads at these null points can be determined by simultaneous measurement of the resonant frequencies of multiple resonant modes. Therefore, the independent determination of masses at null points of each resonant mode allows for monitoring of multiple parameters with only a single magnetoelastic sensor.

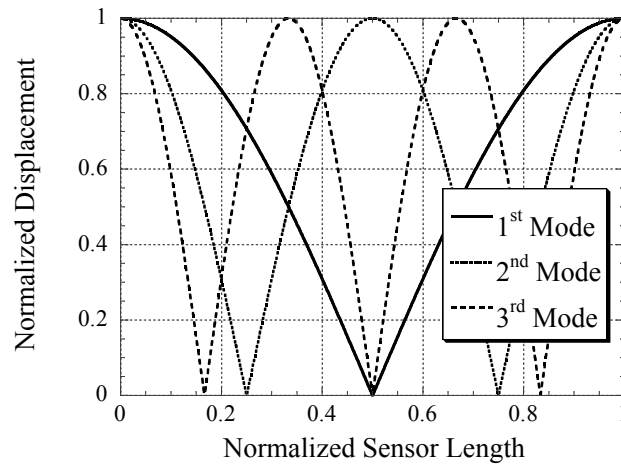


**Figure 4.1.** Magnitude of sensor displacement as a function of location for the three lowest resonant modes.

While previous studies have aimed to eliminate the blind spots in measurement resulting from the low vibrations at null point regions, this work aims to explore the opposite by using the blind spots to monitor multiple parameters simultaneously. For example, while one set of null points could be functionalized to detect alcohol vapor using  $\text{TiO}_2$  sol-gel, another set of null points could be functionalized to detect water vapor using  $\text{SiO}_2$  sol-gels [4.6]. Similarly, different sets of null locations could be functionalized with antibodies specific to a variety of different pathogens or bacteria [4.15]. Since the null points are infinitely narrow regions on the sensor, it is unclear from previous work how the sensor respond to masses that cover varied surface areas at the null locations. Therefore, this study examines the effect of changing the length and width of the coating region on the sensor response. Multiple null locations were also loaded sequentially to demonstrate the capacity to implement a single magnetoelastic sensor to monitor multiple parameters.

## 4.2. Experiments

Although the magnetoelastic strip, by itself, is usually referred to as the magnetoelastic sensor, it is actually a sensing element that needs an instrument that can provide the magnetic fields and monitor its magnetic responses. In this project, a custom magnetoelastic sensor reader, which demonstrates the portable nature of this technology, was employed for determining the resonant frequency of the sensor for all experiments. Briefly, the device performed a frequency sweep by generating a sinusoidal excitation signal at the interrogation frequency in addition to a DC biasing field. After exciting the sensor for 250  $\mu$ s, the AC excitation circuit was disconnected from the coil and a detection circuit was connected. In the absence of an external AC excitation field, the sensor experienced a “ring-down,” or an exponentially decaying vibration at its resonant frequency. The detection circuit functions by monitoring the number of times the ring-down signal crosses a predetermined threshold value. The device then switches to the next frequency increment step and repeats this process until the frequency sweep is completed. A block diagram representation of the detection device operation is shown in **Figure 4.2**. A 200-turn solenoid coil (75 mm long, 17 mm diameter) was fabricated for interrogating the sensors and a polycarbonate plate was fashioned to rest near its center. On the polycarbonate plate, another polycarbonate piece was adhered perpendicularly to act as a reference for consistent placement of the Metglas samples (20 mm offset from center for 40 mm long strips).

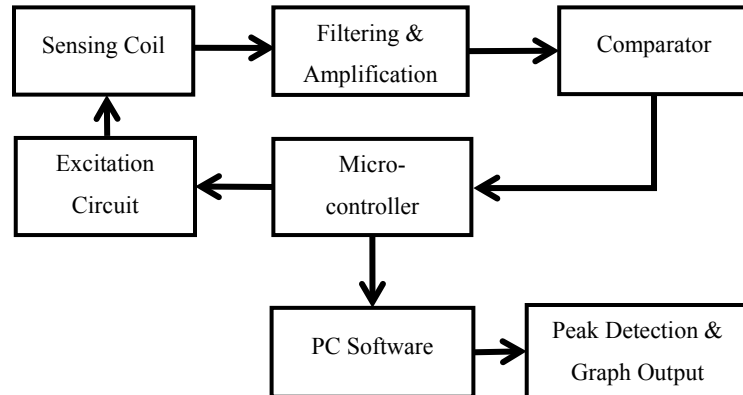


**Figure 4.2.** Flowchart of magnetoelastic sensor detection circuit. The sensing coil is driven using an AC and DC excitation circuit. After generating the excitation signal, the sensing coil is disconnected from the excitation circuit, and then connected to the detection circuit. The detection circuit counts the number of times the sensor response crosses a set threshold. Finally, the data is sent to a computer for analysis.

By definition, resonant frequencies of the sensor are the frequencies of highest energy storage (least destructive interference), which results in the highest number of threshold crossings (the longest ring-down time). If the excitation field is not at a resonant frequency (of any mode), the sensor vibration and the excitation field have a destructive interference, resulting in a very short ring-down time. In contrast, if the excitation field is at a resonant frequency of any mode, the sensor vibration synchronizes with the excitation field, leading to a long ring-down period at the frequency of the corresponding mode. For example, when the frequency of the excitation field is at the resonant frequency of the 2<sup>nd</sup> mode, the resulting ring-down frequency will also be at the resonant frequency of the 2<sup>nd</sup> mode. Note that the ring-down frequency does not affect the operation of the sensor detector since it captures the ring-down period and not the ring-down frequency.

A typical resonance profile obtained from the device is shown in **Figure 4.3**. It should be noted that in **Figure 4.3**, the resonant frequencies of the 2<sup>nd</sup> and 3<sup>rd</sup> modes are

lower than the multiple values of the 1<sup>st</sup> resonant frequency. This is due to the fact that the DC biasing field was set to 12 A/m up to 80 kHz, 50 A/m up to 120 kHz, and 60 A/m for frequencies above 120 kHz in order to increase the signal-to-noise ratio at each resonant mode (larger DC biasing fields are needed for 2<sup>nd</sup> or 3<sup>rd</sup> modes to properly bias the sensor). However, varying the DC biasing field also shifts the resonant frequency due to the  $\Delta E$  effect [4.16], which lowers the resonant frequencies at the 2<sup>nd</sup> and 3<sup>rd</sup> modes.

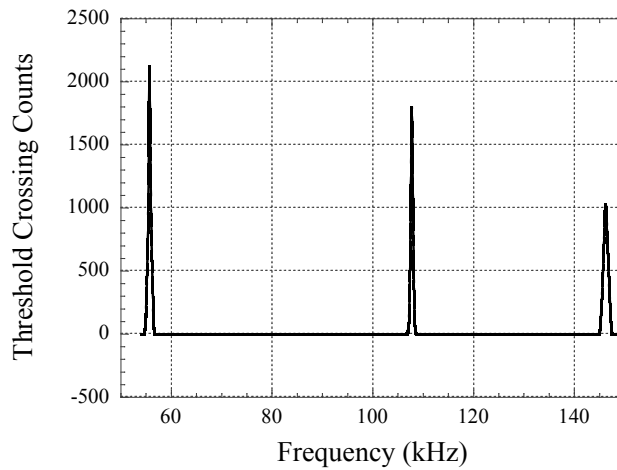
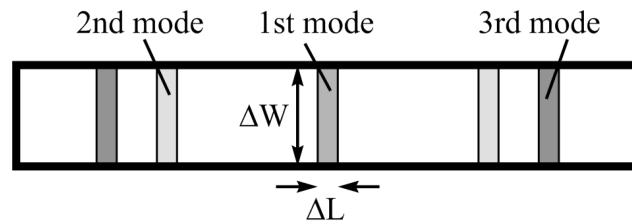


**Figure 4.3.** Frequency response obtained from a 40 mm  $\times$  12.7 mm sensor. To improve signal quality, higher DC biasing fields were used to monitor the 2<sup>nd</sup> and 3<sup>rd</sup> modes. The resulting  $\Delta E$  effect lowered the resonant frequencies of the higher resonant modes from the expected values (integer multiples of the 1<sup>st</sup> resonant frequency).

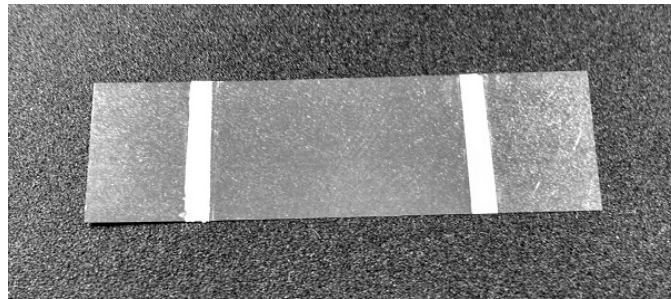
#### 4.2.1. Confirming Null Locations

The theoretical null locations of the 1<sup>st</sup>, 2<sup>nd</sup>, and 3<sup>rd</sup> resonant modes are located at  $L/2$ ,  $L/4$ , and  $L/6$  distance from the edge of the sensor, respectively (see **Figure 4.4**). However, because past studies have investigated the effects of loading these locations with masses several orders of magnitude smaller than the sensor mass, this investigation was designed to confirm the results with a mass only slightly smaller than the mass of the sensor. Two additional locations along the sensor were chosen to further confirm

that the behavior of the sensor response follows the theoretical sinusoidal displacement pattern even at higher mass loads. Samples were weighed using a Scientech SA80 digital scale to quantify mass change. In cases where modes required symmetric loading (2<sup>nd</sup> and 3<sup>rd</sup> order), each node location was painted individually and weighed to verify that symmetry was preserved within a 5% margin of error.



(a)



(b)

**Figure 4.4.** (a) Depiction of a typical magnetoelastic sensor and null locations for the 1<sup>st</sup>, 2<sup>nd</sup> and 3<sup>rd</sup> resonant modes. (b) Picture of a magnetoelastic sensor with the null locations of the 2<sup>nd</sup> resonant mode painted.

Metglas 2826MB ribbon (28  $\mu\text{m}$  thick) was sheared into 40 mm  $\times$  12.7 mm segments to produce the sensors. Each sensor was masked with an adhesive tape around the regions theorized as the null point locations. Acrylic paint (Apple Barrel 20403 white, Plaid Enterprise Inc., Norcross, GA) was applied at the null point and the excess paint was removed by sliding a small flat-edge trowel across the surface. The tape was then removed before the paint dried, thus leaving behind a strip of paint with a height

equivalent to the tape thickness (0.063 mm). The painted sensor was left open in a well-ventilated area for two hours to ensure complete drying before testing.

Five sets of three sensors each were coated with 1 mm × 12.7 mm paint sections at  $L/2$ ,  $L/3$ ,  $L/4$ ,  $L/6$  and 0 mm from each edge of the strip in order to compare the magnitudes of frequency change to the theoretical displacement values for each mode. The width of the paint located at  $L/2$ ,  $L/4$  and  $L/6$  was set at 6.7 mm based on results obtained experimentally (see **Section 4.2.2**) which showed zero frequency shift for the 3<sup>rd</sup> resonant mode. The average change in frequency normalized to change in mass was then determined for each sensor to assess how closely they correlated to the theoretical values.

#### **4.2.2. Changing width of the sensing region**

The effect of varying the mass coverage across the width of the sensor on the lowest three resonant modes was investigated. The sensors were separated into three groups with three sensors per group. For each sensor group, a 1 mm long segment was painted at  $L/2$ ,  $L/4$  or  $L/6$  from the sensor edge, corresponding to the null locations of the 1<sup>st</sup>, 2<sup>nd</sup>, or 3<sup>rd</sup> resonant modes, respectively. The resonant frequencies of the three lowest modes were measured. Next, the changes in the resonant frequencies were recorded after carefully removing 1 mm increments of paint from each side of the sensor along its width using a blade. **Figure 4.5a** illustrates this process.

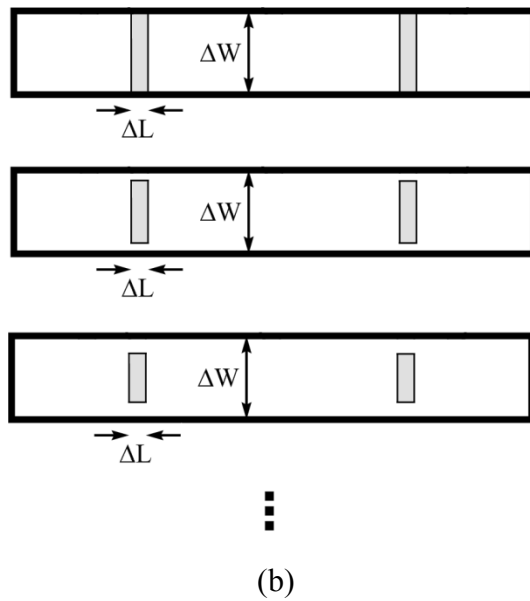
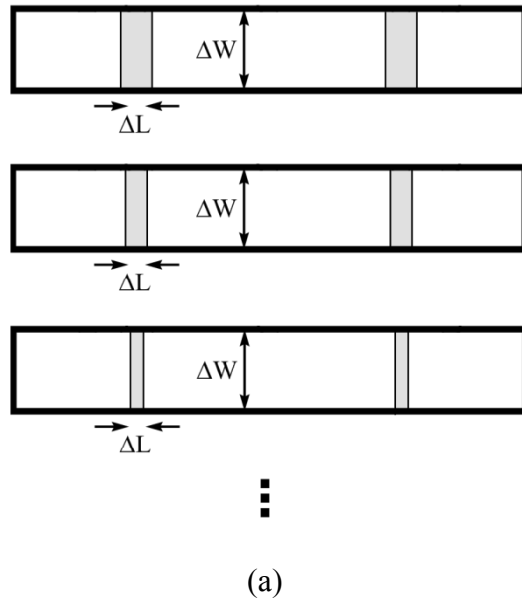


**Figure 4.5.** Illustration of the process of a) removing 1 mm of paint from each side of the 2<sup>nd</sup> resonant node locations along the width direction and b) removing 0.25 mm of paint from each side of the resonant nodes along the length direction.

### 4.2.3. Changing Length of the Sensing Region

An experiment similar to that in **Section 4.2.2** was performed to determine the effects of varying the coverage of the sensor along its length. Regions 3 mm across the sensor's length were painted on three sets of sensors (three sensors per set) at the null locations using the method described above. The resonant frequencies of the three lowest resonant modes were recorded as paint was removed in increments of 0.25 mm from each side of the load region along the sensor's length (**Figure 4.5b**). The painted region spanned the entire width of the sensor for this test.

### 4.2.4. Loading Multiple Null Locations Simultaneously

An investigation was conducted to assess the possibility of using a single magnetoelastic sensor for simultaneous detection of multiple parameters. Three groups of three sensors each were painted at the 1<sup>st</sup>, 2<sup>nd</sup> and 3<sup>rd</sup> null locations. The dimensions of the paint regions were chosen based on the results of the changing width and changing length experiments (see **Section 4.3.2** and **4.3.3**). After determining the resonant frequencies with mass loading on the null location of one resonant mode, paint regions were added to null points corresponding to additional modes on each sensor. The purpose of this procedure was to determine if the sensor could be used to track loads at multiple locations simultaneously. The sensor groups initially loaded at only the null locations of the 1<sup>st</sup> resonant mode were additionally loaded at the 3<sup>rd</sup> resonant mode null points. The groups initially loaded at the 3<sup>rd</sup> resonant mode null point locations were additionally loaded at the 1<sup>st</sup>. The sensors loaded at null locations of 2<sup>nd</sup> resonant modes were additionally loaded at the null locations of the 1<sup>st</sup> resonant mode. The hypothesis is that if the sensor can independently track multiple modes, the addition load at another mode will have a minimal effect on the resonance of the initial load.

## 4.3. Results and Discussions

### 4.3.1. Confirming Null Locations

**Table 4.1** lists the expected displacements of the lowest 3 resonant modes at locations across the strip length (they are the absolute values of a cosine function, as shown **Figure 4.1**). The recorded changes in sensor response (normalized to mass), obtained by loading sensors at the respective locations, were also included in the table. For convenience, the frequency shifts were displayed after normalizing to the highest expected displacement for each group of sensors (i.e. for  $L/2$ , all locations were normalized such that the  $f_2$  value was 1).

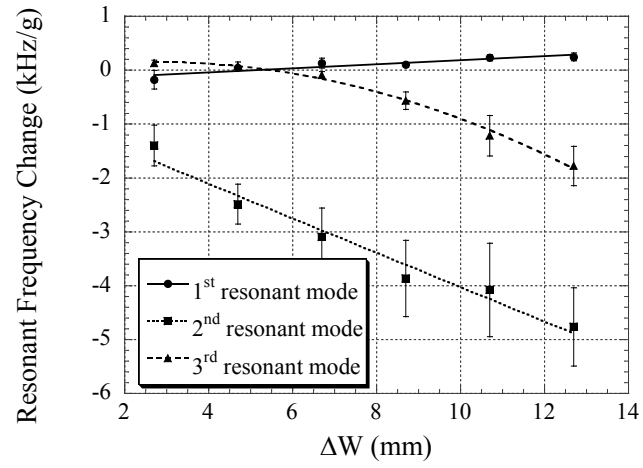
When comparing the displacements to the normalized frequency changes in **Table 4.1**, it is evident that the actual frequency response for each resonant mode follows a trend similar to the displacements at each mode, even at loads up to 25% of the mass of the sensor (sensor mass 0.114 g, paint mass 0.029 g). This indicates that each resonant mode has locations where mass loading has the highest impact on its resonant frequency, as well as locations where the mass loading has no impact on its resonant frequency. Results in **Table 4.1** shows that the sensitivity towards mass loading for each resonant mode is strongly correlated to the displacement of that mode.

**Table 4.1.** Theoretical displacements at different locations for the three lowest resonant modes. The resonant frequency shifts at these modes were also measured when the sensor was loaded at these locations. The resonant frequency values are the mean of measurements from 3 sensors.

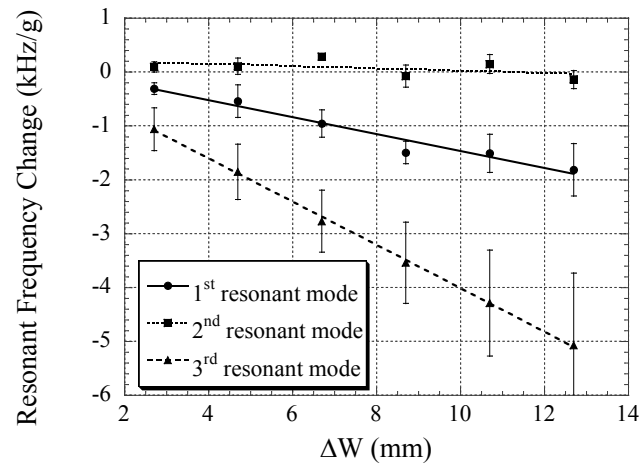
Load Position	Displacement Normalized to the Displacement at the Edge of the Sensor			Frequency Change Normalized to Mass (kHz/g)			Frequency Change Normalized to the Highest Value		
	1 <sup>st</sup>	2 <sup>nd</sup>	3 <sup>rd</sup>	$\Delta f_1$	$\Delta f_2$	$\Delta f_3$	$\Delta f_1$	$\Delta f_2$	$\Delta f_3$
L/2	0.000	1.000	0.000	0	5.2	0.6	0.000	1.00	0.122
L/3	0.500	0.500	1.000	2.2	3.7	9.5	0.234	0.387	1.000
L/4	0.707	0.000	0.707	6.2	-0.3	4.9	0.707	-0.039	0.550
L/6	0.866	0.500	0.000	4.9	1.7	0.3	0.866	0.310	0.061
0	1.000	1.000	1.000	18.2	18.1	13.1	1.000	0.995	0.721

#### 4.3.2. Changing the Sensing Region Width

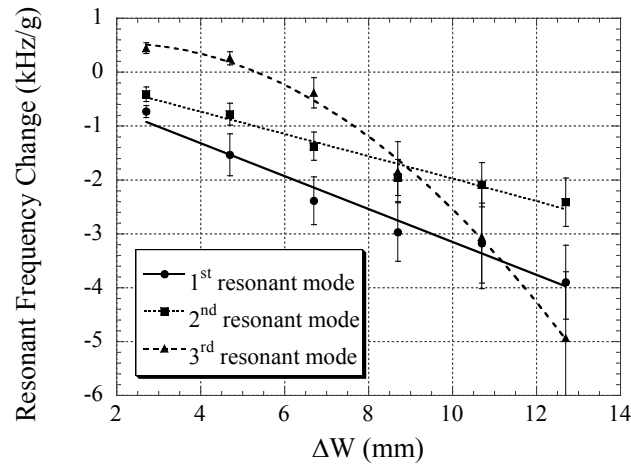
**Figure 4.6** illustrates the relationship between the width of the loading region and the resonant frequency for each null location. For loading at the null locations of 1<sup>st</sup> and 2<sup>nd</sup> resonant modes, the changes in resonant frequencies for the corresponding null locations are near zero. For example, **Figure 4.6a** shows that  $\Delta f_1$ , the 1<sup>st</sup> resonant frequency shift, has a very low degree of change regardless of sensor width. This is to be expected since there should be no vibration to damp at this location. However, the response of the 3<sup>rd</sup> resonant mode, as shown in **Figure 4.6c**, increases with increasing coverage along the width of the sensor. It is possible that this is a result of asymmetry between the sensor ends, which would act to shift the null locations along the sensor width. While this would occur at each null point, the signal of the 3<sup>rd</sup> resonant mode would be most susceptible since the level of vibration increases more rapidly than the other two modes as a function of distance from the null.



(a)



(b)



(c)

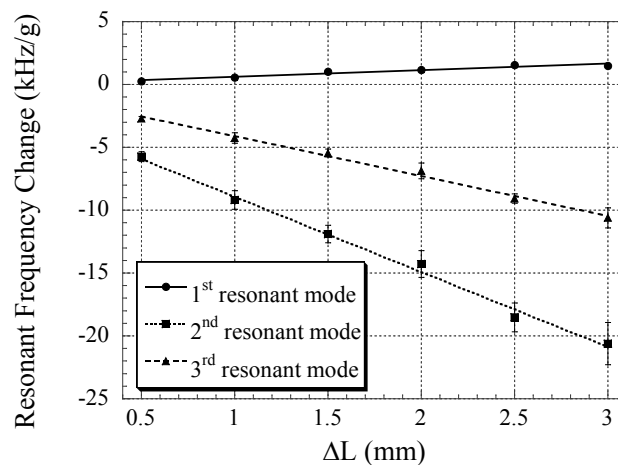
**Figure 4.6.** The frequency shifts for the three lowest resonant modes associated with varying the width of the load regions at the null locations of the (a) 1<sup>st</sup>, (b) 2<sup>nd</sup>, and (c) 3<sup>rd</sup> resonant modes. Error bars are the standard deviation of measurements of three sensors.

In addition to the shifting of the 3<sup>rd</sup> resonant frequency when a mass is applied to its null location, it is also evident from **Figure 4.6** that some of the resonant frequencies experienced a small increase after a mass was applied. Cheng and colleagues reported similar observations, which were attributed to modifications of the sensor's elasticity in the loading region that appeared to be more significant than the damping effect of the added mass [4.14].

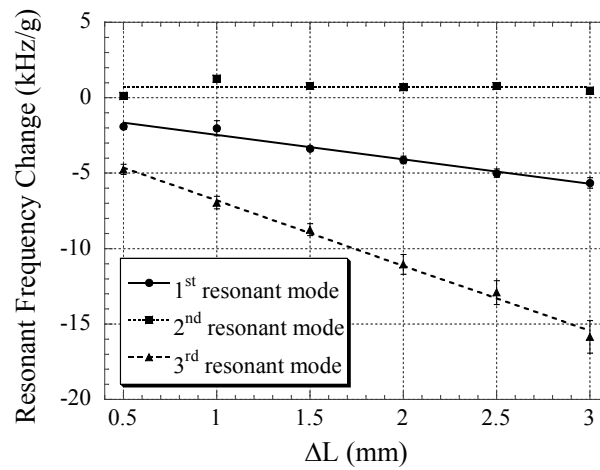
**Figure 4.6** also indicates that the frequency shift for each sensor depended on load region width. Therefore, when using the sensor to determine multiple loads by functionalizing different null locations, the sensitivity of each null location can be controlled by varying the area of coverage along the width of the sensor.

### 4.3.3. Changing the Sensing Region Length

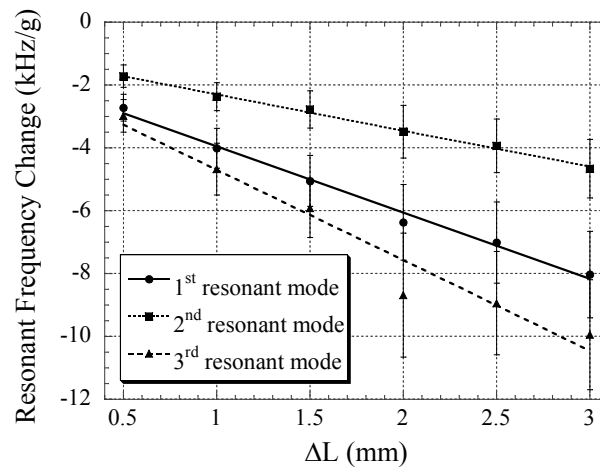
Investigations into the effect of varying the length of the sensing region yielded the results shown in **Figure 4.7**. Similar to changing the width of the sensing region, changing the length results in a modification to the sensor's sensitivity for all resonant modes. As expected, loading at the null locations of the 1<sup>st</sup> and 2<sup>nd</sup> resonant modes (**Figure 4.7a** and **Figure 4.7b**) results in a near-zero response in the frequency shift of the corresponding resonant frequencies. However, loading at the null locations of the 3<sup>rd</sup> resonant mode (**Figure 4.7c**) affected the resonant frequency of the 1<sup>st</sup> mode. Therefore, while the length of the sensing region at any given null location can be used to control the sensitivity of the sensor response, it does not have a significant effect on maintaining a zero frequency shift for the associated resonant mode at zero loading. This is in contrast to the role of the sensing area width, since a change in the width alters both the sensitivity and the frequency shift of modes when loading at their null locations. Therefore, using this technology to monitor multiple variables of interest on a single strip would entail zeroing the frequency response corresponding to each null location by modifying the sensing width and calibrating the sensitivity at each null location by setting an appropriate sensing region length.



(a)



(b)



(c)

**Figure 4.7.** The frequency shifts for the three lowest resonant modes associated with varying the length of load regions at the null locations of the (a) 1<sup>st</sup>, (b) 2<sup>nd</sup>, and (c) 3<sup>rd</sup> resonant modes. Error bars are shown corresponding to the standard deviation of measurements of all three sensors.

#### 4.3.4. Loading Multiple Regions Sequentially

Ideally, loading the null points associated with a resonant mode should cause zero frequency shifts in the resonant modes not associated with that null location. Results from **Section 4.3.2** and **4.3.3** indicated that a width of 6.7 mm provided a zero frequency shift for the 3<sup>rd</sup> mode when loading its null locations; therefore, all coatings for this test were set at 6.7 mm wide by 1 mm long. **Table 4.2** shows the results of first applying the coating at the null locations of one mode and then adding paint to null locations of another resonant mode.

**Table 4.2.** Sequential loading at null locations of multiple resonant modes. The values are the mean of measurements from 3 sensors.

Resonant Mode of the first loading	$\Delta f_1$	$\Delta f_2$	$\Delta f_3$	Resonant Mode of the second loading	$\Delta f_1$	$\Delta f_2$	$\Delta f_3$
1 <sup>st</sup>	0.010	8.375	1.006	3 <sup>rd</sup>	10.02	2.261	-0.610
2 <sup>nd</sup>	8.385	-0.389	6.218	1 <sup>st</sup>	-0.705	2.761	0.007
3 <sup>rd</sup>	11.62	4.283	0.918	1 <sup>st</sup>	-1.190	5.892	-0.009

The sensor showed minimal interference on other resonant modes when loading a particular resonant mode, as illustrated in the sequential loading at null locations of the 1<sup>st</sup> and then the 3<sup>rd</sup> resonant modes, and vice versa. The total frequency shift for these two tests is summarized in **Table 4.3**. It is evident from **Table 4.3** that the mass loading has a cumulative effect on the sensor response. **Table 4.2** shows that loading at null locations of the 1<sup>st</sup> resonant mode had a slightly different result before and after loading the null locations of the 3<sup>rd</sup> resonant mode. There are several possible reasons that this could occur. In determining the area for application of the load, the sensor must be

assumed perfectly rectangular; however, if the ends of the sensors are not perfectly parallel, then the ideal null locations would be shifted. Additionally, the authors assumed for simplicity that frequency shift was linearly proportional to mass change, and that loads applied to the sensor null locations were placed in perfect symmetry around it. While it is not likely that that location of applied paint was off-center from the ideal null locations, it is possible that the thickness or density of the painted layer varied enough to cause the small differences between the frequency shifts observed during the sequential loading experiment by causing out-of-plane vibrations.

**Table 4.3.** Comparison of sequential loading at the null locations of 1<sup>st</sup> and 3<sup>rd</sup> resonant modes in opposite order. The values are the mean of measurements from 3 sensors.

Resonant Mode of the Loading		$\Delta f_1$	$\Delta f_2$	$\Delta f_3$
1 <sup>st</sup>	3 <sup>rd</sup>	10.03	10.64	0.40
3 <sup>rd</sup>	1 <sup>st</sup>	10.44	10.17	0.91

#### 4.4. Conclusions

This work demonstrates the capacity for multiple parameter sensing with a single magnetoelastic sensor by loading at null locations of multiple resonant modes and monitoring the corresponding resonant frequencies. It was shown that the frequency shift due to a mass load at the null locations of a given resonant mode can have no impact on the corresponding resonant frequency by controlling the width of the loading region, while the overall sensitivity of the sensor could be modified by changing the length of the load region. Results showed that there was little difference between the sensor responses when loading a single resonant mode or multiple null locations simultaneously, allowing detection of multiple parameters with a single magnetoelastic resonance sensor.

## References

- 4.1. B. Pratiher, S.K. Dwivedy, "Nonlinear vibration of a magneto-elastic cantilever beam with tip mass," *J. Vib. Acoust.*, vol. 131, no. 2, 2009.
- 4.1 G.Y. Wu, "Non-linear vibration of biomaterial magneto-elastic cantilever beam with thermal loading," *Int. J. Non-Linear Mech.*, vol. 55, pp. 10-18, 2013.
- 4.2 D. Kouzoudis, C.A. Grimes, "The frequency response of magnetoelastic sensors to stress and atmospheric pressure," *Smart. Mater. Struct.*, vol. 8, pp. 885-889, 2000.
- 4.3 C.A. Grimes, D. Kouzoudis, "Remote query measurement of pressure, fluid-flow velocity, and humidity using magnetoelastic thick-film sensors," *Sens. Actuators*, vol. 84, pp. 205-212, 2000.
- 4.4 M.K. Jain, Q.Y. Cai, C.A. Grimes, "A wireless micro-sensor for simultaneous measurement of pH, temperature, and pressure," *Smart Mater. Struct.*, vol. 10, pp. 347-353, 2001.
- 4.5 C.A. Grimes, S.C. Roy, S. Rani. Q. Cai, "Theory, instrumentation and applications of magnetoelastic resonance sensors: a review," *Sensors (Basel)*, vol. 11, no. 3, pp. 2809-2844, 2011.
- 4.6 Cai Q.Y., Jain M.K. and Grimes C.A., "A wireless, remote query ammonia sensor," *Sensor. and Actuat. B-Chemical*, vol. 77, no. 3, p. 614-619, 2001.
- 4.7 X. Gao, W. Yang, P. Pang, S. Liao, Q. Cai, K. Zeng, C.A. Grimes, "A wireless magnetoelastic biosensor for rapid detection of glucose concentrations in urine samples," *Sen. Actuators B*, vol. 128, no. 1, pp. 161-167, 2007.
- 4.8 C. Ruan, Z. Kefeng, O.K. Varghese and Grimes C.A., "A magnetoelastic bioaffinity-based sensor for avidin," *Biosens. Bioelectron.*, vol. 19, no. 12, pp. 1695-1701, 2004.
- 4.9 J. Wan, M.L. Johnson, R. Guntupalli, V.A. Petrenko. B.A. Chin, "Detection of *Bacillus anthracis* spores in liquid using phage-based magnetoelastic micro-resonators," *Sen. Actuators B*, vol. 127, no. 2, pp. 559-566, 2007.

- 4.10 R.S. Lakshmanan, R. Guntupalli, J. Hu, V.A. Petrenko, J.M. Barbaree, B.A. Chin, "Detection of Salmonella typhimurium in fat free milk using a phage immobilized magnetoelastic sensor," *Sens. Actuators B*, vol. 126, no. 2, pp. 544-550, 2007.
- 4.11 C. Ruan, K. Zeng, O.K. Varghese, C.A. Grimes, "Magnetoelastic immunosensors: amplified mass immunosorbent assay for detection of Escherichia coli O157:H7," *Anal. Chem.*, vol. 75, no. 23, pp. 6494-6498, 2003.
- 4.12 B. Pereles, A. DeRouin, K.G. Ong, "Partially loaded magnetoelastic sensors with customizable sensitivities for large force measurements," *IEEE Sensors Journal*, vol. pp, no. 99, 2014.
- 4.13 S. Li, Z.Y. Cheng, "Nonuniform mass detection using magnetostrictive biosensors operating under multiple harmonic resonance modes," *J. Appl. Phys.*, vol. 107, no 11, pp. 4514, 2010.
- 4.14 R. Guntupalli, J. Hu, R.S. Lakshmanan, T.S. Huang, J.M. Barbaree, B.A. Chin, "A magnetoelastic resonance biosensor immobilized with polyclonal antibody for the detection of Salmonella typhimurium," *Biosens. Bioelectron.*, vol. 22, no. 7, pp. 1474-1479, 2007.
- 4.15 K.G. Ong, C.S. Mungle, C.A. Grimes, "Control of a magnetoelastic sensor temperature response by magnetic field tuning," *IEEE Trans. Magn.*, vol. 39, no. 5, pp. 3319-3321, 2003.

## 5. A Wireless Sensor for Real-Time Monitoring of Tensile Force on Sutured Wound Sites

Andrew DeRouin<sup>†</sup>, Nina Pacella<sup>†</sup>, Chunfeng Zhao, Kai-Nan An, Keat Ghee Ong  
Biomedical Engineering, Michigan Technological University, Houghton MI 49931, USA.

### Abstract

A new wireless sensor was designed, fabricated and applied for *in situ* monitoring of tensile force at a wound site. The sensor was comprised of a thin strip of magnetoelastic material with its two ends connected to suture threads for securing the sensor across a wound repair site. Since the sensor was remotely interrogated by applying an AC magnetic field and capturing the resulting magnetic field, it did not require direct wire connections to an external device or internal battery for long-term use. Due to its magnetoelastic property, the application of a tensile force changed the magnetic permeability of the sensor, altering the amplitude of the measured magnetic field. This work presents two sensor designs: one for high and one for low force ranges. A sensor was fabricated by directly adhering the magnetoelastic strip to the suture. This sensor showed good sensitivity at low force, but its response saturated at about 1.5 N. To monitor high tensile force, the magnetoelastic strip was attached to a metal strip for load sharing. The suture thread was attached to both ends of the metal strip so only a fraction of the applied force was directed to the sensor, allowing it to exhibit good sensitivity even at 44.5 N. The sensor was applied to two *ex vivo* models: a sutured section of porcine skin and a whitetail deer Achilles tendon. The results demonstrate the potential for *in vivo* force monitoring at a wound repair site.

This material was previously published in *IEEE Transactions on Biomedical Engineering*

## 5.1. Introduction

A surgical suture is typically a thread sewn into a wound site using a needle to hold damaged tissue together while it heals. Surgical sutures can be permanent or temporary, and made of degradable or non-degradable materials depending on the type of wound. Permanent sutures are typically used for skin wound closure, where they can be removed after wound healing. Additionally, they are used internally for applications that require strong mechanical support over a long period of time such as hernia repair, orthopedic repairs, etc. In contrast, temporary sutures, which are biodegradable, are used for smaller wounds with shorter healing times. Depending on the severity and location of the wound, the number of sutures used, and surgical techniques, some surgical sutures may experience large tensile forces that may cause them to fail or tear through the tissue [5.1-5.4]. Therefore, postoperative monitoring of tensile force on the suture is critical, not only to prevent excessive force from damaging the wound repair, but also to gain useful information for improving surgical techniques for wound repairs in general.

While feedback regarding tensile force on surgical repairs holds weight on the quality of the surgical procedure itself, perhaps more significant is the need for biofeedback regarding wound sites during post-surgical rehabilitation. The American Physical Therapy Association has laid out resources to promote evidence-based care; however, the literature reveals that physical therapists are limited in their ability to execute this care due to time, accessibility, variability among patients, and difficulty applying the evidence [5.5,5.6]. Therefore, feedback regarding the actual load state injury will aid in bridging this gap between understanding the clinical evidence and achieving its practical application. An effective approach to monitor the actual load of the injury site is to directly track the load at the suture used for the surgical repair.

Few sensors have been designed for monitoring forces at wound sites during and after surgery. For example, a stitch-force sensor and a hook-force sensor have been designed to monitor the tension of a suture prior to wound closure [5.7]. These sensor systems are designed for guiding surgeons to apply the correct tension on the suture,

which can lead to better wound closure since excessively tight sutures can lead to ischemia of tissue while loose sutures are unable to provide proper mechanical support for proper wound healing. Although highly accurate, these systems are only applicable during the operation, and thus cannot be used to monitor wound conditions, including tension on the suture, postoperatively.

This paper presents a wireless sensor system for *in situ* monitoring of tensile force at a wound repair site. As illustrated in **Figure 5.1**, the sensor is made of a thin strip of magnetoelastic material. Both ends of the sensor are connected to the suture threads so that tension on the suture will generate a tensile force that the sensor can quantify. The sensor can be applied in parallel to the wound closing suture. When the wound closing suture fails, force loading across the repair site will be transferred to the sensor. This allows detection of a suture failure by tracking the sudden increase in the force measurement.

The major advantage of the magnetoelastic sensor, compared to other types of force or stress sensors such as strain gauges, is its wireless, passive (no internal battery) nature. The magnetoelastic sensor is detected remotely by generating an AC magnetic field through a magnetic coil (excitation coil), and then monitoring its magnetization at harmonic frequencies with a secondary coil (detection coil) [5.8-5.11]. Since there is no direct contact between the sensor and the detector, the sensor can be used for *in vivo*, real-time tracking of force loading on the suture post-operatively, even when the suture is inside the body. In addition, the sensor does not require internal power to operate, which allows further miniaturization without compromising battery lifetime. The magnetoelastic sensor is able to detect tensile force due to its magnetoelastic property, which allows its magnetic permeability to change with an applied force. Since the captured sensor signal is proportional to the magnetization of the sensor, and the magnetization of the sensor is directly correlated to the magnetic permeability of the material, the application of a tensile force results in a change in the measured signal amplitude.

A custom detection system has been fabricated to interrogate the sensor. The system provides an AC magnetic field to the sensor, and monitors the sensor at a higher-order harmonic frequency (a frequency that is an integer multiple of the excitation magnetic field frequency). The separation in excitation and detection frequencies allows more amplification of the sensor signal without amplifying the excitation field, resulting in a larger signal-to-noise ratio. In this work, the 3<sup>rd</sup> order harmonic frequency was used because it has the largest signal amplitude among the harmonic frequencies without requiring a secondary biasing field.

The focus of this paper is to investigate the design and fabrication of the sensor, and to demonstrate its application. Two versions of the force sensor were fabricated and characterized: a low-force sensor with high sensitivity at a low force range of up to 1.5 N, and a high-force sensor that can sense forces up to 44.5 N. For potential monitoring of sutures in limbs, such as after a tendon repair surgery, tube-shape excitation/detection coils were also fabricated to monitor the sensor response. Two sets of coils were fabricated. The small coil, with an internal diameter of 28 mm, has stronger signal amplitudes but was only applicable for testing purposes and small animal tests due to its small size. The large coil, with an internal diameter of 88 mm, can be used for applications involving large animals or even humans, but has a weaker signal.

## 5.2. Experiments

### 5.2.1. Sensor Design and Fabrication

**Figure 5.1** shows the two sensor designs: a low-force sensor and a high-force sensor. The low-force sensor was made of a thin magnetoelastic strip of Metglas 2826MB, an amorphous ferromagnetic alloy from Metglas Inc. Both ends of the sensor were attached to the suture thread so that a tensile force on the suture can be directly transferred to the sensor, changing its magnetic response (see **Figure 5.1a**). This design allowed the sensor to measure small force loading but was unable to detect large force

values due to saturation of the sensor response. The low-force sensor was fabricated by mechanically shearing the as-purchased 30  $\mu\text{m}$ -thick Metglas ribbon into 30 mm  $\times$  1 mm strips. The ends of each strip were then adhered to commercial medical sutures (Ethicon Coated Vicryl Polyglactin 910 suture) with adhesive (JB Weld Original Cold Weld Formula). The sensor was then coated with rubber (Perfomix Plastidip) to protect it from the environment.

The high-force sensor was designed to share the load applied to the sensing component with a secondary piece of material. It consisted of the same magnetoelastic strip as the low-force sensor, but with both of its ends adhered to a metal substrate using epoxy (see **Figure 5.1b**). The thicker metal strip experienced most of the applied force, leaving only a fraction of the load for the sensor to measure. As a result, the second design had a larger range, but a lower resolution. Specifically, the high-force sensor consisted of a stainless steel strip (stainless steel 304, annealed) with hooks at both ends. The dimensions of the metal strip were 28 mm  $\times$  1 mm  $\times$  0.5 mm. The sensor, 20 mm  $\times$  1 mm  $\times$  30  $\mu\text{m}$ , was attached to the strip with adhesive (JB Weld Original Cold Weld Formula). Suture threads were tied to the both ends by the hooks. A rubber sleeve with 2.5 mm in diameter and 0.1 mm in wall thickness covered the metal strip with both opened ends sealed with rubber (Perfomix Plastidip) to completely protect the sensor from the environment.

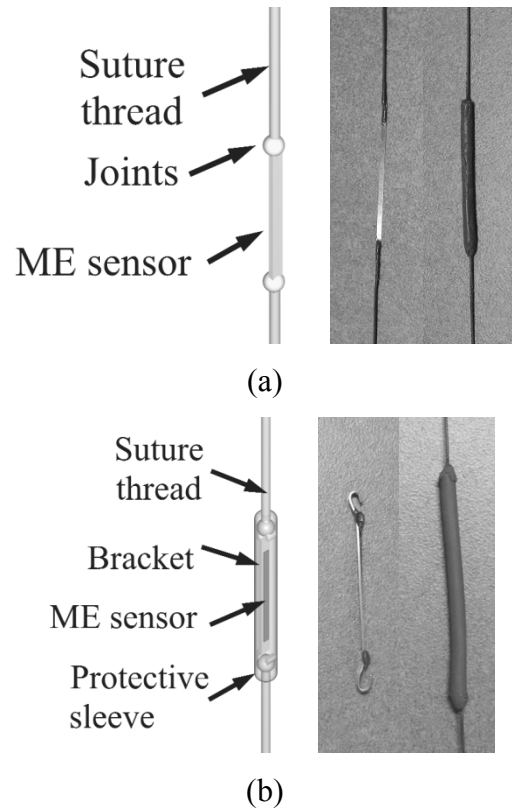
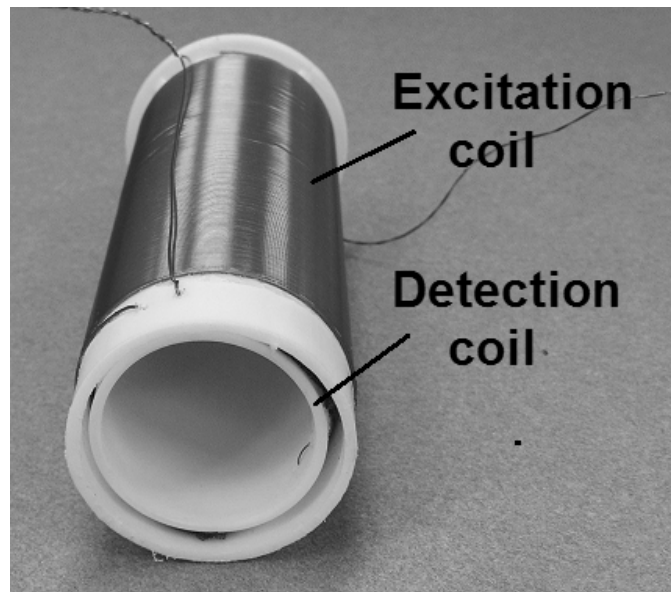


**Figure 5.1.** The (a) low-force sensor and (b) high-force sensor used for measuring the force loading on a suture. For both figures, the illustrations are on the left, the uncoated sensors are in the middle and the sensors after coating/packaging are on the right.

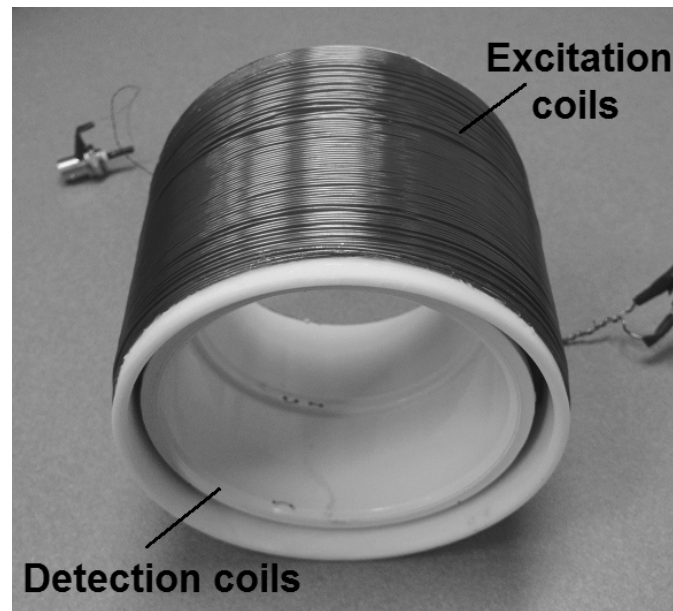
### 5.2.2. Detection System and Coils

In order to test the sensor response towards an applied tensile force, one end of the suture was secured to a support while a weight was applied at the opposite end. The sensor was placed inside the detection/excitation coils to allow data collection during this process. Two sets of coils were fabricated: a set of small coils and a set of large coils. The excitation coil of the small coil design was a solenoid with 80 mm in length, 40 mm in diameter, has 220 turns, and was made of 26 gauge magnet wire (see **Figure 5.2a**) primarily for testing and small animal experiment purposes. The small detection coil (placed inside the excitation coil) was made of two solenoids connected in series but with

opposite winding directions to cancel out the majority of the excitation signal in the absence of the sensor. Each detection coil for the small coil setup was 38 mm in length, 33 mm in diameter, has 172 turns, and was made of a 32 gauge wire. Similarly, the excitation coil of the large coil design intended for use in large animal models and applications relevant to human limbs was 80 mm in length, 115 mm in diameter, has 205 turns, and was made of a 20 gauge wire. Each large detection coil was 35 mm in length, 105 mm in diameter, had 150 turns, and was made of a 32 gauge wire (see **Figure 5.2b**). This study used solenoids as detection coils, which are practical for wrapping around the limb of the patient. For applications that require implantation of sensor in a large body area, such as at a rotator cuff, different coil designs, such as a planar coil configuration described in [5.12], could be used.



(a)



(b)

**Figure 5.2.** Pictures of the (a) small excitation/detection coil and (b) large excitation/detection coil.

The sensor was energized with a 200 Hz magnetic field using a Fluke 271 function generator and Tapco J1400 amplifier through the excitation coil. The magnetization of the sensor at 600 Hz (3<sup>rd</sup> harmonic) was tracked over a range of force loadings using an Agilent spectrum analyzer (4396B) via the detection coil (see **Figure 5.3** for illustration). A computer was connected to the spectrum analyzer to control the experiment and collect measurements for data processing.

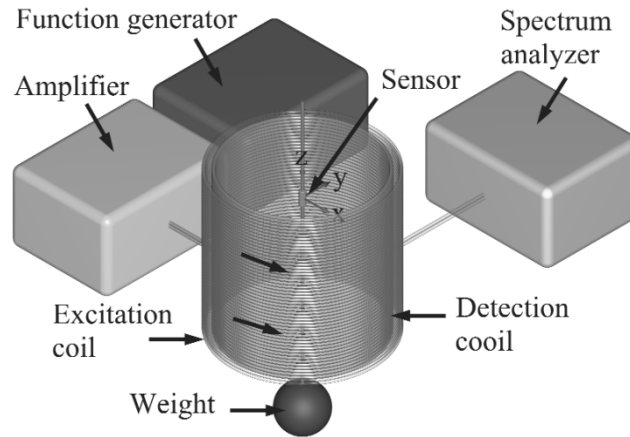


**Figure 5.3.** Illustration of the sensor detection instrument and the excitation/detection coil. The origin of the rectangular coordinate is at the center of the top detection coil.

### 5.2.3. Setup for Force Monitoring at Simulated Skin Repair

The sensor was applied to a test sample made of the skin section of a porcine shoulder, about  $12\text{ cm} \times 7\text{ cm} \times 0.8\text{ cm}$  in size. An artificial wound of about 0.4 mm in depth was created across the width at the center of the skin sample with a surgical scalpel. The wound was then closed with Ethicon Coated Vicryl Polyglactin 910 suture as shown in **Figure 5.4**. Two sets of steel plates were crimped to both ends of the skin sample. Metal wires were then tied to the metal plates, allowing the sample to be secured to the loader as well as application of weight (see **Figure 5.5**). A large-force sensor was sutured onto the sample across the wound (see **Figure 5.5**). To evaluate the force monitoring capability of the sensor, a strain gauge (Micro-measurements Type W25013) was also used. The strain gauge was attached to a stainless steel metal strip identical to the one used for the large-force sensor. Two suture threads connected the ends of the sensor to ends of the strain gauge in parallel. Each connection was then tied to a suture via a slipknot (see **Figure 5.5**). This configuration allows the sensor and strain gauge to share the load equally. The reason the sensor and strain gauge were not connected in

series was that doing so would increase the overall length of the sensor (with strain gauge), thus limiting the ability to monitor force loading around the wound site.

Currently, the sensor size (~3-4 cm in length) is not practical to be incorporated to the wound-closing suture for direct measurement of force loading across the wound. Nevertheless, the application of the sensor in parallel to the wound-closing suture can still be useful to monitor wound repair failure. If the wound repair holds, the sensor experiences only a fraction of the loaded force since a large portion of the load is supported by wound-closing suture. If the repair fails, however, the force measured by the sensor becomes much higher even under the same loading condition since the wound-closing suture no longer shares the load. Note that upon full development, the sensor will be incorporated to the wound-closing suture. This will allow monitoring of force at the wound site as well as serving as a detection system for suture failure.

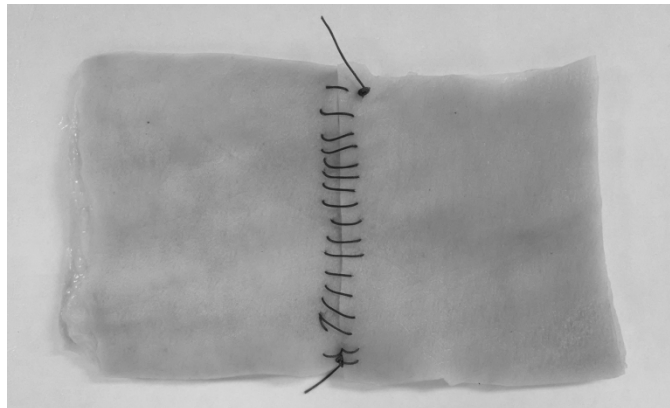


**Figure 5.4.** A rectangular shape skin sample from a porcine shoulder. A wound was created with a cut at the center along the width of the sample, and then closed with Ehicon Coated Vicryl Polyglactin 910 suture

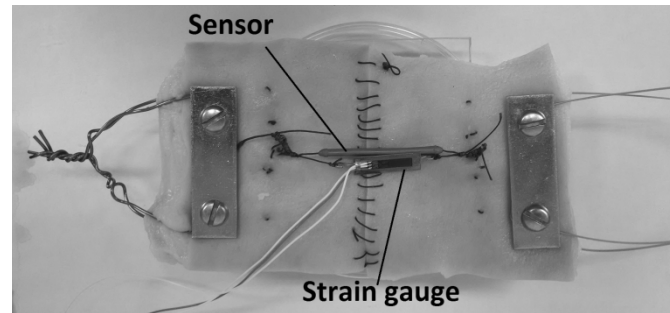


**Figure 5.5.** The strain gauge and sensor was sutured across the wound in parallel to measure applied forces at the wound site.

The change in the strain gauge resistance was measured by connecting its terminals to a Wheatstone bridge circuit and measuring the change in the output voltage of the circuit. Prior to attaching the strain gauge onto the skin sample, a calibration curve was obtained by applying a known tensile force at the strain gauge and monitoring the voltage change at the output of the bridge circuit.

To monitor the sensor, the test sample was suspended from a support at one end so that the sensor was situated directly at the center of the large detection coil (see **Figure 5.6**). Weights were then applied to the other end of the sample to generate a tensile force on the test sample. At different applied weights, the response of the sensor was measured, as well as the measurements from the strain gauge for comparison.

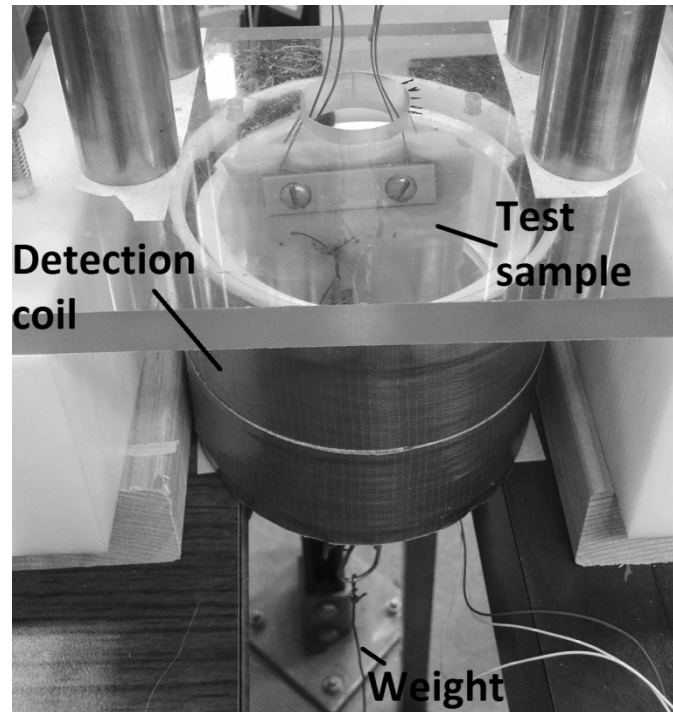


**Figure 5.6.** The setup of the wound monitoring experiment. The skin sample was supported at one end so weight can be applied at the opposite end to apply a force. The sample was at the center of the detection coil during the measurements. Note that in the practical application the coil will be placed around the patient's limb that contains the sutured tissue.

#### 5.2.4. Setup for Force Monitoring at a Simulated Tendon Repair

A large-force sensor was first calibrated by measuring its 3<sup>rd</sup> harmonic field at different tensing forces. A deer tendon (11 cm long × 0.8 cm diameter) was used to demonstrate the application of the sensor for force monitoring across tendon repairs, as shown in **Figure 5.7**. The sensor was sutured at two points along the length of the tendon with Ethicon Coated Vicryl Polyglactin 910 sutures. Additional sutures were placed at either end of the tendon test sample to allow it to be anchored to the hanging apparatus at the top and the applied weights at the bottom. The sample was soaked in phosphate-buffered saline for six hours prior to testing to ensure that it was not stiff from dehydration. The same loading setup was implemented as the porcine skin model (**Figure**

5.5) and the change in the 3<sup>rd</sup> harmonic field from the sensor was monitored as the tendon was loaded with various tensile forces.

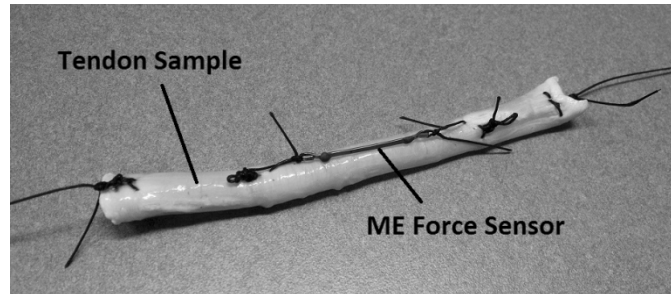


**Figure 5.7.** The application of a large force sensor to a deer tendon repair.

## 5.3. Results and Discussion

### 5.3.1. Characterization of Sensor Performance

The 3<sup>rd</sup> harmonic field amplitude measured with the small coil when a tensile force was applied to the low-force sensor can be visualized in **Figure 5.8**. The sensor showed an almost linear increase at forces below 1 N, but the slope of the response decreased significantly and saturated at about 1.5 N. Therefore, the sensor was suitable only monitoring at low forces. The full scale output of the sensor was about 0.14 mV (0.15 N - 1.5 N), or about 13% of the sensor base signal (sensor signal at its lowest loading). **Figure 5.9** plots the change in the sensor signal when it was repeatedly cycled between 0.15 N and 1.86 N. There was no observable drift.

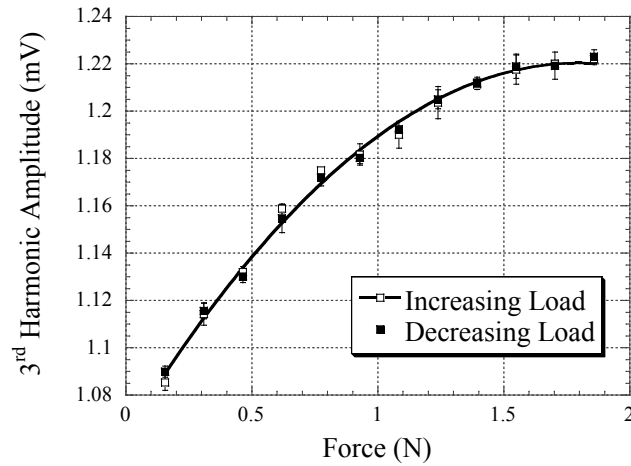


**Figure 5.8.** Change in the 3<sup>rd</sup> harmonic field amplitude, measured with the small coil, when a low-force sensor experienced a tensile force loading of up to 1.86 N. The sensor response saturated at a force loading of about 1.6 N. Error bars represent the standard deviation at each point for  $n = 3$  loading cycles.

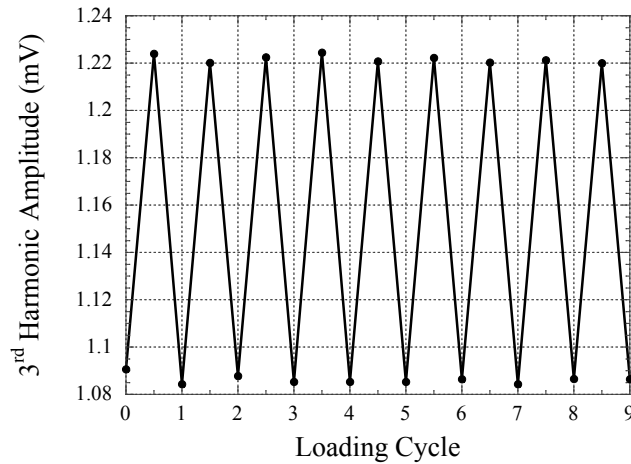


**Figure 5.9.** The response of the low-force sensor measured with the small coil when the sensor was cycled between high load (1.86 N) and low load (0.15 N) for over 9 cycles (with a cycle defined as increasing and then decreasing back to the starting load).

**Figure 5.10** plots the 3<sup>rd</sup> harmonic field amplitude of the high-force sensor when it was loaded from 5.6 N to 44.5 N, and then back to 5.6 N. The application of a tensile

force on the sensor strained the stainless steel strip, which in turn generated a force on the magnetoelastic sensor through its adhesion points. As a result, the sensor experienced a large bending force in addition to the tensile force, which caused the response to decrease rather than increase. The sensor showed a logarithmic response, where its sensitivity decreased as force increased (lines in the figure are logarithmic curves). When monitored with the small coil, the full scale output of the sensor was 0.4 mV, or about 12% of the sensor signal at maximum load. When using the large coil, the full scale output of the sensor was 0.125 mV, or about 37% of the sensor signal at maximum load. The hysteresis of the sensor signal was also determined from **Figure 5.10** as less than 3.5% of the sensor's full scale output for both coils. **Figure 5.10** indicates that monitoring the sensor with a larger coil reduced the signal amplitude by about 10 times, but the full scale output of the sensor was increased by 3 times. In addition, the large coil was a more practical size for use in large animals or even human. To examine the long term stability of the sensor, the response was also monitored when it was cycled between 5.6 N to 44.5 N (see **Figure 5.11**). The signal drift measured by the large and small coils were found to be less than 3%.

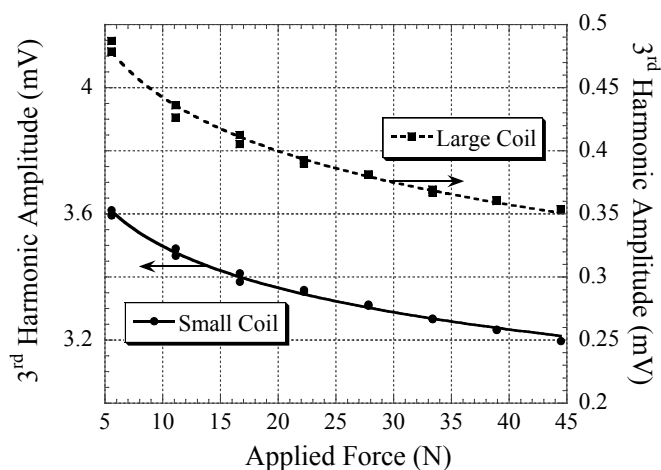


**Figure 5.10.** Change in the 3<sup>rd</sup> harmonic field amplitude when a high-force sensor experienced a tensile force loading of up to 44.5 N. The measurements using the large coil and small coil were shown.

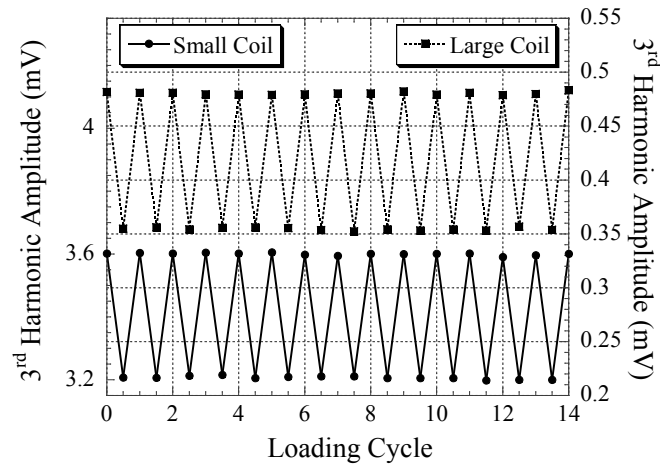
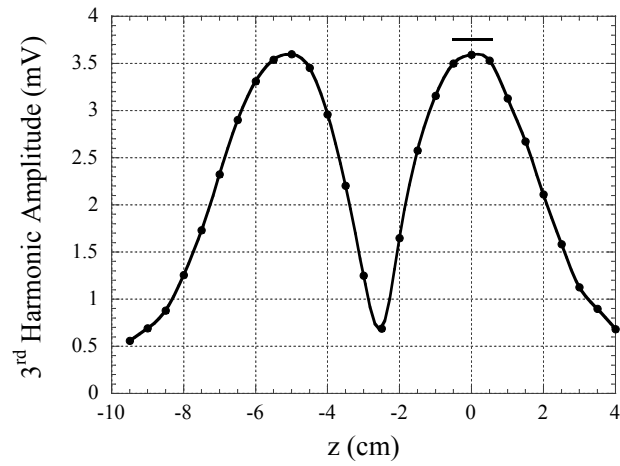
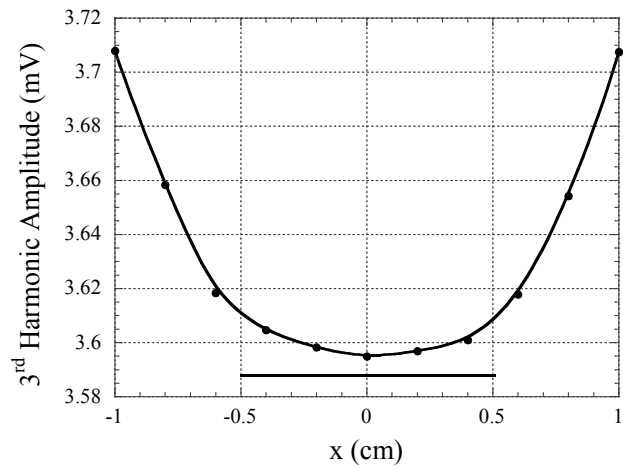


**Figure 5.11.** The response of the high-force sensor measured with the small coil and large coil when cycled between high load (44.5N) and low load (5.6 N) for over 15 cycles.

In addition to the applied load, the amplitude of the 3<sup>rd</sup> harmonic magnetic field was also dependent on the position of the sensor. **Figure 5.12** and **Figure 5.13** plot the response of a high-force sensor when its position inside the small coil and large coil, respectively, varied. When moving in the  $z$ -direction (see **Figure 5.3** for coordinate definition), the sensor signal was at its maximum when it was at the center of each detection coil (the detection coil consisted of two coils connected in series but with opposite winding directions). The sensor signal also increased when it moved away from the center of the detection coil (moved along the  $x$ - or  $y$ -axis away from the origin).



(a)



(b)

**Figure 5.12.** Change in the 3<sup>rd</sup> harmonic amplitude when the high-force sensor was moved along the (a) z-axis and (b) x-axis of the small coil (see **Figure 5.2** for coordinate definition).

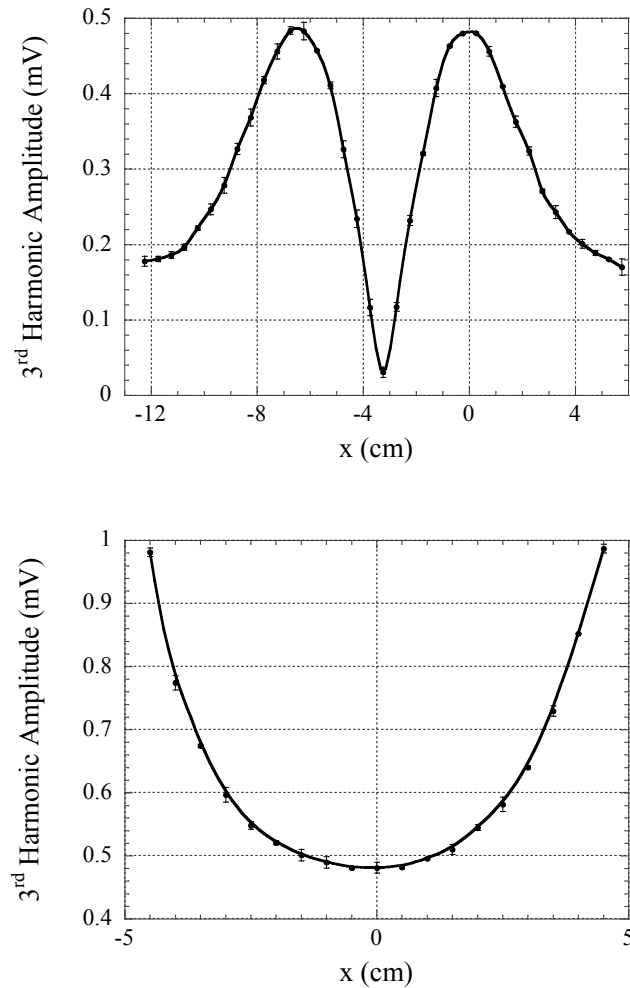


**Figure 5.13.** Change in the 3<sup>rd</sup> harmonic amplitude when the high-force sensor was moved along the (a) z-axis and (b) x-axis of the large coil (see **Figure 5.2** for coordinate definition).

For certain applications where the sensor is expected to remain static throughout its use (e.g., monitoring force loading on a tendon sample in an *ex vivo* experiment), a simple technique to ensure measurement accuracy from the changing sensor position is by confining the sensor to a region of known size, and then quantify the maximum error caused by variations in position within the region. **Figure 5.14** plots the maximum error in the sensor measurement as a function of the size of the sensor confinement region. The error is defined as a percentage error with respect to the sensor's full scale output, while

the sensor confinement region size is expressed as the diameter of a spherical region from the center of the coil.

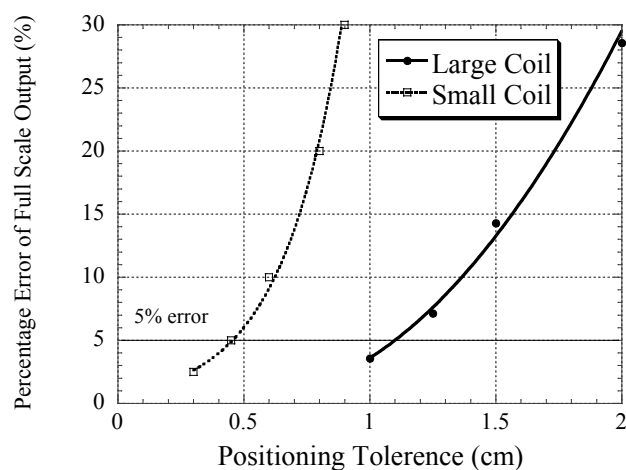


**Figure 5.14.** The error due to changing sensor position (percentage error normalized to the full scale output) as a function sensor confinement region size. The sensor confinement region size is expressed as the diameter of a spherical region from the center of the coil.

**Figure 5.14** indicates that larger detection coil allows more variations in sensor position while maintaining accuracy. In addition, this plot allows the user to determine the allowable variations in sensor position for a given error tolerance and coil size. For example, if the user wants the positioning related error to be less than 5%, the sensor should be confined to a zone of about 4.5 mm at the center of the coil (for small coil) or 11 mm (for large coil). Note that the percentage error is defined over the full scale output of the sensor. The error can be further reduced by increasing the sensitivity of the sensor, which will lead to a larger full scale output.

Although the sensor accuracy can be ensured by fixing its position, this technique is not practical for applications where the sensor is expected to migrate due to body movement. A solution to this challenge is to remove the sensor location effect, as detailed in our previous work [5.10], by measuring the 2<sup>nd</sup> harmonic field of the sensor with a biasing magnetic field, and then locating the biasing field that corresponds to the

maximum 2<sup>nd</sup> harmonic field amplitude. Since this biasing field is position dependent but is not affected by the force loading, it can be used to calibrate the force measurements from the 3<sup>rd</sup> harmonic field. However, this requires additional circuitry and a DC excitation coil, which will lead to a larger and more complicated detection system.

The failure of sensor due to excessive force loading was also investigated by continuing increasing the loading force until the sensor or suture broke. It was found that the low force sensor broke when the loading was equal or larger than 21.0 N ( $n = 5$ ,  $SD = 7.3$ ), while the large force sensor failed at about 60.7 N ( $n = 5$ ,  $SD = 2.0$ ). For the small force sensor, the failure was due to the detachment of the adhesive between the suture thread and the sensor. Thus, if needed, it is possible to improve the maximum failure load with a better adhesive. For the large force sensor, the failure was due to the breakdown of the suture thread at the knot. Therefore, a stronger suture thread or a better tying mechanism may improve the sensor reliability at large load. There was no observable bending of the sensor prior connection failure.

### 5.3.2. Force Monitoring at a Simulated Skin and Tendon Repairs

During the porcine skin repair testing, a range of forces were applied to the test sample while simultaneously measuring the output from the strain gauge and the large-force sensor signal. The actual force measured by the strain gauge was calculated by calibrating the measured output voltage to the empirically obtained strain gauge calibration curve. The actual force measured by the sensor was determined by calibrating the measured 3<sup>rd</sup> harmonic field amplitude to the empirically measured large coil curve from **Figure 5.10**. **Figure 5.15** plots the force values obtained by the sensor versus the force measurements by the strain gauge. Ideally, the curve should be linear with a slope of 1. The sensor showed a trend consistent with the strain gauge measurements, and only some differences were observed at higher force.

**Figure 5.16** illustrates the 3<sup>rd</sup> harmonic amplitudes of the sensor when the deer tendon was loaded with force ranging from 0 to 12 N. As the force increased, the 3<sup>rd</sup>

harmonic amplitude of the sensor decreased, similar to the results in **Figure 5.10**. The calibration of the sensor, obtained by measuring the sensor response while directly loading the sensor prior to suturing to the tendon sample, is also plotted in **Figure 5.16**. Ideally, the calibration curve and the tendon-loading curve should match each other. The difference between these two curves may be due to the small stretching of the tendon sample at the suture anchoring sites when tensile force was applied.

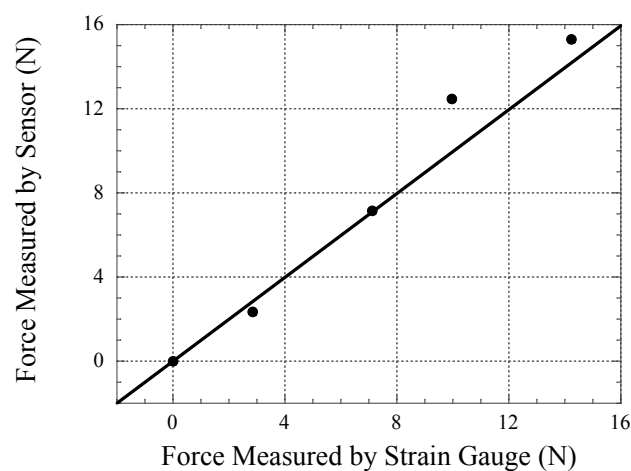


**Figure 5.15.** Force measurements by the sensor compared to the forces measured by the strain gauge when different loads were applied to the skin sample.

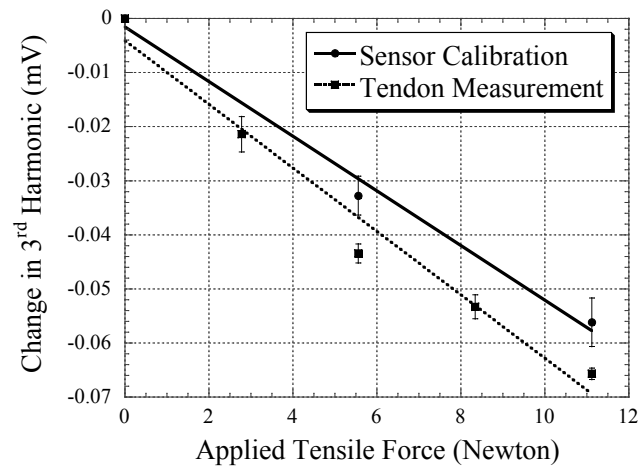


**Figure 5.16.** Force measurements by the sensor when the tendon was loaded from 0 to 12 N. The sensor calibration measurements are also shown in the plot. The errors represent standard deviation of 3 measurements.

In addition to the above tests, the large-force sensor was also embedded at the center of a  $10\text{ cm} \times 6\text{ cm} \times 6\text{ cm}$  sample of porcine muscle and monitored in the same fashion as described in the previous experiment with zero loading. In this case, no noticeable changes were observed in the sensor response compared to the externally attached sensor. Furthermore, the orientation of the sensor (with regards to rotation about the sensor length) was found to have no influence on the resulting response.

Since this tensile sensor technology can be activated and monitored through magnetic fields, it is suitable for *in vivo* force monitoring in applications such as tracking tensile force after tendon and ligament repair. By facilitating the implementation of available clinical data into current treatment regimes, the capacity to track the stress state of orthopedic injury sites has the potential to revolutionize therapy techniques, resulting in improving treatment outcomes. Currently, there is a lack of effective technologies for real-time, *in situ* tracking of internal injury sites. Standard sensors cannot directly measure stress and strain at internal muscles or tendons. Furthermore, imaging methods (magnetic resonance imaging, x-ray) cannot be deployed accurately while in motion.

Although ultrasound systems have been applied to monitor tendon strain, its implementation requires careful interface between ultrasound transducer and skin [5.13], and thus is more suitable in laboratory or clinical settings than for ambulatory applications. The ability of this sensor to directly monitor stress/strain of surgically repaired tissues such as tendons or muscles in situ and in real time can provide critical information to guide postoperative care or rehabilitation to prevent complications related to over-stressing the injury. However, although the sensor has the potential to provide ambulatory monitoring of stress/strain of injured tissue, it is only limited to patients who already needing surgical repairs.

To ensure clinical practicality, the sensor needs to be much smaller than the current size. Miniaturization of sensor is possible by altering the fabrication process. For example, shearing shorter, thinner sensors and adhering them to thinner backing materials could result in smaller sensors with the same design. Furthermore, changing fabrication technique, such as electroplating or sputtering to existing sutures allow fabrication of smaller sensors. However, smaller sensors result in lower signal amplitude, thus a more sensitive detection coil and amplifier are needed.

It is also possible to incorporate the sensing material to an existing suture so the wound-closing suture can also be used as the sensing suture. To accomplish this, a biodegradable, non-cytotoxic magnetoelastic material [5.14] can be functionalized onto the suture. Since the material is bioabsorbable and implemented in a biodegradable suture, there is no need to remove the sensor after use.

## **5.4. Conclusions**

A wireless, passive sensor was presented for monitoring tensile force on a surgical suture. Although not yet clinically ready, the current version of the sensor can be applied as a research tool to understand force loading on tendons and tissues on *ex vivo* models. Two different sensor designs show that this technology can be used for monitoring forces of different ranges. Characterization of the sensors indicates low hysteresis and drift.

Using a large coil can increase the relative full scale output of the sensor, but with a decreased in the signal amplitude. Although force measurements are sensitive to the position of the sensor, the errors are acceptable if the sensor is within 5 mm (small coil) or 10 mm (large coil) from the center of the detection coil. Thus, in practice, the detection coil needs to be secured to the user to limit its movement. For applications where a large sensor migration is expected, we also plan to implement a previously reported location calibrating technique, but will first develop the needed detection electronics and instruments. Another future work is sensor miniaturization. With a reduced size, it will be possible to incorporate the sensor into the suture used for wound closure rather than requiring an additional suture with an incorporated sensor across the wound site. Currently, the sensor was excited and monitored with standard electronic instruments. Another future step for realizing the sensor for practical use is to develop a truly wearable monitoring device.

## References

- 5.1 C.A. Cummins, G.A. Murrell, "Mode of failure for rotator cuff repair with suture anchors identified at revision surgery," *J Shoulder Elbow Surg.*, vol. 12(2), pp. 128-33, 2003.
- 5.2 F.A. Barber, P. Cawley, J.F. Prudich, "Suture anchor failure strength - an in vivo study," *Arthroscopy*, vol. 9(6), pp. 647-652, 1993.
- 5.3 C.K. Bynum, S. Lee, A. Mahar, J. Tasto, R. Pedowitz, "Failure mode of suture anchors as a function of insertion depth," *The American Journal of Sports Medicine*, vol. 33, no. 7, pp. 1030-1034, 2005.
- 5.4 D.C. Meyer, R.W. Nyffeler, S.F. Fucentese, C. Gerber, "Failure of suture material at suture anchor eyelets," *Arthroscopy*, vol. 18(9), pp. 1013-1019, 2002.

- 5.5 J. Schreiber, "A review of the literature on evidence-based practice in physical therapy," *The Internet Journal of Allied health Sciences and Practice*, vol. 3, no. 4, pp. 1-10, 2005.
- 5.6 D.U. Jette, K. Bacon, C. Batty, M. Carlson, A. Ferland, R.D. Hemingway, J.C. Hill, L. Ogilvie, D. Volk, "Evidence-based practice: beliefs, attitudes, knowledge, and behaviors of physical therapists," *Physical Therapy*, vol. 83, no. 9, pp. 786-805, 2003.
- 5.7 T. Horeman, E. Meijer, J. Harlaar, J.F. Lange, J.J. van den Dobbelen, J. Dankelman, "Force sensing in surgical sutures," *PLoS ONE*, vol. 8, issue 12, 0084466, 2013.
- 5.8 E.L. Tan, A.J. DeRouin, K.G. Ong, "Magnetoelastic-harmonic stress sensors with tunable sensitivity," *IEEE Sensors Journal*, vol. 12, no. 6, pp. 1878-1883, 2012.
- 5.9 E.L. Tan, A.J. DeRouin, B.D. Pereles, K.G. Ong, "Design, fabrication, and implementation of a wireless, passive implantable pressure sensor based on magnetic higher-order harmonic fields," *Biosensors*, vol. 1, pp. 134-152, 2011.
- 5.10 E.L. Tan, B.D. Pereles, K.G. Ong, "A wireless embedded sensor based on magnetic higher-order harmonic fields: application to liquid pressure monitoring," *IEEE Sensors Journal*, vol. 10(6), pp. 1085-1090, 2010.
- 5.11 B.D. Pereles, R. Shao, E.L. Tan, K.G. Ong, "A wireless flow sensor based on magnetic higher-order harmonic fields," *Smart Materials and Structures*, vol. 18, 095002, 2009.
- 5.12 N.P. Oess, B. Weisse, B.J. Nelson, "Magnetoelastic strain sensor for optimized assessment of bone fracture fixation," *IEEE Sensors Journal*, vol. 9, no 8, pp. 961, 2009.
- 5.13 G.A. Lichtwark, A.M. Wilson, "In vivo mechanical properties of the human Achilles tendon during one-legged hopping," *The Journal of Experimental Biology*, vol. 208, pp. 4715-4725, 2005.

- 5.14 H.R. Holmes, A. DeRouin, S. Wright, T.A. Lograsso, T.M. Riedemann, R.M. Rajachar, K.G. Ong, "Biodegradation and biocompatibility of mechanically active magnetoelastic materials," *Smart Mater. Struct.* 23 (2014) 095036 (5pp).

## 6. Force Sensing Suture Anchor for Real Time Monitoring of Tensile Loads

Andrew J. DeRouin, Alexa Thompson, Keat Ghee Ong\*

Biomedical Engineering, Michigan Technological University, Houghton, MI 49931, USA

### Abstract

A wireless sensor was embedded in a suture anchor to monitor the applied force at the suture after a surgical procedure such as a rotator cuff repair. The sensor was made of an array of magnetoelastic strips, stacked together and adhered to a stainless steel strip to form a force-sensing element. The center of the suture anchor was hollow so one end of the magnetoelastic force-sensing element could be secured to the anchor. The other end of the force-sensing element was connected to suture. As a result, after the anchor was secured to a substrate (e.g., bone), any tensile force applied to the suture would create a strain on the magnetoelastic strips, increasing their magnetic permeability. The change in the magnetoelastic strip's magnetic permeability was detected by applying a magnetic field and monitoring the resulting magnetization fields through a set of excitation/detection coils. Experiments were conducted to characterize the performance of the sensor in terms of sensitivity, stability, and detection range. The response of the sensor was also characterized with varying force-loading angles to determine the potential limitations of the sensor that could arise due to anatomical variability and surgical placement.

**Keywords:** Magnetoelastic sensors, wireless, passive, suture anchor, rotator cuff.

## 6.1. Introduction

Tendon and ligament injuries are very common, with an estimated 32 million patients and \$30 billion in costs annually in the US alone [6.1]. Surgical repair or reconstruction of a tendon or ligament is the clinical standard to treat these injuries; however, repair or reconstruction failures often occur due to high tensile force applied to the injury site, such as rotator cuff re-tear (20-90%) [6.2-6.5], flexor tendon re-rupture (10-20%) [6.6], Achilles tendon re-rupture (5%) [6.7,6.8], etc.. Monitoring tensile force after tendon repair becomes critically important, not only for guiding the postoperative rehabilitation regime, but also for preventing excessive force application to the repair site, which can cause it to fail. To address this medical limitation, a noninvasive sensor was developed for *in vivo* measurement of tensile force at these repair sites.

While the described technology can be applied to various tendon or ligament repairs, the focus of this paper is to present its application to monitor surgical repairs for rotator cuff injuries. Rotator cuff injuries are common, especially for the elderly population. They affect as much as 40% of the population at 60 years or older [6.9-6.10]. In fact, there are 300,000 rotator cuff surgeries performed every year in the United States, with a combined cost to the healthcare system of about \$3 billion annually. Rotator cuff repairs involve the placement of anchors, which are screws that anchor the tendon to the bone via a connecting suture. These repairs have a fairly high failure rate; even after treatment, reoccurrence and re-tear rates are high, with an average rate of about 25% and more than 57% for patients 65 years or older [6.9-6.11]. Therefore, there is a clear medical need for a technology, such as the sensor described in this paper, to improve the outcomes of these repairs.

Post-surgery force monitoring can lead to optimization of the surgical technique and postoperative rehabilitation regimes for rotator cuff repairs. Today, many studies [6.12,6.13] employ *in vitro* models for evaluating treatment outcomes of tendons with simulated force loading. However, without an effective quantitative method that can measure real-time, *in vivo* forces at the tendon repair site during typical daily activities of

the test subject, *in vitro* models do not provide complete information needed for better understanding the cause of repair failure, confirming the best surgical technique, and searching for an optimal rehabilitation program. In addition, constant force monitoring after the surgery can also be used to prevent failure and reduce healing times of rotator cuff surgeries. Many factors, such as age, type of injury, and health conditions, affect the healing rates of patients. Today, due to a lack of a quantitative evaluation tools to provide biofeedback during the rehabilitation process, health care providers have no choice but to use a conservative approach, unnecessarily delaying the healing process, leading to more physical therapy sessions and less than optimal healing outcomes. On the other hand, there are situations where the healthcare provider misjudges the healing progress of patients and prescribes over-aggressive treatment, further injuring the repair. The force monitoring sensor can become a tool to prevent these problems from occurring by providing quantitative feedback to the provider to allow for patient-specific care.

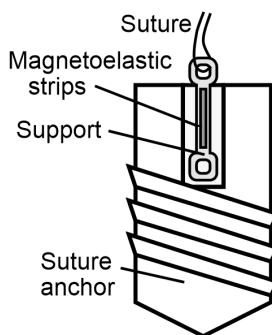


**Figure 6.1.** Suture anchor design with an embedded magnetoelastic sensor.

As illustrated in **Figure 6.1**, the proposed sensor is made of a stress-sensitive magnetoelastic material embedded in a non-metallic suture anchor used for rotator cuff repairs. One end of the sensor is attached to the anchor, while the other end is connected to a suture. As a result, when the anchor is secured to a bone, any tensile force loading on the suture will create a strain at the magnetoelastic material, increasing its magnetic permeability. The change in the magnetoelastic material's magnetic permeability is detected by applying a magnetic field and monitoring its magnetized fields through a set

of excitation/detection coils. The excitation system can be made into a wearable system, as illustrated in **Figure 6.2**, for continuous monitoring of the sensor's response. The detection and excitation coils can be encased in a solid form that conforms to the patient's shoulder to ensure consistent field generation. The detection electronics and power supplies will be attached to the coil form, and secured to the user's shoulder with a shoulder band as shown in **Figure 6.2**.

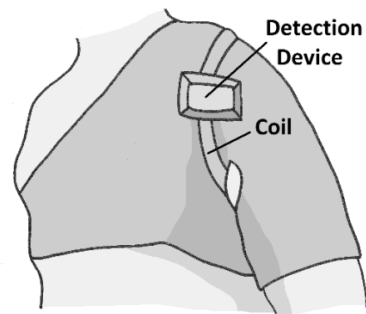


**Figure 6.2.** Illustration of the wearable detection system. A shoulder band will allow the device to be secured to the test subject, minimizing movement during use.

Prototypes of the force-sensing suture anchor were fabricated and their force sensing capability was evaluated. Specifically, the force sensitivity and repeatability of the suture anchor were quantified. The accuracy of the measurements was also determined as a function of the orientation of the applied force. To evaluate these parameters of the sensor, an experimental apparatus consisting of commercial electronic instruments was created to interrogate the suture anchor while applying various force profiles. In addition, a custom electronic circuit was fabricated to detect the suture anchor, and the performance of the custom electronic circuit was examined.

## 6.2. Experiments

### 6.2.1. Design and Fabrication of Force Sensing Suture Anchor

As shown in **Figure 6.3**, the sensor consisted of a magnetoelastic material, a suture anchor, and a support structure that connected the magnetoelastic material to the suture. The suture anchor was 3D printed with V-flash FTI 230. The design of the anchor was based on a commercial suture anchor (Smith & Nephew TwinFix Ultra PK), but the center of the anchor was hollow to allow embedding of the magnetoelastic material. The force-sensing magnetoelastic material was made of 6 strips of  $6 \text{ mm} \times 1.2 \text{ mm} \times 30 \text{ }\mu\text{m}$  Metglas 2826MB (Metglas Inc.), stacked and glued together with Loctite epoxy 1775049 to form a thicker strip with a larger signal amplitude. The magnetoelastic strips were etched by submersion in 10% ferric chloride solution for 60 seconds at  $40^\circ\text{C}$  prior to application of the epoxy to improve surface roughness, and thus, adherence. The magnetoelastic stack was adhered to a stainless steel support of  $8 \text{ mm} \times 1.2 \text{ mm} \times 0.5 \text{ mm}$ . The stainless steel piece was also etched similarly to the magnetoelastic strips, but for 180 seconds. The two ends of the stainless steel support were bent into loops so that they could be secured to the anchor at one end and tied to the suture at the other end. After adhering the magnetoelastic stack to the stainless steel support, the whole structure was inserted into the cavity of the suture anchor, which was then filled with epoxy. To ensure that the sensing structure was centered in the structure (to prevent pinning the sensor strips against the inner wall) a nylon thread was inserted through the upper loop of the stainless steel piece, allowing it to be suspended at the center of the anchor. The anchor was annealed in an oven at  $100^\circ\text{C}$  for 2 hours and left in room temperature for at least 1 day prior to use.

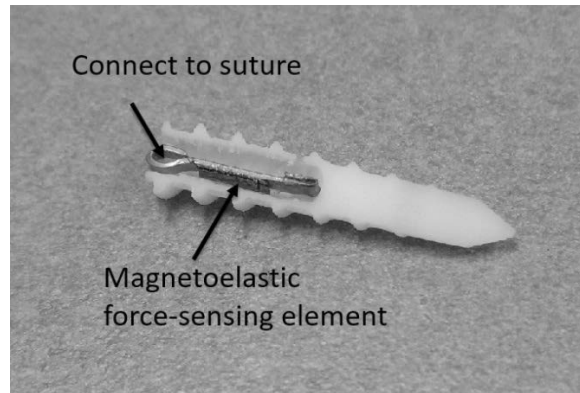


**Figure 6.3.** A photograph of a force-sensing suture anchor cut along its length prior to filling the cavity in the anchor with adhesive.

### 6.2.2. Experimental Setup and Procedures

**Figure 6.4** illustrates the experimental setup that applied tensile force of different magnitudes and directions to the suture anchor. The suture anchor was secured to a sample holder by fastening it into a threaded hole. The sample holder was inserted inside the excitation/detection coils. To apply forces of varying amplitudes, different weights were applied to the other end of the suture. The angle of the force application was varied by resting the suture thread through different stainless steel bars that were placed below the sample holder as depicted in **Figure 6.4**.

The interrogation of the suture anchor was achieved with commercial electronic devices. Specifically, a function generator (Fluke 271) was used to generate an AC voltage of 200 Hz. The AC signal was amplified with an audio amplifier (Tapco J1400), which was connected to the AC excitation coil. At the same time, a DC current was generated by a power supply (Kepco ABC 10-10DM) to the DC excitation coil. The magnetization of the magnetoelastic material inside the suture anchor was captured by the detection coil, and was measured by a spectrum analyzer (Agilent 4396B). The excitation coil was a solenoid with 80 mm length, 115 mm diameter, 205 turns, and was made of 26 gauge magnet wire. The detection coil (placed inside the excitation coil) was made of two

solenoids connected in series but with opposite winding directions to cancel out the majority of the excitation signal in the absence of the sensor. The detection coil was 35 mm in length, 105 mm in diameter, had 150 turns, and was made of 32 gauge wire.

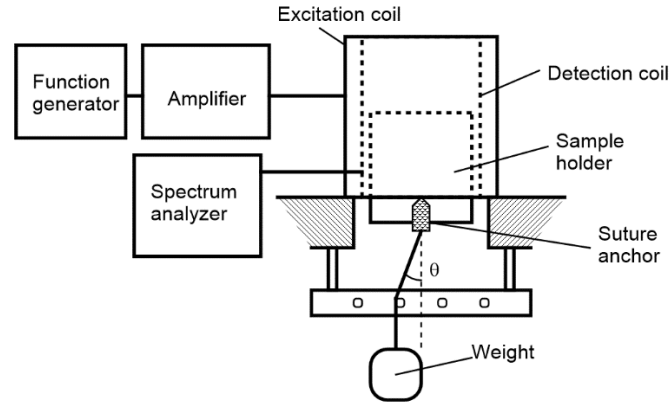


**Figure 6.4.** Depiction of the experimental setup using commercial electronic devices (function generator, amplifier, and spectrum analyzer). The suture anchor was attached to a sample holder and interrogated with excitation/detection coils. Force was applied with a weight.

To measure the sensitivity of the force-sensing suture anchor, weights of different values were applied to the anchor and the amplitude of the 3<sup>rd</sup> order harmonic (at 600 Hz) was measured with the spectrum analyzer. The amount of weight was gradually increased from 0 to 45 N, and then gradually reduced back to 0 N to determine the hysteresis of the measurements. The suture anchor was also exposed to cyclic loading between 0 and 45 N to quantify its repeatability and measurement drift. Forces above 45 N were not tested as the Ethicon Coated Vicryl Polyglactin 910 suture thread used for this experiment failed in tension at around 75 N. To determine the effect of loading direction on the suture anchor, the angle of the applied force, defined as  $\theta$  in **Figure 6.4**, was decreased from 0 to  $-45^\circ$ , and then increased to  $45^\circ$ . The excitation AC current for all experiments was 200 mA. Note from Figure 6.3 that the head of the stainless steel wire is placed close to the opening of the screw. In the actual application, the head of the stainless steel piece will be

embedded 1.5 to 2 mm into the anchor. Thus, the maximum angle of force application on the stainless steel sensing element will be approximately 45°.

### 6.2.3. Custom Detection Device

A wearable detection system is needed for practical implementation of the magnetoelastic force-sensing suture anchor. Thus, a low-cost and portable prototype detection device was designed and fabricated for monitoring the response of the magnetoelastic material (see **Figure 6.5**). The detection device operated by implementing time-domain signal acquisition followed by a Fourier Transform of the data to obtain the frequency spectrum of the sensor response. The amplitudes at each harmonic frequency were then extracted from the frequency-domain data.

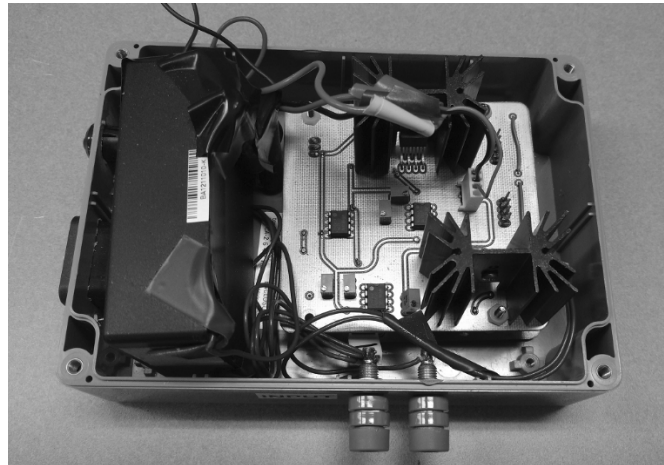


**Figure 6.5.** A photograph of the custom electronic circuit for detecting the response of the force sensing suture anchor.

#### 6.2.3.1. Excitation Circuit

A block diagram overview of the detection device is shown in **Figure 6.6**. A MATLAB graphical user interface (GUI) was generated to communicate with the MSP430f2618 microcontroller (Texas Instruments) onboard the detection circuit, which

also controlled the excitation circuit. A Wein Bridge Oscillator circuit was used to produce a 200 Hz sinusoidal signal. The Wein Bridge Oscillator output was amplified and filtered in order to smooth the signal and provide adequate voltage to the following power amplification circuit. Due to the nature of harmonic detection, it was critical that harmonics in the excitation signal were minimized to prevent detection of false harmonic signals at the detection circuit input. An OPA548 was chosen for power amplification due to its large current output per channel (5 A), wide supply range, thermal shutdown safety feature, and stability when driving inductive loads. A variable gain stage was also implemented to accommodate for different coil configurations, where higher coil impedance generally requires a higher excitation circuit output.

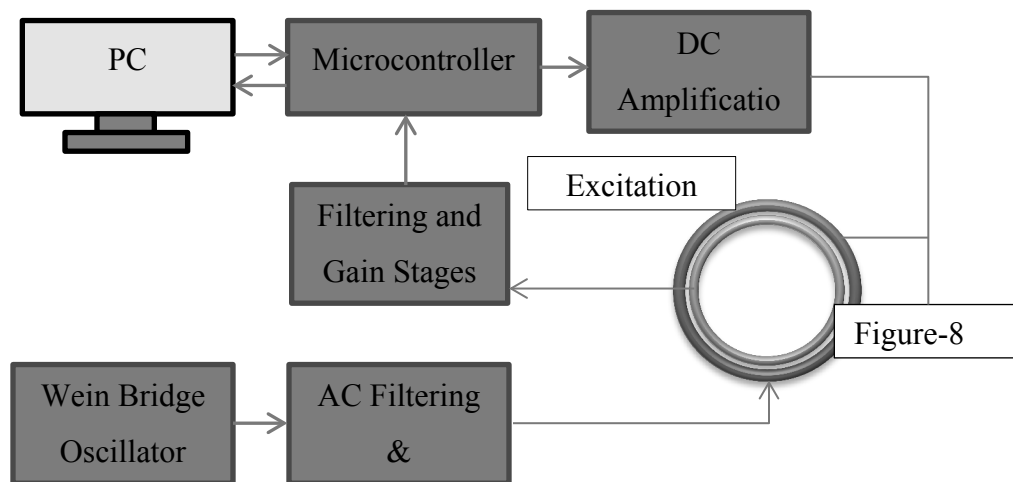


**Figure 6.6.** Flowchart depicting the functionality of the detection device.

A DC excitation circuit and coil were also included in the device design. The DC excitation field, which was connected to an independent DC excitation coil wound concentrically over the AC excitation coil, was generated by amplifying the MSP430 microcontroller's digital-to-analog converter output using LF353 general purpose op amps as well as a second OPA548 amplifier. The DC biasing field generated by this

circuit added the capability for software-controlled DC biasing sweeps to locate the maximum amplitude response corresponding to each harmonic frequency component.

### 6.2.3.2. Detection Circuit

Since the goal of the harmonic detection circuit was to monitor the response at the harmonics of the 200 Hz excitation signal, a notch-filtering stage was implemented at 60 Hz to remove power-line noise. Six additional Sallen-Key bandpass filtering stages were used to amplify and filter the detection signal using LF353 general purpose amplifiers. Ideally, the first input stage would perform the majority of the amplification; however, due to the large signal-to-noise ratio of the sensor response when compared to the excitation signal (approximately 85dBm) in addition to the low gain-bandwidth product (compared to the desired frequency range of 1 MHz) of the chosen op amps (low-cost) it was necessary to amplify the signal at future stages to prevent saturation. An overall gain of 18000 was achieved with this configuration.

The graphical user interface, as shown in **Figure 6.7**, allows control of the circuit via communication to the MSP430 microcontroller. Specifically, the user interface controls a variety of parameters including: number of 200 Hz periods to collect data over, number of points per period, the DC starting and ending current, the number of steps between those currents, and the internal MSP430 reference to use (1.5 V for smaller signals to improve resolution and 2.5 V for larger signals). A second GUI was created (**Figure 6.8**) which collects and displays a graph of the 2<sup>nd</sup> order harmonic signal (400 Hz) as a function of DC biasing field once the sweep is complete.

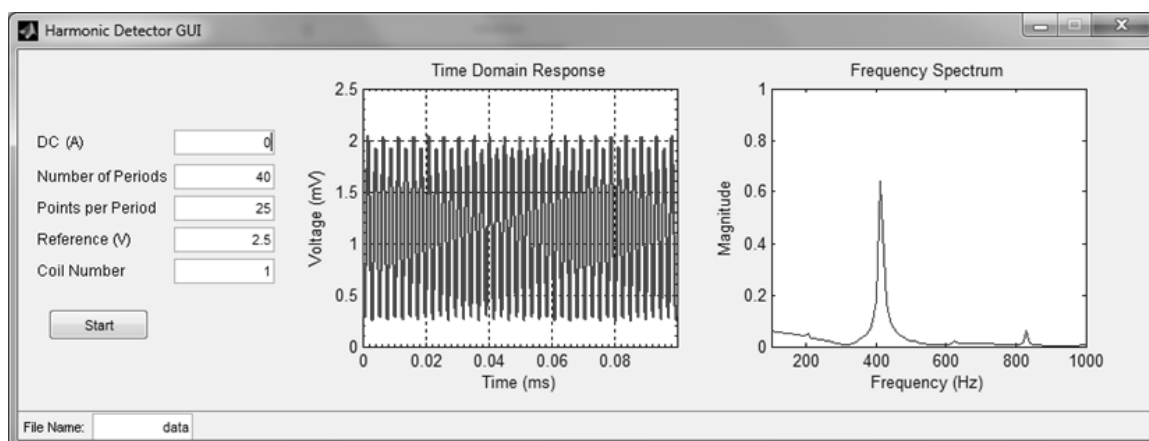


**Figure 6.7.** Graphics user interface for the custom suture anchor detection device. (top) GUI for capturing the frequency spectrum. The graph on the left shows the time-domain signal and the graph on the right are the frequency-domain data (peaks at 400 Hz and 800 Hz are the 2<sup>nd</sup> and 4<sup>th</sup> harmonics).

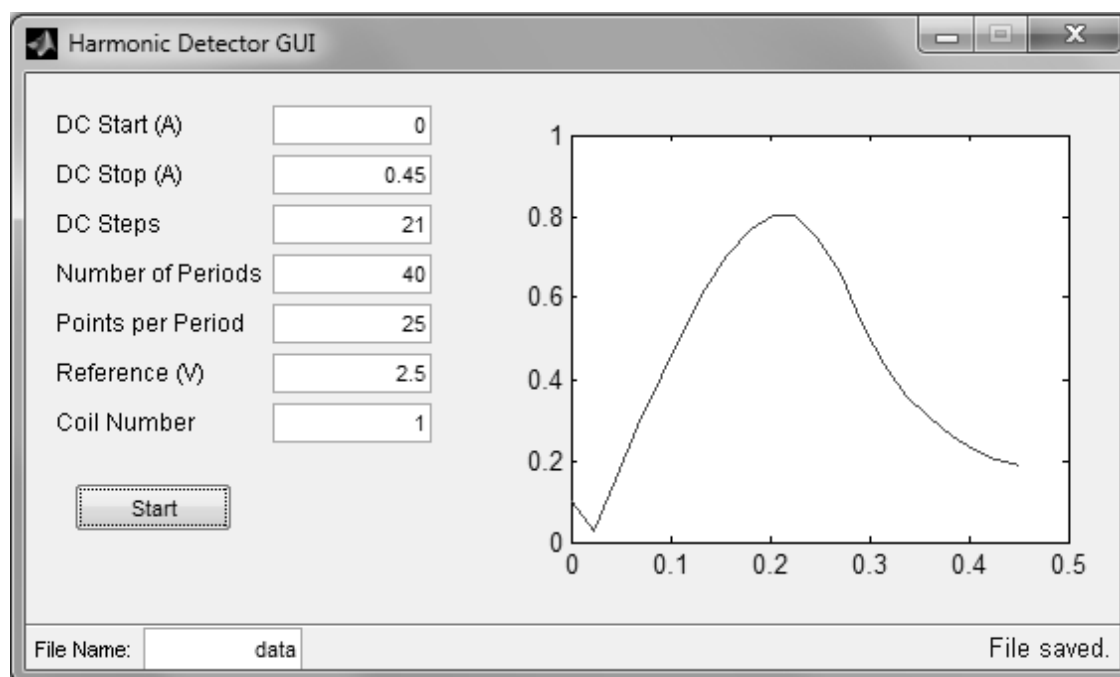


**Figure 6.8.** GUI for measuring the harmonic signals as a function of a DC biasing field. Shown in the graph is the 2<sup>nd</sup> order harmonic signals at biasing fields from 0 to 0.5 A.

### 6.3. Results and Discussions

**Figure 6.9** plots the measured 3<sup>rd</sup> harmonic response of the force-sensing suture (measured voltage at the detection coil at 600 Hz) when 0 to 45 N of tensile force was applied along the length of the suture anchor (both increasing and decreasing forces). The response followed a 2<sup>nd</sup> order polynomial, and the hysteresis between the increasing and decreasing loads was less than 1% of the sensor's full scale output. This sensor also demonstrated very low drift when exposed to cyclic loading. As shown in **Figure 6.10**, there was no observable drift in the sensor response over 10 cycles of force loading. Note that this sensing system can only measure force of up to about 50 N because it needs to detect forces of a few Newtons. The high sensitivity for this sensor system was needed to precisely measure subtle changes in forces at a rotator cuff when the user was performing various activities, allowing the study of rotator cuff strength during regeneration and also providing early indication of potential repair failure. If needed, the force range of the sensor can be changed by altering the thickness and material elasticity of the supporting substrate that the magnetoelastic material was attached to (a 1.0 mm × 0.5 mm flat 316L stainless steel wire was used for this sensor). A thicker and stiffer support for the magnetoelastic material would increase the force range but reduce the sensitivity.

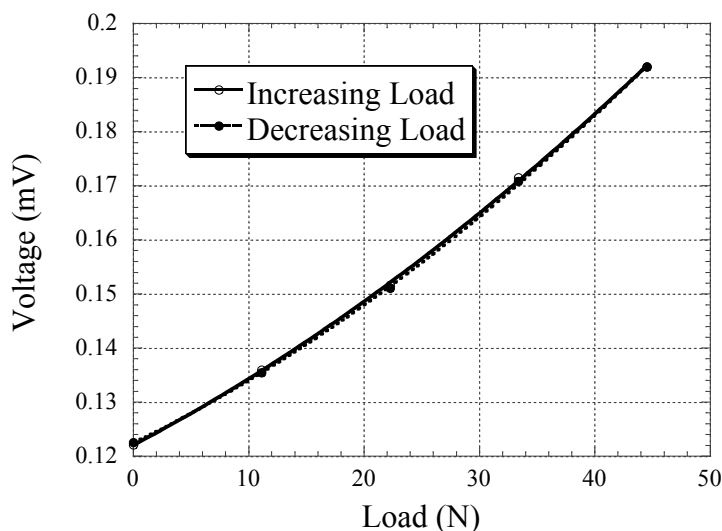


**Figure 6.9.** The response of the force-sensing suture anchor towards force applied along the longitudinal direction of the anchor. Standard deviations (less than 0.1%) are plotted but may not be visible in the plot. The hysteresis between the increasing and decreasing cycles is 0.83% of the full scale output.

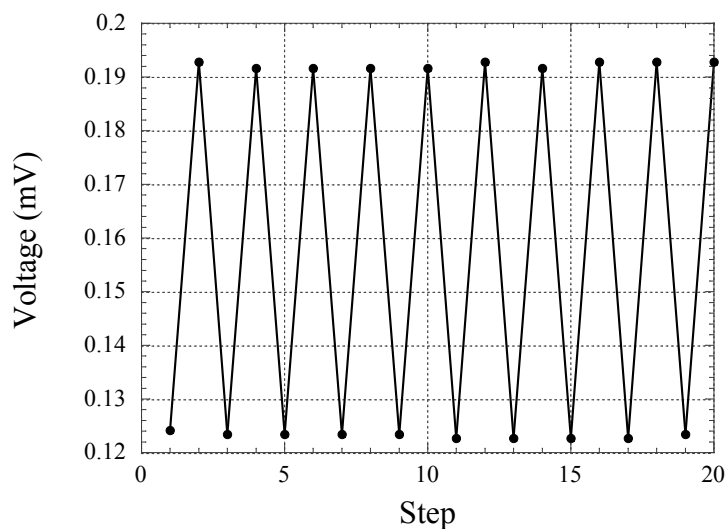


**Figure 6.10.** Change in the measured signal from the suture anchor when applied force was alternately varied between 0 and 45 N.

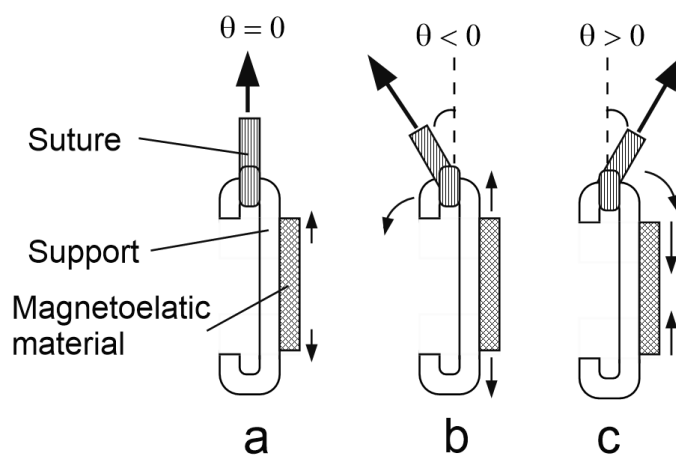


**Figure 6.11.** (a) The stainless steel was extended when the suture was pulled along the length of the suture anchor, resulting in a tensile force on the magnetoelastic material. (c) The stainless

steel support was bent away from the magnetoelastic material when the suture was pulled at  $\theta < 0^\circ$ , causing a larger tensile force at the magnetoelastic material. (c) The stainless steel support was bent towards the magnetoelastic material when the suture was pulled at an angle towards it, generating a compressive force on the magnetoelastic material.

During clinical implementation, it is unlikely that the load will be directly applied along the length of the suture anchor. Instead, the load will be applied at an angle with respect to the length of the anchor. To quantify the potential error due to the applied force direction, the sensitivity of the suture anchor was investigated as a function of the loading angle as shown in **Figure 6.11**. As shown in **Figure 6.11a**, when the force was applied along the length of the suture anchor ( $\theta = 0^\circ$ ), the stainless steel support was extended, generating a tensile force on the magnetoelastic material and thus increasing its signal amplitude (see **Figure 6.12**). When the suture was pulled at an angle away from the side where magnetoelastic material was attached (see **Figure 6.11b**) ( $\theta < 0^\circ$ ), the stainless steel support experienced bending that caused an additional tensile force on the magnetoelastic material, resulting in a larger force sensitivity (see **Figure 6.12**). However, after a certain angle, the sensitivity of the force-sensing suture did not appear to increase with angle. This was probably due to the narrowness of the adhesive-filled cavity that prevented further bending of the stainless steel support at large angles. In contrast, when a force was applied in the same direction as the magnetoelastic material (See **Figure 6.11c**), the stainless steel support bending caused a compression force on the magnetoelastic material. As a result, the force-sensing suture anchor showed a decrease to negative values (sensor signal decreased with increasing loads, as shown in **Figure 6.12**). In addition, as shown in **Figure 6.12b**, the sensor's sensitivity was very stable and also larger when loaded at an angle  $15^\circ < \theta < 45^\circ$ . Therefore, as long as the suture anchor was secured in the right direction, the sensor signal would not be affected by slight changes in the force direction, which is critical since movement of the rotator cuff may cause a slight change in the force direction and this system will be resistant to this error. Nevertheless, during the surgical implantation of the force-sensing suture anchor, the

surgeon has to make sure the suture anchor is secured in the right direction to ensure accuracy of measurements. A notch or other identifying feature can be added to the final product in order to simplify identification of the orientation during laparoscopic surgery.

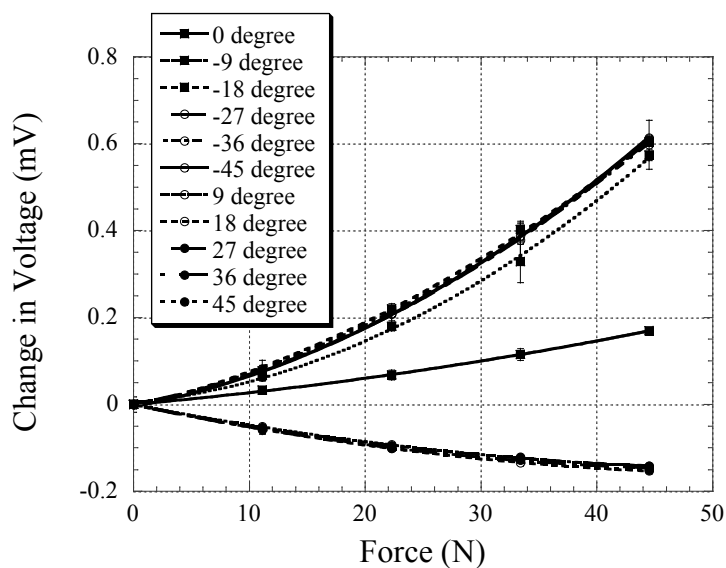


**Figure 6.12a.** Changes in sensor signal due to the angle of force loading.

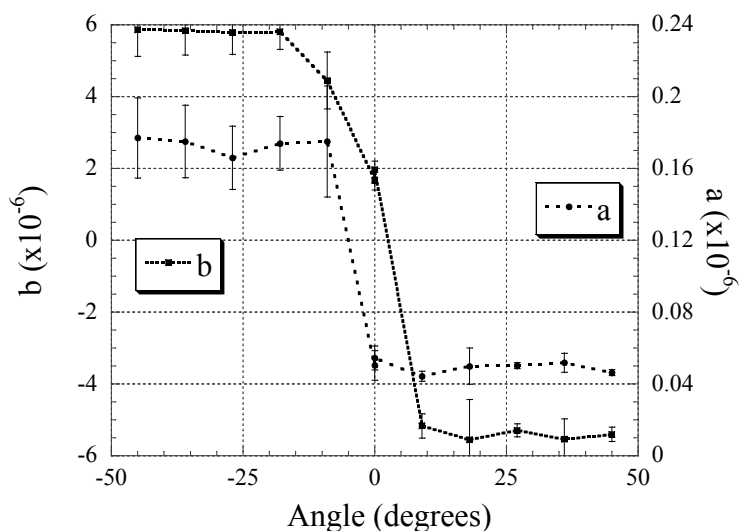


**Figure 6.12b.** Coefficients of 2<sup>nd</sup> order polynomial curves ( $y = ax^2 + bx + c$ ) fitted to the sensor response as a function of angle of the loading force (**Figure 6.12a**).

## 6.4. Conclusions

A wireless, passive sensor was integrated with a suture anchor for monitoring an force in real time, *in vivo*. Experimental results indicated the suture anchor showed repeatable response with low hysteresis and drift, and the sensitivity can be altered by changing the sensor design and material. The sensitivity of the sensor was also quantified as a function of force application direction, and it was found that the response of the suture anchor sensor was relatively constant at angles of 15° to 45° from the longitudinal axis of the anchor.

When completely developed, the described sensing system can measure loads at orthopedic repair sites, specifically rotator cuff surgeries, thus providing quantitative feedback for surgeons and physical therapists to reduce rehabilitation time and cost, as well as reducing the chances of repair failure. The suture anchor can be wirelessly monitored with a wearable device, allowing real-time, continuous biofeedback for surgeons and physical therapists to make informed decisions and accurately apply evidence-based care. To our knowledge, there is no comparable technology that can perform similar tasks efficiently, and successful implementation of our system could lead to significant cost savings in the orthopedic industry. Therefore, the sensor technology presented in this paper, when fully developed, may improve healing rates or reduce the healing time for such injuries, which will significantly reduce associated healthcare costs and increase the patient's quality of life.

## References

- 6.1. A. Praemer, S. Furner, D.P. Rice. *Musculoskeletal Condition in the United States*. Parke Ridge, IL: American Academy of Orthopaedic Surgeons: pp.182. 1999.
- 6.2. D.F. Gazielly, P. Gleyze, C. Montagnon. "Functional and anatomical results after rotator cuff repair." *Clin. Orthop. Relat. Res.*, Vol. 304, pp.43–53, 1994.

- 6.3. C. Gerber, B. Fuchs, J. Hodler, “The results of repair of massive tears of the rotator cuff.” *J. Bone Joint Surg. Am.*, Vol. 82, No. 4, pp. 505–515, 2000.
- 6.4. D.T. Harryman II, L.A. Mack, K.Y. Wang, S.E. Jackins, M.L. Richardson, F.A. Matsen III, “Repairs of the rotator cuff. Correlation of functional results with integrity of the cuff.” *J Bone Joint Surg Am* Vol. 73, No. 7, pp. 982–989, 1991.
- 6.5. L.M. Galatz, C.M. Ball, S.A. Teefey, W.D. Middleton, K. Yamaguchi, “The outcome and repair integrity of completely arthroscopically repaired large and massive rotator cuff tears.” *J. Bone Joint Surg. Am.*, Vol. 86-A No. 2 pp. 219–224, 2004.
- 6.6. D. Elliot and T. Giesen, “Treatment of unfavourable results of flexor tendon surgery: Ruptured repairs, tethered repairs and pulley incompetence,” *Indian J. Plast. Surg.*, Vol. 46, No. 3, pp. 458–471, 2013.
- 6.7. M. Dorien, M. van der Eng, T. Schepers, J.C. Goslings, N.W.L. Schep, “Rerupture Rate after Early Weightbearing in Operative Versus Conservative Treatment of Achilles Tendon Ruptures: A Meta-analysis,” *J. Foot Ankle Surg.*, Vol. 52, No. 5, pp. 622-628, 2013.
- 6.8. R. Cetti, S.E. Christensen, Ejsted, R. Jensen, “Operative versus nonoperative treatment of Achilles tendon rupture. A prospective randomized study and review of the literature,” *Am. J. Sports Med.*, Vol. 21, pp. 791-799, 1993.
- 6.9. M. Möller, T. Movin, H. Granhed, K. Lind, E. Faxén, J. Karlsson, “Acute rupture of tendon Achillis. A prospective randomised study of comparison between surgical and non-surgical treatment,” *J. Bone Joint Surg. Br.*, Vol. 83, No. 6, pp. 843-848, 2001.
- 6.10. P. Ruiz-Moneo, J. Molano-Munoz, E Prieto, J. Algorta, “Plasma rich in growth factors in arthroscopic rotator cuff repair: A randomized, double-blind, controlled clinical trial,” *Arthroscopy*, Vol. 29, pp. 2-9, 2013.

- 6.11. K.A. Derwin, S.F. Badylak, S.P. Steinmann, J.P. Iannotti, "Extracellular matrix scaffold devices for rotator cuff repair," *J. Shoulder Elbow Surg.*, Vol. 19, pp. 467-476, 2010.
- 6.12. L. Neyton, A. Godeneche, L. Nove-Josserand, Y. Carrillon, J. Clechet, M.B. Hardy, "Arthroscopic suture-bridge repair for small to medium size supraspinatus tear: Healing rate and retear, pattern". *Arthroscopy*, Vol. 29, pp. 10-17, 2013.
- 6.13. K. Kim, E. Uchiyama, H.B. Kitaoka, K.N. An, "An in vitro study of individual ankle muscle actions on the center of pressure." *Gait and Posture*, Vol. 17, pp. 125-131, 2003.
- 6.14. K. Arai, S.I. Ringleb, K.D. Zhao, L.J. Berglund, H.B. Kitaoka, K.R. Kauffman, "The effect of flatfoot deformity and tendon loading on the work of friction measured in the posterior tibial tendon," *Clinical Biomechanics*, Vol. 22, pp. 592-598, 2007.

## 7. Magnetoelastic Galfenol as a Stent Material for Wirelessly Controlled Degradation Rates

Andrew DeRouin, Roger Guillory, Weilue He, Rupak Rajachar, Jeremy Goldman, Megan Frost, and Keat Ghee Ong\*

Biomedical Engineering, Michigan Technological University, Houghton, MI 49931, USA

### Abstract

Coronary artery disease is the leading cause of death for both men and women, accounting for more than 5 million deaths in the United States alone. The gold standard of care for this condition is balloon angioplasty with implantable stents. However, long-term presence of the stent can have negative effects resulting in stenosis of implanted stents (restenosis). Current methods to prevent this problem include drug-eluting stents and biodegradable stents. Biodegradable stents proposed thus far have either degraded too slowly or failed to provide mechanical support long enough. This work investigates the use of a unique type of magnetic material for post-operative wireless control of stent degradation rates. Utilizing magnetoelastic Galfenol (iron-gallium), applied magnetic fields translate into longitudinal micron-level elongations of the material, which could be implemented to wirelessly cause a micro-stirring effect. A mass-loss experiment in cell media and corresponding cross-sectional surface area analysis revealed that degradation rates can be controlled using magnetoelastic fields. *In vitro* indirect cytotoxicity tests on primary aortic smooth muscle cells from Sprague-Dawley rats indicated that Galfenol byproduct must be concentrated to about 7 times the potency of levels collected after 60 days of degradation to cause significant cell death (~15%). Surface and cross-sectional characterization using scanning electron microscope identified differences in the corrosion behavior and surface oxide constituents. Results indicate that Galfenol ( $\text{Fe}_{80}\text{Ga}_{20}$ ) degradation rates (~ 0.55% per month) are insufficient for stenting

This material will be submitted to *IEEE Transactions on Biomedical Engineering* for publication

applications and that pitting is the primary corrosion type. While this material may not be ideal for comprising the entire stent, there is potential for use in combination with other materials. Furthermore, the ability to control degradation rates post-implantation opens new possibilities for biodegradable stents; additional magnetoelastic materials should be investigated for use in stenting applications.

## **7.1. Introduction**

More than 5 million people in the United States suffer from coronary artery disease (CAD), which is the leading cause of death for both men and women [7.1]. CAD is caused by plaque buildup in the coronary arteries that results in the reduction of the vessel diameter and, as a result, decreases the volume of oxygenated blood flowing to the heart. If left untreated, blockage of coronary arteries can lead to myocardial infarction and death [7.1]. The most common treatment for this disease utilizes coronary stents - small expandable tubes made of wire-mesh [7.2] - that are permanently implanted inside the artery to keep occluded blood vessels open [7.1]. Unfortunately, the long-term presence of a stent can cause complications such as restenosis or constrictive remodeling (narrowing) of the artery [7.2]. To avoid these issues, drug-eluting stents, such as the TAXUS and CYPHER stents [7.1], have been developed; however, even though the occurrence of restenosis and constrictive remodeling can be reduced in about 65% of cases, research shows that the continued presence of the stent becomes unnecessary after initial vessel remodeling, and may actually cause harm as it may lead to late stent thrombosis [7.3]. As a result, many researchers are working on biodegradable stents that will slowly dissolve after preliminary deployment, avoiding issues of restenosis while still treating CAD. Current work mostly focuses on iron, magnesium or polymer stents [7.3]; however, the performance of these stents has not yet reached desired expectations. For example, the degradation of magnesium stents is too fast, iron stents not only degrade too quickly but also in a non-uniform fashion, and while polymer stents can easily be tuned, they do not have sufficient mechanical strength over the course of their lifespan

[7.3]. More importantly, these stents have predetermined degradation rates that cannot be altered post-implantation. Therefore, they cannot adapt for individual conditions that may require faster or slower degradation of stents.

To develop a stenting system that is adaptive to individual conditions, this work has investigated a unique material with controllable degradation rates post-implantation, as well as the ability to monitor its surrounding conditions. The technology utilized in this project was made of a biocompatible magnetoelastic material, Galfenol ( $\text{Fe}_{80}\text{Ga}_{20}$ ) alloy, which can be set to generate a sub-micron level vibration with an AC magnetic excitation field. Preliminary results have indicated that the sub-micron vibration alters the degradation rate of a magnetoelastic material [7.4]. In addition, the vibration produces a stress-dependent magnetic flux that can be remotely monitored with a coil antenna. As a result, not only can this stent monitor the surrounding conditions of the implant site, but its degradation rate can be controlled post-implantation. Essentially, this technology will allow determination of the time point when the stent is no longer needed, at which point the rate of stent degradation can be adjusted depending on the need. This will allow for personalization of patient treatment post-stenting procedure, hence improving the outcome of percutaneous coronary interventions.

Previous studies using pure iron stents showed excellent biocompatibility in rabbit and pig animal models [7.5-7.7]. Additionally, iron has high ductility [7.8] and strength, making it ideal for stent applications. Unfortunately, iron has been shown to have a low degradation rate in arterial applications that significantly detracts from its usefulness in biodegradable stent applications [7.5]. In addition, the primary type of degradation for pure iron is pitting. As a result, many studies have been performed to find ideal microstructural modifications, treatments, or alloying methods to improve iron's degradation rate without significantly hindering its mechanical qualities and biocompatibility [7.8-7.21].

Radioactive gallium is currently used in the process of performing gallium scans (Gallium 67 Scans) to identify inflammation and areas of rapid cell division to locate

tumors and the cause of fevers with unknown causes [7.22]. No notable biological reactions have been reported aside from rare cases of allergic reaction. In fact, gallium salts are being investigated for use in treatment of some gram-positive antibiotic-resistant bacterial infections [7.23].

Galfenol has been heavily investigated for its giant magnetostrictive properties, which allow it to change in dimension with an applied magnetic field. In fact, aside from Terfenol-D, it has the highest magnetostriction of any stable material. Polycrystalline Galfenol can exhibit tensile strength in the range of 400 GPa, which is 4-5 times higher than pure iron [7.24]. Given the biocompatibility of iron and gallium on their own, Galfenol is a very interesting material for use in biomedical applications. Its increased tensile strength adds additional advantages, since stent struts composed of it could be made thinner while still providing sufficient mechanical support.

Holmes and colleagues recently investigated the cytotoxicity of  $\text{Fe}_{88}\text{Ga}_{12}$  and  $\text{Fe}_{71}\text{Ga}_{29}$  degradation byproducts generated from samples obtained from Ames Lab on L929 fibroblasts [7.4]. Results from this study showed no significant cell death at a variety of concentrations used for indirect cytotoxicity experiments. This study also included a comparison of degradation rates for Galfenol samples submersed in standard culture media with and without magnetic field application. Mass loss analysis of the samples indicated that it was possible to control degradation rates of the samples by controlling exposure to an externally applied magnetic field.

The purpose of this work is to further the investigation into the use of Galfenol as a biodegradable biomaterial – specifically toward coronary stenting applications. Therefore, similar investigations to the work by Holmes were performed on primary aortic smooth muscle cells isolated from Sprague-Dawley rats to achieve an experiment closer to *in vivo* cellular conditions. Primary cells will provide a closer representation of the true vulnerability of vascular cells to Galfenol than the immortalized fibroblast cells used in previous studies. One of the primary goals of the work presented here is to determine the threshold level of Galfenol degradation byproduct required to cause

significant cellular toxicity. The degradation behavior of the material is also analyzed in this work through mass-loss measurements, surface SEM images, and cross-sectional SEM images.

## 7.2. Experiments

Iron-Gallium (Galfenol) samples were grown using the Bridgeman Technique as reported in [7.25]. Specifically, 0.8 mm diameter Fe<sub>80</sub>Ga<sub>20</sub> wire was obtained from Ames Lab. In all cases, the wire samples were cleaned ultrasonically in 90% ethanol solution for 10 minutes and annealed for 1 hour at 100°C prior to the experiments. The wires were then sterilized for 12 hours with N74 Anprolene ethylene oxide (Anderson Sterilizers) prior to implementation *in vitro*.

### 7.2.1. Degradation Experiment

Wire samples of 3 cm length and 0.5 mm diameter were immersed in 4 mL samples and incubated at 37°C and 5% CO<sub>2</sub> for 3, 15, 30, 45, and 60 day time intervals. One group of samples ( $n = 3$  each) was exposed to magnetic field at 40 Hz and 0.5 A produced by a Fluke 271 function generator amplified by an audio amplifier (Tapco Juice 1400) through an excitation coil (11 cm length, 5 cm diameter, 540 turns). The field was applied for 2 hours each day. An Etek 10709 digital multimeter with a calibrated thermocouple was used to assess the temperature of the wires under applied magnetic field. The thermocouple was attached to a 3 cm section of Galfenol wire and placed at the center of the excitation coil with the other samples. The temperature was monitored twice per hour during the magnetic field application each day (at 30 minutes and 90 minutes into the treatment) which allowed confirmation that the temperature of the sensor never reached 38°C or above. An identical procedure was for a control group where wires were degraded in media but magnetic vibration was not applied. Each sample was weighed using an AB265-S Mettler Toledo scale prior to immersion in cell media. After the

designated timepoints, the wires were removed from solution, ultrasonicated in ethanol for 3 minutes, dried using compressed air, and weighed again to determine mass loss.

### 7.2.2. Surface Characterization

Wires from the experiment described in **Section 7.2.1** were analyzed under a JEOL JSM-6400 (Peabody, MA) scanning electron microscope equipped with a dSpec automation system (Geller MicroAnalytical Laboratory; Topsfield, MA). Wires and wire cross-sections were carbon coated and imaged at an accelerating voltage of 20kV and a current of 0.51nA. Sections were observed and imaged at a working distance of 39mm using backscattered electron imaging (BEI) at 130X normal magnification. Three regions of interest for one representative cross-section for each group were selected. Energy-dispersive x-ray spectroscopy (EDS) was performed at 300,000X normal magnification. Identified elements were normalized with provided appropriate elemental standards using identical beam conditions.

A custom sample cross-sectioning apparatus and procedure were developed to obtain the wire cross-sections. The wires obtained as described in **Section 7.2.1** were embedded into Pace Technologies ULTRA-3000R Resin by first securing one end into a cork encircled by PVC tubing which was filled with the resin. The tubing was then cut and removed from the cylindrical mold and the cylindrical samples were cut along the radial direction of the samples.

The sample cutter was constructed by first attaching the head of a commercial drill press apparatus to a Dremel. The head of the apparatus was bolted to a piece of 2" × 8" pressure-treated pine wood. ¼" holes were drilled in the wood piece and ¼" steel rods were inserted through the holes. The rods were also inserted into identical holes drilled into a ½" thick PVC sheet that acted as a base. This allowed the Dremel to move along the vertical direction in a repeatable manner. A small platform was also created and connected to the base piece. The platform was made of 2" × 4" pressure treated pine and had a 1/8" × 1/8" × 2" polycarbonate strip adhered to it using double-sided industrial

strength adhesive tape. The end of the sample was placed at the edge of the polycarbonate strip and the Dremel was lowered with a 1/16" tungsten carbide blade to cut the sample in a guillotine style. This process was repeated until 10-16 cross-sections were obtained from each sample. The circular cross-sectioned samples were then super-glued to the bottom of a cylindrical mold in the shape of the scanning electron microscope sample holder. After the super-glue was allowed to dry, more resin was applied a second time to fill the mold. The resulting sample pucks with cross sections embedded in the bottom were sanded using 120, 500, and 1200 grit MD diamond sanding discs on a Struers Tegrapol-21 automated polishing apparatus at 10 N contact force for 3 minutes each. Following sanding, the samples were polished using a nylon polishing disc with 1  $\mu\text{m}$  diamond paste for 3 minutes at 10 N. 0.1  $\mu\text{m}$  diamond paste polishing on the same type of substrate was then performed for 30 minutes at 15 N to finalize the polishing procedure.

### **7.2.3. Indirect Cytotoxicity Test**

Primary rat smooth muscle cells (SMCs) were obtained and cultured according to Chamley-Campbell et al. [7.26] with slight modifications. In brief, anaesthetized rats (Sprague-Dawley) were euthanized according to the American Veterinary Medical Association Guidelines. Rat aortas were collected and soaked in 1% pen-strep phosphate-buffered saline (PBS). The following steps were performed in a biosafety hood to avoid contamination. The adventitia layer was removed carefully from the vessel. The lumen was fluxed with 1% Penicillin-Streptomycin (pen-strep) PBS several times to remove residual blood cells. The tissue was then cut into 1-2  $\text{mm}^2$  pieces. After another PBS wash, the small tissue explants were mixed with excessive complete Dulbecco's Modified Eagle Medium (DMEM) media (with 10% fetal bovine serum (FBS) and 1% pen-strep), transferred into a tissue culture treated T75 flask, and placed into a 37  $^{\circ}\text{C}$  5%  $\text{CO}_2$  incubator. The tissue explants were left for 2-4 weeks without any movement in the incubator to let the SMCs migrate out from the tissue explant to the flask substrate. At that time, the culture flask was gently transferred out for phase contrast microscopy

examination. Once SMCs formed island-like cell sheets, 0.05% trypsin was applied to detach SMCs. After neutralization and centrifuge ( $\times 150g$  for 5 min), the dispersed cells were re-suspended in the complete DMEM media and subcultured in another T75 flask. 2-3 weeks after the first passage, cells were ready for the experiment. Along with each experiment, SMCs were characterized by fluorescently labeling anti-smooth muscle  $\alpha$ -actin [7.27]. Passages 2-5 were then used in this study.

Cultured cells were washed in 1% pen-strep PBS followed by detaching the cells using 0.05% trypsin. The cells were then seeded at a density of  $1 \times 10^4$  cells  $\text{cm}^{-2}$  with DMEM (10% FBS and 1% pen-strep). 24 hours later, the media was exchanged with media collected from the degradation experiment explained in **Section 7.2.1**. The degradation media was then spun down in a centrifuge at 5000 rpm for 10 minutes. 90% of the supernatant was removed to concentrate the degradation byproduct. The degradation media was diluted with fresh media in order to obtain the desired concentrations of 10  $\mu\text{g/mL}$ , 25  $\mu\text{g/mL}$ , 50  $\mu\text{g/mL}$ , and 100  $\mu\text{g/mL}$ . These concentrations were chosen based on work by [7.27] which showed significant primary vascular smooth muscle cell toxicity with pure iron degradation products at 50  $\mu\text{g/mL}$ . Therefore, the purpose of this experiment was to compare pure iron and Galfenol cytotoxicity. Calcein-AM (2  $\mu\text{M}$ ) and ethidium bromide (5  $\mu\text{g/mL}$ ) were used to stain the cells. An Olympus BX51 microscope was used to image cells at 4x magnification. Live-dead analysis was carried out with viability reported as the ratio of live cells to total cells in each dish. The cell densities were also compared to determine if Galfenol byproducts causes anti-proliferative effects on smooth muscle cells similar to ferric iron [28].

## **7.3. Results and Discussion**

### **7.3.1. Degradation Experiment**

The mass loss of the sensors over time is shown in **Figure 7.1**. From this graph, it is clear that this experiment confirmed the results of mass loss experiments in [7.4].

Compared to previous work, new protocols were implemented to reduce procedural errors and better reflect the structure of stents. For example, the surface-to-volume ratio of the samples used in previous work was  $1.5 \text{ mm}^{-1}$  compared to the wire surface-to-volume ratio in this experiment which was approximately  $5.1 \text{ mm}^{-1}$ . Additionally, in [7.4] the wire samples were removed from media every time they were weighed. However; in this experiment, each sample was left in cell media until it was weighed at the end of its test period. It is logical to assume that the reduction in standard deviation for this test compared to those in work by Holmes et al. resulted from eliminating variables associated with removing the sensors from the media and weighing them repeatedly. It should also be noted that, in this experiment, the average Galfenol starting mass was 313.70 mg. Therefore, the maximum change in mass is approximately 0.86% for the control and 1.20% for the samples vibrated by magnetic field. Previous experiments showed degradation from about 0.20% to 0.38%; however, the surface area-to-volume ratio is about 3.4 times higher in this experiment. If the previous experimental results were increased by this ratio and extrapolated to 60 days, they would be 2.04% and 3.87%, which would be much higher than the results obtained in this experiment. Exposure to air and breaking off regions of the degradation product during handling of samples (during the process of periodically weighing them) in previous work are possible reasons for this difference. This effect could be more significant in areas where cracking of the bulk material had occurred due to magnetoelastic vibration, accounting for the larger difference in ratio of degradation between control and vibrated samples for the experiment from previous work.

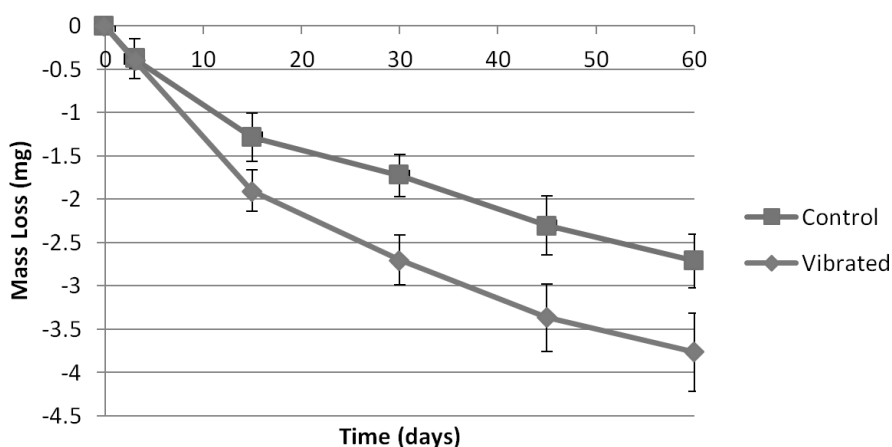


**Figure 7.1.** Mass loss of Galfenol samples in media over 15-day time points comparing control samples to remotely vibrated samples.

### 7.3.2. Surface and Cross-Sectional Characterization

Surface SEM images were taken from degraded wires at each time point. Of particular note are the images displayed in **Figure 7.2** which were taken as representative samples from the 60-day time points. Qualitatively, the control samples at right have more open and thoroughly degraded pits. Given that the magnetic field application has the effect of straining the magnetoelastic portions of the Galfenol wire, and that the oxide layer does not possess magnetoelastic properties, it is possible that the base magnetoelastic layer is applying a force to the rigid oxide formed at the interfacing surface. The shear force generated by this difference in strains is likely responsible for causing flakes of degradation byproduct to crack and break off more readily. This would explain the increased degradation rate for samples exposed to magnetic fields in addition to the likelihood that the micro-stirring effect of the wire vibration is exposing more solvent to the material surface. If this theory is correct and the change in degradation behavior is a result of exposing layers beneath the oxide layer, future studies will need to focus on the size of the dislodged oxide particles to determine if they are smaller, larger,

or the same size as standard oxide flakes in order to prevent serious side effects including potential embolisms that could result in stroke.

Because the pits in the magnetically vibrated samples appear to be more open, it is likely that pitting surface area was increased by this mechanism of breaking off oxide layers more quickly, preventing deep and narrow pits that could cause sudden strut failure, and instead accelerating the degradation of more open pits. Additionally, the sub-micron elongation and contraction of the wire along its length may have contributed to a micro-stirring effect, which could accelerate ion dissociation into and from media (or blood/tissue) more readily *in vivo*.

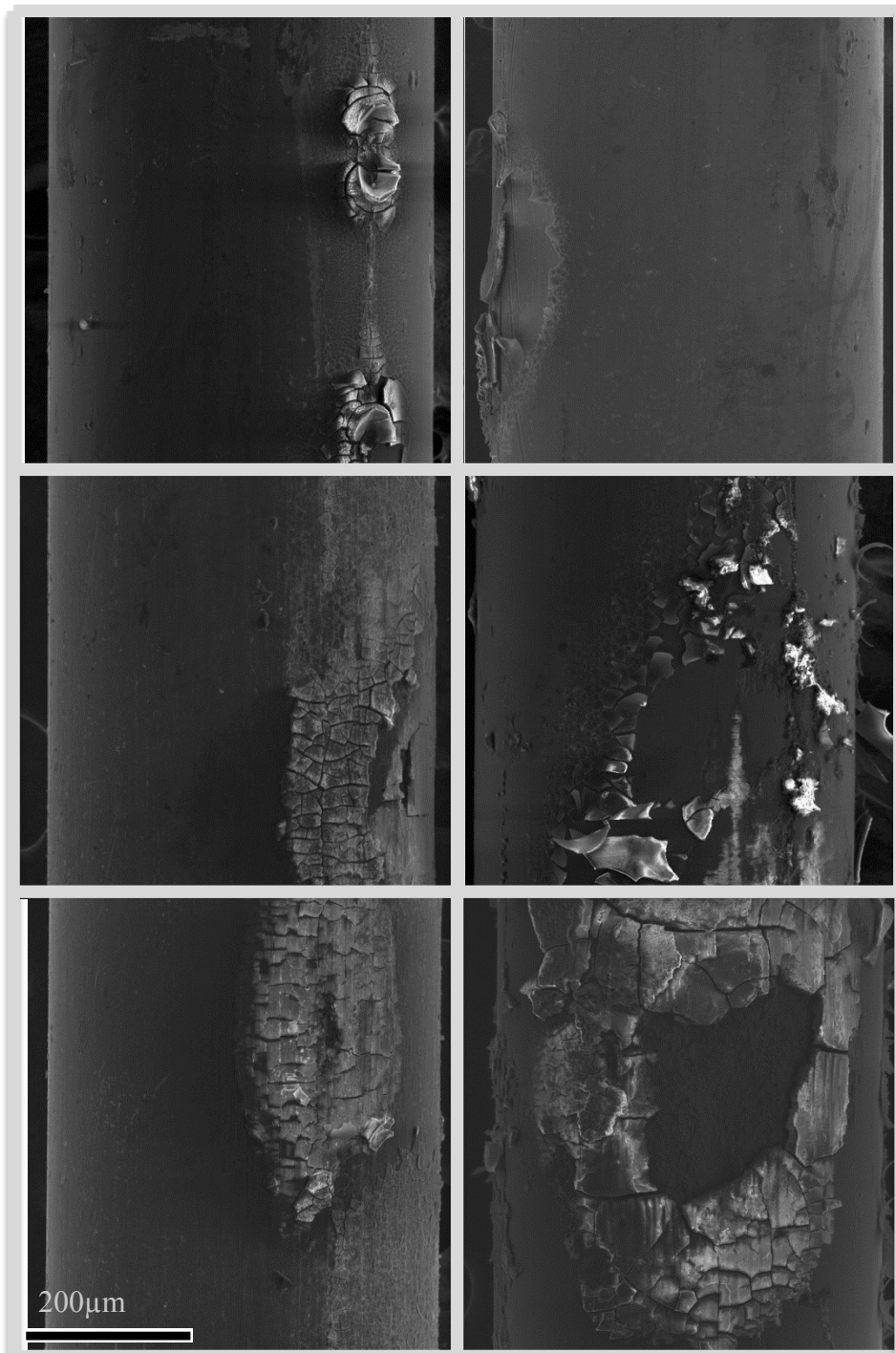


**Figure 7.2.** (previous page) The left column SEM images are taken from control samples degraded for 60 days while the right column is taken from degraded samples with daily applied magnetic fields for 60 days. A 200  $\mu\text{m}$  scale (black) is shown in the bottom left image which applies for all images.

Analysis of cross-sectioned wires revealed surface area reductions as shown in **Table 7.1**. The calculations shown in the table assume that mass loss is directly proportional to surface area. As expected, when compared to direct weighing (see **Figure 7.1**), the calculation of mass loss from cross-sectioned images showed slightly higher losses from both the control (3.22 mg vs. 2.72 mg) and the samples vibrated by the applied magnetic field (4.55 mg vs. 3.77 mg). In both cases, the differences can be explained by noting that the direct weighing method included the degradation product still adhered to the surface of the bulk material, while the cross-sectional analysis was taken from the unaltered sample.

**Table 7.1.** Mass loss results using surface area analysis in ImageJ software. Measurements are taken as a percent difference from a 0.5 mm diameter wire.

	Control	Vibrated
<b>AVG (% change)</b>	1.03%	1.45%
<b>STD</b>	1.05%	0.73%
<b>Mass (mg)</b>	3.22	4.55

While the results of this test corroborate the results of the mass loss experiment, statistical significance between vibrated and control samples (ANOVA,  $p < 0.05$ ) was not obtained. The high degree of variability in samples using this method is likely a result of the non-uniform surface area along the wire's length as well as the cracking seen in **Figure 7.3**. The large crack extending from near the center of the wire to the surface was a result of the sample cross-sectioning method and was observed in all samples.

For the non-vibrated wire, corrosion products resembling relatively low atomic weight oxides were abundantly present at the wire/epoxy interface (**Figure 7.4a**). These oxides most likely include gallium and iron oxides, with some possible derivative of  $\text{Ca}_3(\text{PO}_4)_2$  for locations in the non-vibrated sample (b and c from **Table 7.2**).

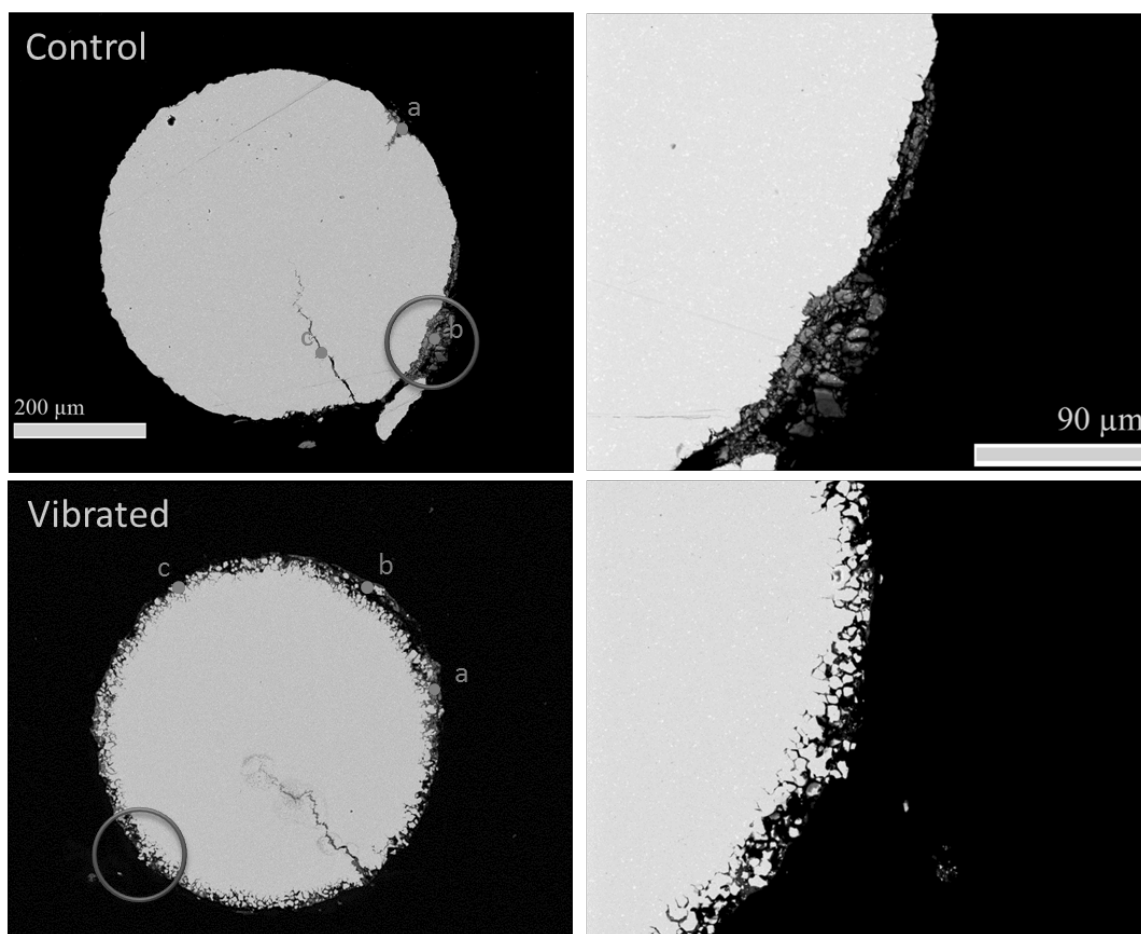


**Figure 7.3.** Backscatter images of wire cross sections after 60 days of degradation in media. Images are at 140X (left) and 3,300X (right) normal magnification for non-vibrated (top) and vibrated samples (bottom). The red circles in images at left mark the locations that the images at right were taken. The red dots labeled a, b, and c mark the locations where EDS was performed as presented in **Table 7.2**.

**Figure 7.3** also indicates that the vibrated samples exhibited a different mode of corrosion when compared with the non-vibrated samples. Large portions of the bulk material were dislodged, while oxide development occurred within the interstitial space (**Figure 7.4b**). Furthermore, **Figure 7.4b** shows concentrated gallium depletion in the bulk iron matrix approaching the corrosion-surface interface of the wire (lighter dot-like regions among the bulk were comprised primarily of gallium). EDS characterization of multiple points in the vibrated sample oxide exhibit a relatively higher weight percentage of gallium content in multiple regions relative to the non-vibrated corrosion products. A possible explanation for this phenomenon could be that the vibration causes an unstable gallium cation near the surface of the wire in the bulk matrix that favorably dissolves into the oxide product, leaving gallium depleted, iron rich fragmented bulk particles, and a more gallium rich oxide compared to the non-vibrated samples.

**Table 7.2.** EDS weight percentage per element by location (ND = not detected).

	<b>Fe wt%</b>	<b>Ga wt%</b>	<b>O wt%</b>	<b>C wt%</b>	<b>P wt%</b>	<b>Ca wt%</b>
<b>Control Sample</b>						
<b>a</b>	12.16	62.34	25.35	0.15	ND	ND
<b>b</b>	50.99	7.63	31.11	1.78	6.45	2.05
<b>c</b>	68.01	7.85	23.47	0.40	0.12	0.14
<b>Vibrated Sample</b>						
<b>a</b>	58.62	17.31	23.57	0.27	ND	0.22
<b>b</b>	61.82	13.56	23.83	0.50	ND	0.29
<b>c</b>	41.01	33.93	24.54	0.40	ND	0.13

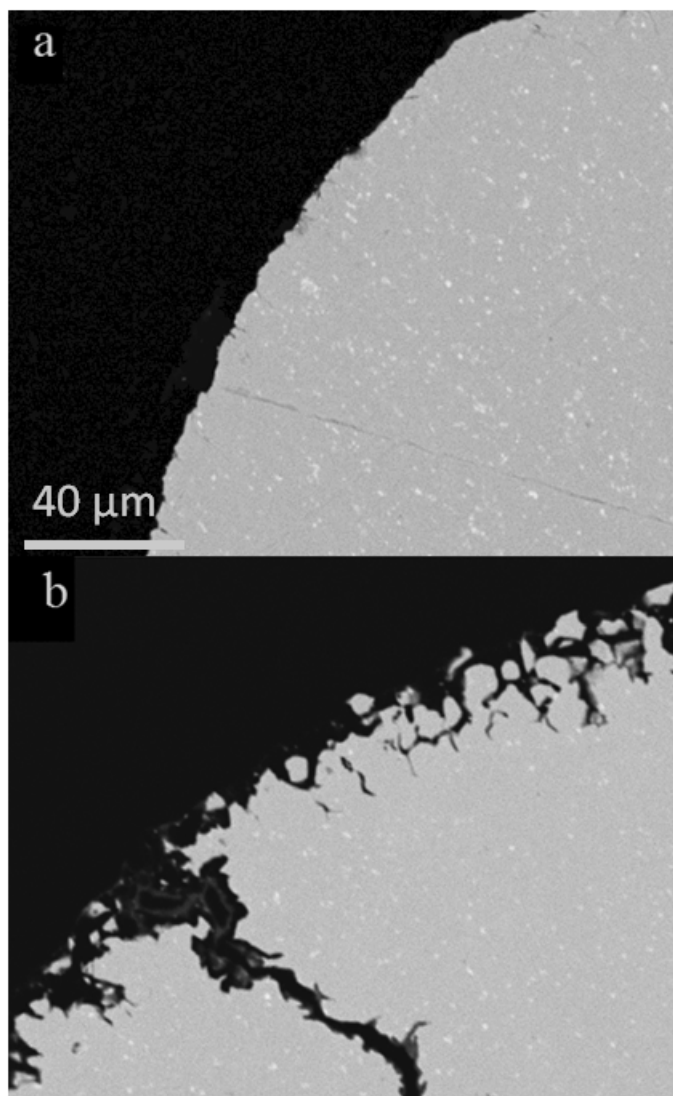


**Figure 7.4.** High magnification backscatter images of (a) control sample at and (b) vibrated sample.

A second possible explanation for the differences in oxide constituents is that the gallium oxides are more favorable on the surface of the bulk. Because Gallfenol is primarily body-centered cubic  $\alpha$ -Fe with randomly substituted gallium [7.28], it is expected that these regions contribute to stress concentrations, and thus, areas with increased reactivity. The Pilling-Bedworth ratio as given by [7.29]:

$$R_{PB} = \frac{M_{oxide} \cdot \rho_{metal}}{M_{metal} \cdot \rho_{oxide}}$$

where  $M$  is the molecular weight and  $\rho$  is the density, can be used to estimate the properties of oxide formation on a surface. Ratios less than 1 produce porous oxides, between 1 and 2 produce stable oxides, and greater than 2 produce unstable/non-uniform oxide layers. On Galfenol, the Pilling-Bedworth ratio of  $\text{Fe}_2\text{O}_3$  and  $\text{Ga}_2\text{O}_3$  are 2.21 and 1.69. Thus, the non-vibrated samples, spalling (flaking off) of iron-based oxides is more likely to occur. However, in the case of the magnetically vibrated samples, the induced strains may contribute to increasing the rate of detachment of oxide layers of all types, especially at regions of gallium impurities that could contribute to local stress concentrations. Thus, the thin layer of oxides at the surface of vibrated samples is expected to be composed of components closer to the iron/gallium ratio of the bulk material.

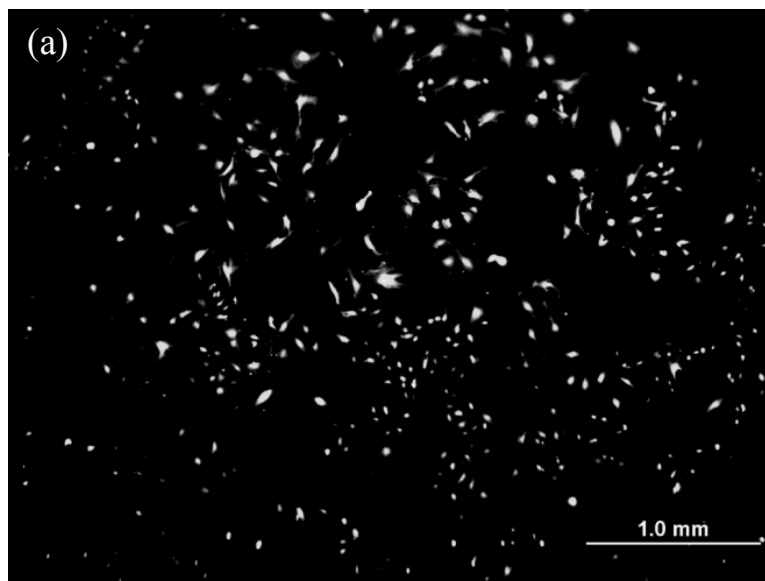
### 7.3.3. Indirect Cytotoxicity Test

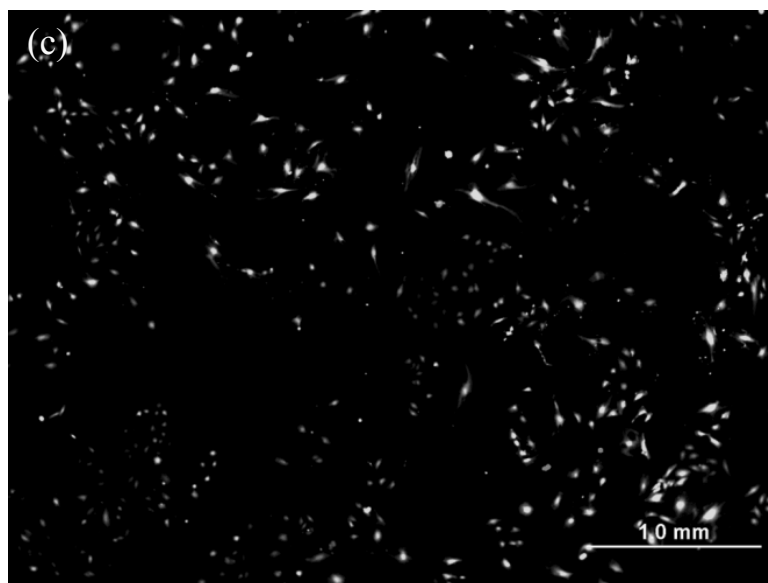
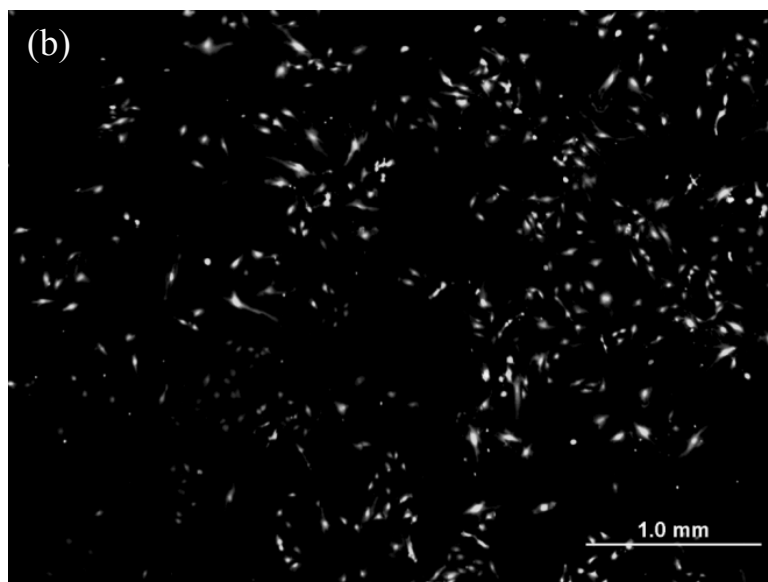
Results from the indirect cytotoxicity test using 10  $\mu\text{g/mL}$ , 25  $\mu\text{g/mL}$ , 50  $\mu\text{g/mL}$ , and 100  $\mu\text{g/mL}$  concentrations of Galfenol degradation byproduct are shown in **Figure 7.5** and **Figure 7.6**. (as calculated using measured mass loss). Analysis of variance (ANOVA) was performed on the cell count data produced by the cell viability experiment with  $p < 0.05$ . Significance was found between the 50  $\mu\text{g/mL}$  cultures and every other group. There was also found to be significance between the 100  $\mu\text{g/mL}$  cultures and every other group.

Previous work by Muller and coworkers showed that primary umbilical venous smooth muscle cell proliferation could be controlled via concentration of ferrous iron in the surrounding tissue [7.30]. In order to confirm that Galfenol byproducts produce similar effects, the total cell counts (live + dead) were plotted as shown in **Figure 7.7**. A significant difference between the total cells in the control wells and wells from all other concentrations (except for 10  $\mu\text{g/mL}$ ) were found. In fact, increasing the Galfenol

byproduct concentration appeared to have an increasingly anti-proliferative effect on the aortic smooth muscle cells.

Although this test shows significant levels of cellular death, this could be interpreted several ways. First, the concentrations of iron and gallium in these tests represent a higher concentration than would be expected *in vivo*. This is due to the fact that the experiment was run in static conditions, whereas blood circulation would carry some of the byproduct away from the stent in most applications. Additionally, the concentrations exposed to the SMC's were approximately 7 times higher than would be expected, even in an *in vitro* setting. This is due to the fact that a concentrated product was used to amplify exposure of the byproduct to the cell cultures. Furthermore, since the iron load in the blood is 400-500  $\mu\text{g/mL}$  [7.30], it is unlikely that the comparatively smaller iron load from a stent would cause considerable problems in an *in vivo* setting. This assumes that the degradation byproducts of the alloyed iron-gallium are comparable to that of pure iron stents and intravenously injected gallium.





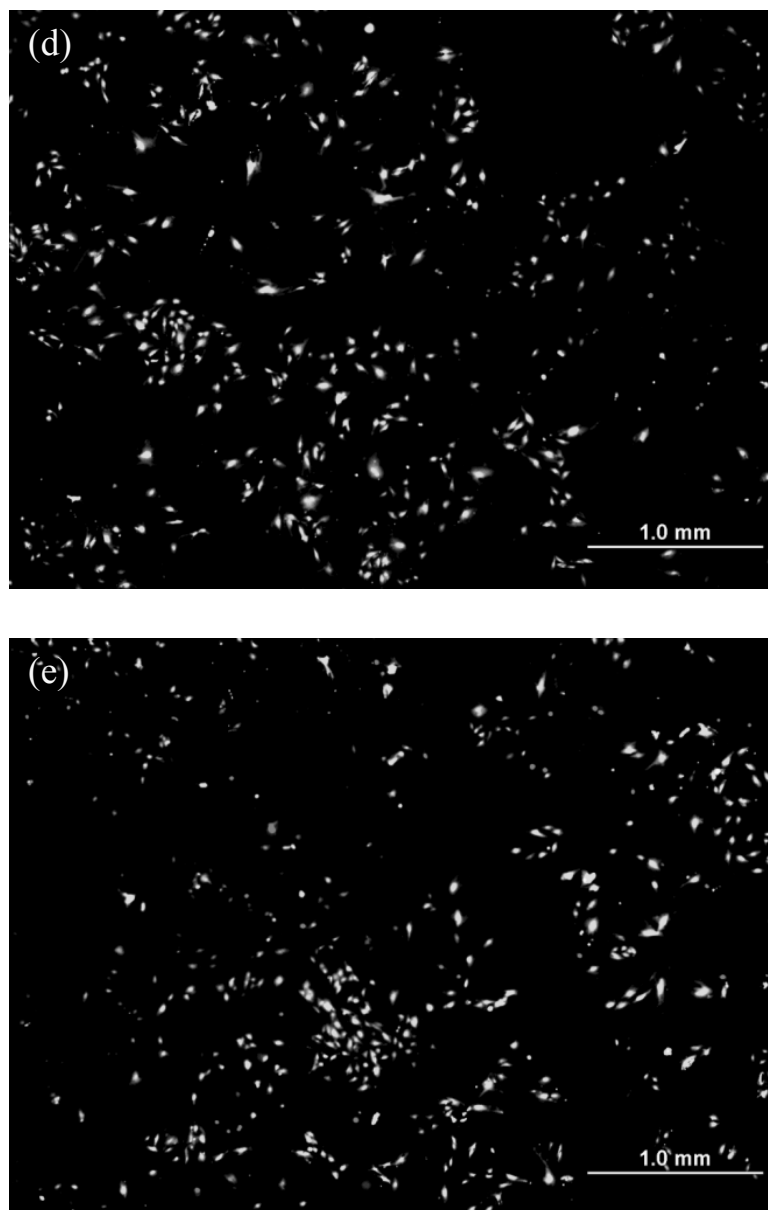


**Figure 7.5.** Visual illustration of the Calcein-AM (live) and Ethidium Bromide (dead) fluorescent assay for the (a) control (b) 10  $\mu\text{g/mL}$  (c) 25  $\mu\text{g/mL}$  (d) 50  $\mu\text{g/mL}$  and (e) 100  $\mu\text{g/mL}$  concentrations of Galfenol degradation byproduct.

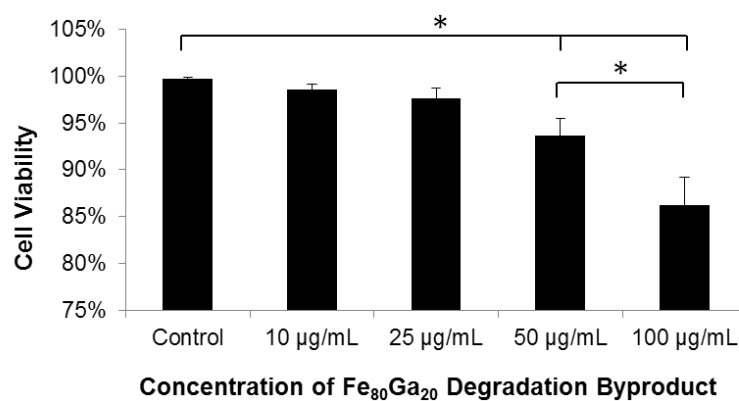


**Figure 7.6.** Exposure to concentration of Galfenol degradation byproducts vs. cell death. # - 50 µg/mL and 100 µg/mL were found to be significant when compared against all other concentrations (ANOVA,  $p < 0.05$ ).

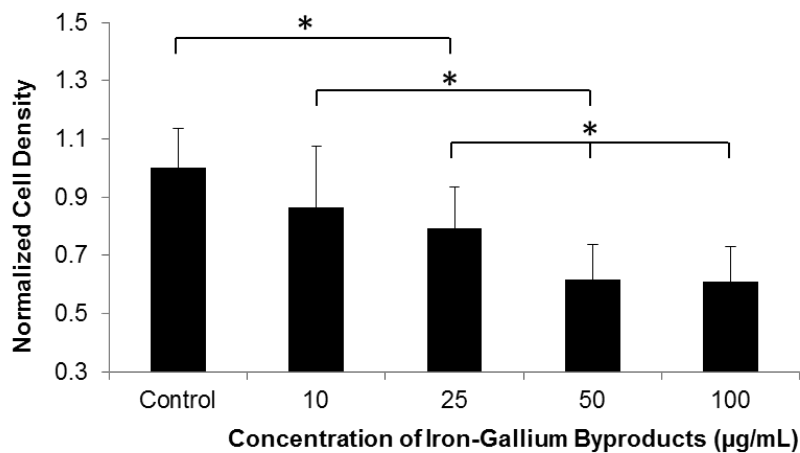


**Figure 7.7.** Average cell count per well with Galfenol degradation byproduct exposure.

\* - Significance was found between all columns except the control vs. 10 µg/mL, 10 µg/mL vs. 25 µg/mL, and 50 µg/mL vs 100 µg/mL (ANOVA,  $p < 0.05$ ).

## 7.4. Conclusion

The biodegradation and cytotoxicity of Galfenol (iron-gallium) were analyzed. Results showed that high enough concentrations of degradation byproducts to result in significant primary smooth muscle cell mortality are not produced in static *in vitro* conditions. Anti-proliferative effects of Galfenol were also observed with decreasing cell counts in cultures with increasing amounts of degradation byproduct. This was likely due to the presence of ferrous iron that has been shown to have anti-proliferative effects on smooth muscle cells in the literature. Qualitative comparison of wire samples with and without applied magnetic field showed a possible acceleration of delamination and detachment of surface oxides due to dissimilar strains between the magnetoelastic iron-gallium and non-magnetoelastic oxide. Mass loss measurements using Fe<sub>80</sub>Ga<sub>20</sub> wires confirmed results from previous *ex vivo* work showing that degradation can be controlled wirelessly by application of applied magnetic fields.

Several future experiments are warranted for further investigation of the cytotoxic effects of high concentrations of Galfenol. First, apoptotic cellular toxicity should be confirmed to rule out the possibility of secondary tissue damage due to cell necrosis. Second, investigations into the cytotoxicity with and without applied magnetic field should be performed. Previous studies have shown that vibrating magnetoelastic materials can cause morphological changes in cell behavior [7.31]. Specifically, a variety of cell types were shown to attach/detach to the material more readily depending on vibration frequency. Quite possibly, this material could be used to control cellular activity around the stent material at different time-points in the degradation process. Future work should include aortic endothelial and smooth muscle cells investigated in terms of their attachment and proliferation in response to magnetoelastic sub-micron vibrations at frequencies relevant to inducing biodegradation (tens to hundreds of Hz).

Due to non-uniform pitting corrosion and relatively low degradation rates (0.41 mg/cm<sup>3</sup> per day), the corrosion rate of Galfenol still needs to be significantly increased for stenting applications. However, even with current degradation rates, this material could be used as an external coating of a fast-degrading material such as magnesium in order to control how long the inner material is protected from degradation. Additionally, other magnetoelastic materials with higher base degradation rates and more uniform corrosion could be investigated as possible alternatives for this application.

## References

- 7.1. D. Panescu, "Emerging technologies drug eluting stents," *IEEE Eng. Med. Bio. Mag.*, Vol. 23, No. 2, pp. 21-23, 2004.
- 7.2. H. Hermawan, D. Mantovani, "New generation of medical implants: metallic biodegradable coronary stent," *International Conference on Instrumentation, Communication, Information Technology and Biomedical Engineering*, pp. 399-402, 2011.
- 7.3. H. Hermawan, D. Dubé, D. Mantovani, "Developments in metallic biodegradable stents," *Acta Biomaterialia*, Vol. 6, pp. 1693-1697, 2010.
- 7.4. H.R. Holmes, A. DeRouin, S. Wright, T.A. Lograsso, T.M. Riedemann, R.M. Rajachar, K.G. Ong, "Biodegradation and biocompatibility of mechanically active magnetoelastic materials," *Smart Mater. Struct.*, Vol. 23, 095036 (5pp). 2014
- 7.5. M. Peuster, P. Wohlsein, M. Brugmann, M. Ehlerding, K. Seidler, C. Fink, H. Brauer, A. Fischer, G. Hausdorf, "A novel approach to temporary stenting: degradable cardiovascular stents produced from corrodible metal - results 6–18 months after implantation into New Zealand white rabbits," *Heart*, Vol. 86, pp. 563–569, 2001.

- 7.6. M. Peuster, C. Hesse, T. Schloo, C. Fink, P. Beerbaum, C. von Schnakenburg, “Long-term biocompatibility of a corrodible peripheral iron stent in the porcine descending aorta,” *Biomaterials*, Vol. 27, pp. 4955–4962, 2006.
- 7.7. R. Waksman, R. Pakala, R. Baffour, R. Seabron, D. Hellinga, F.O. Tio, “Short-term effects of biocorrodible iron stents in porcine coronary arteries,” *J. Interv. Cardiol.*, Vol. 21, pp. 15–20, 2008.
- 7.8. G. Mani, M.D. Feldman, D. Patel, C.M. Agrawal, “Coronary stents: A materials perspective.” *Biomaterials*, Vol. 28, pp. 1689–1710, 2007.
- 7.9. F. Nie, Y. Zheng, S. Wei, C. Hu, G. Yang, “In vitro corrosion, cytotoxicity and hemocompatibility of bulk nanocrystalline pure iron.” *Biomed. Mater.*, Vol. 5, 065015, 2010.
- 7.10. M. Moravej, F. Prima, M. Fiset, D. Mantovani, “Electroformed iron as new biomaterial for degradable stents: Development process and structure-properties relationship,” *Acta Biomater.*, Vol. 6, pp. 1726–1735, 2010.
- 7.11. M. Moravej, A. Purnama, M. Fiset, J. Couet, D. Mantovani, “Electroformed pure iron as a new biomaterial for degradable stents: In vitro degradation and preliminary cell viability studies,” *Acta Biomater.*, Vol. 6, pp. 1843–1851, 2010.
- 7.12. B. Liu, Y. Zheng, “Effects of alloying elements (Mn, Co, Al, W, Sn, B, C and S) on biodegradability and in vitro biocompatibility of pure iron,” *Acta Biomater.*, Vol. 7, pp. 1407–1420, 2010
- 7.13. B. Liu, Y. Zheng, L. Ruan, “In vitro investigation of Fe<sub>30</sub>Mn<sub>6</sub>Si shape memory alloy as potential biodegradable metallic material.” *Mater. Lett.*, Vol. 65, pp. 540–543, 2010.
- 7.14. W. Xu, X. Lu, L. Tan, K. Yang, *Acta Metallurgica Sinica*, Vol. 47, pp. 1342–1347, 2011.
- 7.15. M. Schinhammer, A.C. Hanzi, J.F. Loffler, P.J. Uggowitzer, “Design strategy for biodegradable Fe-based alloys for medical applications.” *Acta Biomater.*, Vol. 6, pp. 1705–1713, 2010.

- 7.16. M. Schinhammer, P. Steiger, F. Moszner, J.F. Löffler, P.J. Uggowitzer, *Materials Science and Engineering C*, Vol. 33, pp. 1882–1893, 2013.
- 7.17. J. Cheng, Y.F. Zheng, *Journal of Biomedical Materials Research Part B: Applied Biomaterials*, Vol. 101B, pp. 485–497, 2013.
- 7.18. D.T. Chou, D. Wells, D. Hong, B. Lee, H. Kuhn, P.N. Kumta, *Acta Biomaterialia*, Vol. 9, pp. 8593–8603, 2013.
- 7.19. S. Zhu, N. Huang, L. Xu, Y. Zhang, H. Liu, Y. Lei, H. Sun, Y. Yao, *Surface and Coatings Technology*, Vol. 203, pp. 1523–1529, 2009.
- 7.20. S. Zhu, N. Huang, H. Shu, Y. Wu, L. Xu, *Applied Surface Science*, Vol. 256, pp. 99–104, 2009.
- 7.21. C.Z. Chen, X.H. Shi, P.C. Zhang, B. Bai, Y.X. Leng, N. Huang, *Solid State Ionics*, Vol. 179, pp. 971–974, 2008.
- 7.22. L.R. Bernstein, J.J.M. van der Hoeven, R.O. Boer, “Hepatocellular carcinoma detection by gallium scan and subsequent treatment by gallium maltolate: rationale and case study.” *Anticancer Agents Med. Chem.*, Vol. 11, No. 6, pp. 585-590, 2011.
- 7.23. A. Rangel-Vega, L.R. Bernstein, E.A. Mandujano-Tinoco, S.J. Garcia-Contreras, R. Garcia-Contreras, “Drug repurposing as an alternative for the treatment of recalcitrant bacterial infections,” *Front. Microbiol.*, Vol. 6. No. 282, 2015.
- 7.24. E. Summers, T.A. Lograsso, J.D. Snodgrass, J. Slaughter, “Magnetic and Mechanical Properties of Polycrystalline Galfenol,” *Proc. Int. Symp. on Smart structures and materials*, Vol. 5387, pp. 448-459, 2004.
- 7.25. A.R. Clark, K.B. Hathaway, M. Won-Fogle, J.B. Resteroff, T.A. Lograsso, V.M. Keppens, G. Petculescu, R.A. Taylor, “Extraordinary magnetoelasticity and lattice softening in bcc Fe-Ga alloys,” *J. Applied Phys.*, Vol. 93, No. 10, pp. 8621-8624, 2003.
- 7.26. J. Chamley-Campbell, G.R. Campbell, and R.L. Ross. "The smooth muscle cell in culture." *Physiological reviews*, Vol. 59. No. 1, pp. 1-61, 1979.

- 7.27. A. Trion, and A. van der Laarse. "Vascular smooth muscle cells and calcification in atherosclerosis." *American heart journal*, Vol. 147 No. 5, pp. 808-814, 2004.
- 7.28. Development and modeling of iron-gallium alloy, Rick A. Kellogg, 2003.
- 7.29. C. Xu, W. Gao, "Pilling-Bedworth ratio for oxidation of alloys," *Mat. Res. Innovat.*, Vol. 3, No. 4, pp. 231-235, 2000.
- 7.30. P.P. Mueller, T. May, A. Perz, H. Hauser, M. Peuster, "Control of smooth muscle cell proliferation by ferrous iron," *Biomaterials*, Vol. 27, No. 10, pp. 2193-2200, 2005.
- 7.31. H.R. Holmes, E.L. Tan, K.G. Ong, R.M. Rajachar, "Fabrication of biocompatible, vibrational magnetoelastic materials for controlling cellular adhesion," *Biosensors*, Vol. 2, No. 1, pp. 57-69, 2012.

## 8. Overall Conclusions

Presented in this work were a variety of studies that, as a whole, aimed to improve the feasibility of magnetoelastic materials for sensing and actuating applications. Magnetoelastic resonant sensors of non-standard geometries were investigated to determine if geometry could play a role on the sensitivity of the sensor response to mass loading. It was shown that a significant increase in sensitivity could be achieved by using triangular sensors rather than standard rectangular strips. The aspect ratio of the triangular sensors was shown to play a critical role in their sensitivity. It was also demonstrated that a flower-shaped custom coil apparatus could detect changes in multiple parameters simultaneously in a single frequency sweep given triangular sensors with a variety of dimensions. These advances are a first step in the development of a multi-functional mass-based sensing platform for biological analysis of physiological fluids. For example, the design could be implemented for using a small amount of the fluid of interest to be dropped in the center of a pattern of triangular sensors (all pointing towards the center) in order to detect various different parameters (e.g. glucose, pH, etc.).

A method for monitoring multiple parameters on a single magnetoelastic resonant strip was also pursued. It was demonstrated that the region of the sensor with mass loading affects the harmonic resonant frequencies in different manners, as previously presented in the literature. Typically, masses much lower than the sensor mass (two orders of magnitude or more) saturate the sensor response; however, this work showed that masses comparable to the sensor mass behaved in the same fashion as those in lower load ranges. Additionally, it was shown that the mass response of sensors loaded at multiple locations simultaneously behaved in a manner that would allow the assumption of superposition of each individual location's effect on the overall resonant response.

Magneto-harmonic sensors and actuators were also explored in this work. Specifically, it was demonstrated that magnetoelastic sensors could be implemented as a means of detecting stresses on deep tissue wounds, which are critical for proper healing of the wound sites after surgery. Both a suture and a suture anchor design were

investigated for their efficacy at monitoring forces applied to tendon repair sites. The suture sensor prototype was composed of a flat stainless steel wire with magnetoelastic sensor adhered along its length. Hooks on either end of the stainless steel wire were attached to suture threads, allowing load-sharing between the sensor and substrate. This design allows for modification of the load sensitivity by changing the sensor substrate (stiffer materials will have lower range and lower sensitivity, and vice versa). The force-sensing capability of the suture sensor was demonstrated in *ex vivo* porcine skin and North American white-tailed deer Achilles tendon models. Testing also revealed a relatively low degree of error (< 5%) with movement of the sensor within a 5 mm radius of the center of the detection coil.

It was determined that there would be situations where the suture sensor could not be implemented due to the addition of the rigid sensor portion of the suture. Therefore, a suture anchor was created which would allow the surgical procedure to remain unchanged during tendon repairs. The sensor system was specifically designed for use in rotator cuff surgical repairs, as they represent one of the most failure-prone and common surgical practices. 3D printed suture anchors based on a commonly implemented commercial suture anchor (Smith and Nephew's TwinFix Ultra PK) were instrumented with magnetoelastic sensors intended for operation in the harmonic sensing mode. Specifically, the sensors consisted of multiple Metglas 2826MB strips adhered in parallel to one another to the side of a flat stainless steel wire. The wire was looped on both sides to increase purchase within the screw and to secure to the suture thread. The fabricated sensing element was embedded in the hollow section of the head of the anchor. Because the load orientation of the tendon-attached suture on the sensing element was expected to vary based on surgical procedure and anatomical variation, the sensor was tested at multiple angles. From 15° and 45° from the longitudinal direction of the anchor, the slope of the sensor response was shown to be constant. This is the ideal case, since the load direction is expected to stay below 45° in most cases due to the fact that the loop of the sensing element is nested inside the head of the screw. This sensor design is a promising

prototype for tendon-repair applications, as it has the potential to provide quantitative feedback regarding the forces experienced at a patient's actual wound site, rather than relying on patient-biased parameters such as pain tolerance and assumed capacity to perform certain tests.

One of the main advantages proposed for magnetoelastic sensing platforms is their low-cost nature. Base materials for sensors can range from about \$0.10 to \$2.00 each; however, detection devices that are capable of monitoring these sensors are relatively high cost, especially for systems utilizing small resonant sensors (high frequency) or sensors placed a large distance away from the detection coil (high power). These systems generally cost tens of thousands of dollars. Thus, the systems are only truly low-cost when implementing a large number of sensor nodes with a single detector. This is a likely reason that, at the time of this publication, the only obvious commercially available magnetoelastic systems are used to detect torque on rotating parts. Therefore, two detection devices were fabricated and built which represent low-cost alternatives (both less than \$200 each, comparable to any other sensor technology) to commercially available alternatives. The result of this work makes the claim that magnetoelastic sensing solutions are low-cost alternatives more concrete.

The biodegradability and cytotoxicity of a promising magnetoelastic material for biomedical applications, Galfenol (iron-gallium) was also investigated. Cytotoxicity tests demonstrated that concentrations much higher than would likely be encountered *in vivo* are necessary to cause significant cellular toxicity. Anti-proliferative effects were observed in primary aortic rat smooth muscle cells with exposure to Galfenol byproducts, which suggests the presence of ferrous iron. Additionally, surface characterization of the degraded materials suggests that the degradation rate of Galfenol can be wirelessly controlled through application of externally applied magnetic fields to more readily expose the bulk material to biological solvents. Compared to the previous work, the data presented in this dissertation was obtained with more robust testing conditions and cell types specific to stenting applications to validate and expand the understanding of

Galfenol's biocompatibility and controllable degradation rates. This work has illustrated that magnetoelastic actuation of implantable devices with controllable post-implantation degradation rates are a promising new candidate for vascular stenting (and other biomedical applications).

## Appendix

**Table A1.** Bill of materials for the thresholding magnetoelastic resonance detection device. Component costs were determined from Digi-Key Electronics as of 08/25/2016.

<b>Part</b>	<b>Each at 1 Unit</b>	<b>Each at 1000 Units</b>	<b># Per Device</b>	<b>Cost 1 Device</b>	<b>Cost 1000 Devices</b>
<b>MSP430f2618 MCU</b>	\$12.60	\$7.26	1	\$12.60	\$7.26
<b>AP1117 V Reg</b>	\$0.47	\$0.14	1	\$0.47	\$0.14
<b>PS8802 Opt Isolator</b>	\$3.12	\$1.43	2	\$6.24	\$2.85
<b>LF353 Op Amp</b>	\$0.54	\$0.21	4	\$2.16	\$0.84
<b>50 MHz Crystal</b>	\$1.14	\$0.66	1	\$1.14	\$0.66
<b>AD5932 Fun Gen</b>	\$10.21	\$5.79	1	\$10.21	\$5.79
<b>AD624 Inst Amp</b>	\$40.84	\$29.20	1	\$40.84	\$29.20
<b>SMD capacitors</b>	\$0.10	\$0.00	40	\$4.00	\$0.10
<b>SMD Resistors</b>	\$0.10	\$0.00	39	\$3.90	\$0.08
<b>1N4148 Diodes</b>	\$0.14	\$0.03	7	\$0.98	\$0.19
<b>TIP41C NPN BJT</b>	\$0.62	\$0.24	1	\$0.62	\$0.24
<b>TIP42C PNP BJT</b>	\$0.62	\$0.24	1	\$0.62	\$0.24
<b>AD8564 Comparator</b>	\$8.66	\$4.91	2	\$17.32	\$9.82
<b>ADG4562 Switch</b>	\$6.15	\$3.85	1	\$6.15	\$3.85
<b>P25A14E Supply</b>	\$29.95	\$19.08	1	\$29.95	\$19.08
<b>TO220 Heatsink</b>	\$1.03	\$0.71	2	\$2.06	\$1.42
<b>Circuit Enclosure</b>	\$14.50	\$9.64	1	\$14.50	\$9.64
<b>Circuit Fabrication</b>	\$43.00	\$0.43	1	\$43.00	\$0.43
<b>Totals</b>				<b>\$196.76</b>	<b>\$91.84</b>

**Table A2.** Bill of materials for the frequency-domain detection device for magneto-harmonic detection. Component costs were determined from Digi-Key Electronics as of 08/25/2016.

<b>Part</b>	<b>Each at 1 Unit</b>	<b>Each at 1000 Units</b>	<b># Per Device</b>	<b>Cost 1 Device</b>	<b>Cost 1000 Devices</b>
<b>MSP430f2618 MCU</b>	\$12.60	\$7.26	1	\$12.60	\$7.26
<b>AP1117 Regulator</b>	\$0.47	\$0.14	1	\$0.47	\$0.14
<b>PS8802 OptIsolator</b>	\$3.12	\$1.43	2	\$6.24	\$2.85
<b>LF353 Op Amp</b>	\$0.54	\$0.21	11	\$5.94	\$2.31
<b>C4051D MUX</b>	\$0.45	\$0.14	1	\$0.45	\$0.14
<b>SMD capacitors</b>	\$0.10	\$0.00	44	\$4.40	\$0.11
<b>SMD Resistors</b>	\$0.10	\$0.00	71	\$7.10	\$0.15
<b>OPA548 Power Amp</b>	\$15.51	\$12.01	2	\$31.02	\$24.01
<b>RAC10-05DC/277</b>	\$27.69	\$22.81	1	\$27.69	\$22.81
<b>Supply</b>					
<b>Circuit Enclosure</b>	\$14.50	\$9.64	1	\$14.50	\$9.64
<b>Circuit Fabrication</b>	\$43.00	\$0.47	1	\$43.00	\$0.47
<b>Totals</b>				<b>\$153.41</b>	<b>\$69.89</b>